TRANSPORT IN A TRELLISED AGRICULTURAL CANOPY: TURBULENCE AND PARTICLE DISPERSION

by

Nathan E. Miller

A dissertation submitted to the faculty of
The University of Utah
in partial fulfillment of the requirements for the degree of

Doctor of Philosophy

Department of Mechanical Engineering

The University of Utah

May 2017

The University of Utah Graduate School

STATEMENT OF DISSERTATION APPROVAL

The dissertation of **Nathan E. Miller**

has been approved by the following supervisory committee members:

James R. Stoll II	, Chair	**12/6/2016** Date Approved
Eric R. Pardyjak	, Member	Date Approved
Meredith Metzger	, Member	**12/28/2016** Date Approved
Marc Calaf	, Member	**1/12/2017** Date Approved
John C. Lin	, Member	**1/13/2017** Date Approved

and by **Tim Ameel**, Chair/Dean of

the Department/College/School of **Mechanical Engineering**

and by David B. Kieda, Dean of The Graduate School.

ABSTRACT

Turbulent transport of momentum, scalars, and heavy particles within plant canopies is strongly impacted by the canopy's effect on the flow field in the canopy sub-layer (CSL). Although considerable research has been conducted on momentum and particle transport in and above dense homogeneous plant canopies, relatively little has been performed in perennial trellised canopies which have repetitive inhomogeneities at the scale of the canopy height. Particle transport in such canopies is of great interest due to the increasing use of training systems of this type by growers and due to the multitude of particle types regularly dispersed in these canopies, e.g., fungal spores and droplets sprayed by growers. The focus of this work is on the transport of momentum and fungal-spore-sized particles in a trellised vineyard canopy.

Due to the discrete two-dimensional nature of the vineyard canopy, CSL flow characteristics differ from those seen in homogeneous canopies and change as a function of the above-canopy wind direction. To determine the specifics of how the trellised canopy geometry and local meteorological conditions combine to determine the characteristics of momentum and particle transport under all possible wind directions, multiple field campaigns were conducted in a vineyard in Oregon. During each of these campaigns, extensive meteorological data were collected while particles were released into the canopy and particle concentrations were sampled at downwind locations. The meteorological and plume data showed that the canopy exerted inhomogeneous nonisotropic drag, caused channeling of the flow along the aisles, and led to persistent coherent flow effects. The combination of these effects led to momentum statistics varying with wind direction, particle transport being biased to along the rows, and plume shapes being more complicated than those seen in homogeneous canopies or freestream flows.

For teaching me how to work, for pushing me to be my best,
and for never ceasing to amaze and encourage me,
I dedicate this to my wonderful parents.

CONTENTS

LIST OF FIGURES

LIST OF TABLES

ACKNOWLEDGMENTS

First, I need to acknowledge my advisor, Dr. Rob Stoll, for his commitment to this work and to helping and advising me throughout my graduate school career. He was always available when needed and worked continuously to improve my abilities as a scientist, researcher, and writer. Second only to my advisor, the help of Dr. Walt Mahaffee of the USDA-ARS has been paramount to my success. I have spent considerable time with Walt and have worked side by side with him throughout this project. He has challenged me, taught me, and inspired me, and deserves considerable recognition. Many other professors have also had a large impact on my education and deserve to be recognized. This includes the members of my advisory committee and Dr. Tim Ameel, Dr. Dan Adams, and Dr. Kent Udell, all of whom I respect greatly. Additionally, I want to thank a number of my peers for their individual efforts in helping with research, writing, classes, encouragement, and friendship. Foremost, this includes Nathan Andrews, Jacqueline Beckvermit, and Tim Price, but also includes Andrew Gould, Sean Moran, Ahsanuzzaman Khan, and others. Finally, I need to acknowledge the Corvallis USDA-ARS staff for their help in conducting the field work for this project. Foremost among these is Tara Neill, whose painstaking work of counting microspheres under the microscope for days on end was of singular importance to the progress of this work. Additionally, Lindsay Theissen, Cole Provence, Jim Eynard, Andy Albrecht, and others deserve acknowledgement for help in conducting the field campaigns and collecting the data.

This work was funded by a National Science Foundation (grant AGS 1255662) and by USDA funding obtained by Walt Mahaffee (project 5358-22000-039-00D). Also, some travel, accommodation, and equipment costs for my trips to Oregon for field campaigns were covered by grants received from the University of Utah's Global Change and Sustainability Center.

CHAPTER 1

INTRODUCTION

The flow field within the canopy sub-layer (CSL) of the atmospheric boundary layer (ABL), is directly influenced by the structure of the canopy's elements (Finnigan, 2000). The ABL is the portion of Earth's atmosphere that is in contact with and is directly affected by the planet's surface, and the CSL is the lowest portion of the ABL. CSL flow facilitates the transport of momentum, scalars, and heavy particles among the canopy elements and to and from the overlying ABL. The influence of the canopy elements on the CSL flow physics is dictated in part by the architecture, solidity, rigidity, and packing density of the individual canopy elements (Dupont and Brunet, 2008). In order for us to understand transport-based bio-physical processes within canopies, particularly those of varied architectures, the understanding of the canopy's influence on that transport is paramount. This is especially important for predicting processes like pollution accumulation, propagule transport, pesticide drift, or even bio-chemical weapon dispersement.

Two main categories of canopies have received considerable research interest in recent years: urban canopies and plant canopies. This project is focused on the transport of momentum and particulates in a trellised agricultural canopy, a canopy type with similarities to both of these categories.

Plant canopies, including both natural canopies like forests (Raynor et al., 1974) and agricultural canopies like wheat fields (Aylor and Ferrandino, 1989), have received extensive research interest for many years. Most of these works have focused on relatively dense homogeneous plant canopies that show little variation in canopy structure (i.e., height, density, or element distribution) at scales on the order of the canopy height, regardless of the location within the canopy and regardless of

direction (e.g., Pan et al., 2014). Considerably fewer transport studies have been done in the CSL of heterogeneous canopies: those with gaps or structural changes with characteristic length scales on or above the order of the canopy height. Studies of this type include single streamwise transitions from one canopy type to another, like a forest edge (Yang et al., 2006; Boudreault et al., 2016), repeating streamwise step changes like sets of windbreaks (Judd et al., 1996) or trellised canopies like vineyards (Bailey and Stoll, 2013), and more complex three-dimensional (3D) canopies like orchards (Dupont and Patton, 2012), forest clearings (Damschen et al., 2014), and modeled plant canopies studied in wind tunnels (Böhm et al., 2013). Although these 3D canopies differ from homogeneous canopies—which are one-dimensional—at local scales, mean planar statistics from both often do not (Harman et al., 2016).

Perhaps the most complex heterogenous canopies to receive focused research interest are urban canopies (e.g., Klein et al., 2007; Hanna and Baja, 2009) and scaled urban-like canopies often composed of cube shaped obstructions (e.g., Yee and Biltoft, 2004; Coceal et al., 2007). Real urban canopies typically have more random patterns with buildings of different heights and shapes distributed somewhat haphazardly, though often still in grid like "blocks" (e.g., Allwine et al., 2002; Britter and Hanna, 2003). Many of the mock urban canopies are held in wind- or water-tunnels and usually consist of identical discrete elements spaced in grid-like patterns of varying densities (e.g., Belcher, 2005; Huq and Franzese, 2013). Urban canopies and the mock canopies used to study them are typified by street canyons which are known to lead to effects like along-canyon flow channeling and persistent flow features (Belcher, 2005; Addepalli and Pardyjak, 2013; Santiago et al., 2013).

Of all of the referenced studies, the majority have only investigated momentum or tracer transport, with comparatively few having studied heavy particle transport. From these studies though, models have been developed for the transport of momentum, tracers, and particulates (e.g., Settles, 2006; Klein et al., 2007; Singh et al., 2008). Additionally, of those that have studied particulate and/or tracer transport, most have been limited by low sampling densities that are often only along a single arc or in a single plane. The sampling has also only typically been performed at downstream distances much greater than a few canopy heights (e.g., Chamecki et al.,

2012), and the data have often only been used to track maximum concentration locations instead of the entire plume shapes (e.g., Hanna and Baja, 2009).

The work reported here is focused on transport of momentum and heavy particles in a two-dimensional perennial trellised plant canopy. This canopy system has been studied considerably less than the homogeneous plant canopies or the heterogenous urban-like canopies, but some recent work has begun investigating this canopy type (Bailey and Stoll, 2013; Bailey et al., 2014b; Chahine et al., 2014). Trellised canopies exhibit similarities with urban canopies (e.g., gaps between elements similar to street canyons), with homogenous plant canopies (e.g., flexible plants, similar length-scale distributions), and with windbreaks (e.g., two-dimensional coordinates, wake features). For this study specifically, the work was performed in a field of *Vitis vinifera* (i.e., a grape vineyard). The use of trellising systems is increasing in many perennial crops (Talaie et al., 2011) and its prevalence in the American Northwest has increased in recent years with increased planting of vineyards. This, combined with the direct economic impact of grapes, results in grape vineyards being of particular interest[1]. The dispersion of particulates is incredibly common in these and similar fields and includes pollens, disease propagules, and liquid droplets from sprays like those often applied by the grower to mitigate damage from pests or fungi. Powdery mildew of grapes (*Erysiphe necator*) is the most widespread and economically important pathogen of cultivated grapes in arid and semi-arid regions with losses as high as 20–25% in susceptible cultivars during severe epidemics (Grove, 2004). Turbulent transport of spores is one of the primary mechanisms in the life cycle of fungal pathogens like *E. necator* (Aylor, 1999). Without it, spores would not spread beyond surfaces very near the host, thus limiting the speed of epidemic expansion (McCartney and West, 2007). Mitigating the impacts of fungal plant pathogens like powdery mildew requires an understanding of the mechanisms that control the rate of epidemic development and severity, and as a primary component of that, the turbulent transport of spores in the CSL.

It was hypothesized the due to the two-dimensional nature of the vineyard canopy,

[1]USDA National Agricultural Statistics Service, Noncitrus Fruits and Nuts Summaries (usda.mannlib.cornell.edu/MannUsda/viewDocumentInfo.do?documentID=1113)

the CSL flow would behave differently when the winds were blowing from different directions with respect to the vine-row direction. This alteration of the CSL flow with the above-canopy wind direction would hypothetically also alter the dispersion of particulate to be different from both homogeneous-canopy and freestream dispersion. The goal therefore was to identify and understand the processes and environmental factors of highest importance to the spread of wind-borne particulate in sparse row-oriented agricultural canopies, specifically vineyards. To accomplish this, field studies that included the releasing and tracking of particles were performed in a vineyard in Oregon in the summers of 2011 and 2013. Meteorological data collected during each year were used to understand the wind-direction dependencies of the mean flow, fluxes, and turbulence in and above the canopy (Chapter 2). Particle release events that were conducted in 2011 during periods when the above-canopy winds were blowing roughly parallel to the vine row direction were investigated and the plume shape was elucidated via a skewed-Gaussian plume equation (Chapter 3). Finally, plumes of considerably more complex shapes, that were released during periods when the mean wind direction above the canopy was significantly different than the vine row direction, were studied using a novel approach that included the superposition of two Gaussian plume equations oriented orthogonally to each other (Chapter 4). Ongoing efforts are using the information learned from these experiments with the goal of building a comprehensive vineyard ecosystem model that includes submodules for the dispersion of particulates, all in an effort to more accurately, economically, and sustainably manage fields of trellised crops (Chapter 5).

1.1 Research Plan

To investigate the flow and transport behavior in vineyards, a series of field studies were conducted in a vineyard in Oregon. The field work was completed in conjunction with the United States Department of Agriculture (UDSA) Agricultural Research Service's (ARS) Horticulture Crops Research Unit in Corvallis. They provided much of the equipment necessary for the experiments as well as provided lab space from which to organize and operate and were crucial in getting access to the field in which the campaigns were completed.

The field campaigns were performed near Monmouth, Oregon (≈ 44° 49′ 28″ N, 123° 14′ 15″ W) in a relatively flat vineyard with ≈ 43 hectares of vines oriented to within 2° of true north-to-south. The vineyard canopy was composed of approximately five year old vines with an average height of 1.9–2.2 m. The leaf area index (LAI = leaf area per ground area) was determined via a leaf pull during each campaign and was ≈ 1.2, which is comparable to vineyards observed in other studies (Johnson et al., 2003). The vine rows were spaced at 2.5 m on center, had a row thickness of ≈ 0.5 m, and an understory opening of ≈ 0.8 m.

1.1.1 Meteorological and Momentum Data Collection

During each of the campaigns, a meteorological tower was deployed in the center of an aisle between two vine rows near the center of the vineyard block where the campaigns were conducted. The tower held Campbell Scientific CSAT3 sonic anemometers at different heights with at least two positioned lower than the canopy top and two above the canopy top (Figure 1.1). This allowed for accurate profiles of relevant statistics to be determined in the CSL. A fine-wire thermocouple was collocated with each anemometer and all were sampled at ≈ 20 Hz for 24 hours per day throughout the campaigns. Campbell Scientific dataloggers were used to store the data. Many other sensors collecting data on soil properties, leaf temperatures, radiation budget components, and carbon and water fluxes were also deployed on and around the tower during each campaign and much of that data have been used in other studies (Bailey et al., 2014a, 2016). Extensive detail about the sensor locations and arrangement, as well as the collected data files, can be found in Appendix A for the 2011 campaign and in Appendix B for the 2013 campaign.

The data from the meteorological tower were partitioned into as many independent continuous 30-minute periods as could be obtained. A period length of 30 minutes was chosen after an ogives test on data collected from a precursory experiment conducted in 2010 revealed that that length was the minimum that provided satisfactory convergence of statistics regardless of the wind direction or the time of day. Standard relevant parameters including the average velocity, the mean wind direction above the canopy, and the canopy-top stability were determined for each of the 30-minute

periods. Flux profiles of heat and momentum, turbulent statistic (e.g., variance) profiles, and energy spectra were calculated for each period. Ensemble averages of these statistics and profiles were taken across all periods with similar stabilities and wind directions. Due to the symmetry of the geometry of the vineyard, the dependencies of these variables were then reduced to only a function of the difference between the mean wind direction above the canopy and the vine row direction (north-to-south). By this definition, the functionality was reduced to only a range of 0° to 90° for row-parallel to row-perpendicular winds. Additionally, the behavior of the row-parallel- and row-perpendicular-oriented components of the velocity and flux behavior was also investigated versus the same mean-wind-to-row-direction difference. This required defining a coordinate system based on the vine row direction with the row-perpendicular velocity component represented as $u_{\perp}$ and the row-parallel component represented as $v_{\parallel}$ (Figure 1.2). This system is explained in more detail in Chapter 2 and used therein and in Chapter 4.

1.1.2 Particle Dispersion Testing

Particle release events were used to understand the transport of heavy particulates in the vineyard. This was done by releasing fluorescing polyethylene microspheres (Cospheric LLC) that had a similar size and weight to the spores of multiple fungal pathogens of interest for vineyards. The mean diameter of the microspheres was ≈ 32 μm with $> 90\%$ of them having diameters between 10 and 45 μm. Microspheres of different colors were emitted into the canopy at multiple heights at a central location in the vineyard over set periods of time. Separate colors of microspheres were emitted from each height during each of the release events to allow for multiple plumes to be characterized under identical wind conditions. Two different microsphere emission methods were used in the field and are described in Chapters 3 and 4.

During each of the release events, the microsphere plume concentrations were sampled using rotating arm impaction traps designed by the USDA ARS collaborators (Thiessen et al., 2016). Five impaction traps were mounted at different heights on towers made of Aluminum T-channel and the towers were arranged into wide arrays designed to capture the shape of the plumes. At least 20 towers were used for each

Figure 1.1: Photos of the meteorological towers in the aisle of the vineyard during the 2011 (left) and 2013 (right) campaigns. The photo from 2011 is southward looking at the northward pointed anemometers while the 2013 photo is northward looking at the westward pointed anemometers.

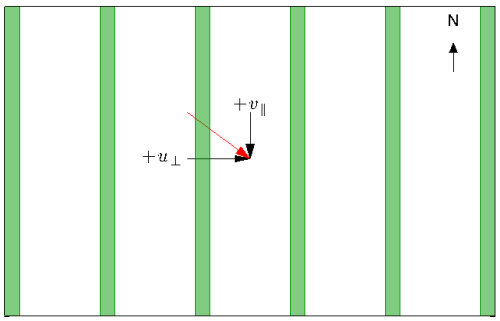

Figure 1.2: A simple schematic of the row-aligned coordinate system used for some portions of the analysis. For any mean wind direction (*red vector*), the row-perpendicular and row-parallel components (*black vectors*) were defined as positive in the direction nearest that of the mean wind direction.

release event, leading to the plume being sampled at ≥ 100 locations downwind of the source. The towers were all kept to downwind distances of no greater than a few canopy heights, thus resulting in a relatively high-resolution understanding of the near-source plume shape. At the end of each release event, the sample rods from each impaction trap were collected and examined. The number of microspheres collected by each trap was determined and used to calculate the mass concentration at each trap location. Considerably more detail on the impaction trap towers and the layout of the tower arrays—including schematics and dimensions—can be found in Appendices A and B for the 2011 and 2013 campaigns, respectively.

The fungal plant pathogens that are most commonly found in vineyard tend to be the most active at releasing spores in the afternoon (Pady and Subbayya, 1970). It is likely that the atmospheric stability during these time is unstable and that the higher temperatures and vertical mixing contribute to the emission of the spores. The microsphere release events were therefore performed at similar times and under similar stability conditions. As many release events as could be completed within the campaign windows were performed, resulting in over 25 release events with over 70 individual plumes collected under a wind variety of wind directions.

1.2 References

Addepalli, B. and E. R. Pardyjak, 2013: Investigation of the flow structure in step-up street canyons - mean flow and turbulence statistics. *Boundary-Layer Meteorol.*, **148**, 133–155.

Allwine, K. J., J. H. Shinn, G. E. Streit, K. L. Clawson, and M. Brown, 2002: Overview of urban 2000: A multiscale field study of dispersion through an urban environment. *Bull. Amer. Meteor. Soc.*, **83**, 521–536.

Aylor, D. E., 1999: Biophysical scaling and the passive dispersal of fungus spores: Relationship to integrated pest management strategies. *Agric. For. Meteorol.*, **97**, 275–292.

Aylor, D. E. and F. J. Ferrandino, 1989: Dispersion of spores released from an elevated line source within a wheat canopy. *Boundary-Layer Meteorol.*, **46**, 251–273.

Bailey, B. N., M. Overby, P. Willemsen, E. R. Pardyjak, W. F. Mahaffee, and R. Stoll, 2014a: A scalable plant-resolving radiative transfer model based on optimized gpu ray tracing. *Agric. For. Meteorol.*, **198–199**, 192–208.

Bailey, B. N. and R. Stoll, 2013: Turbulence in sparse, organized vegetative canopies: A large-eddy simulation study. *Boundary-Layer Meteorol.*, **147**, 369–400.

Bailey, B. N., R. Stoll, E. R. Pardyjak, and W. F. Mahaffee, 2014b: Effect of vegetative canopy architecture on vertical transport of massless particles. *Atmos. Environ.*, **95**, 480–489.

Bailey, B. N., R. Stoll, E. R. Pardyjak, and N. E. Miller, 2016: A new three-dimensional energy balance model for complex plant canopy geometries: Model development and improved validation strategies. *Agric. For. Meteorol.*, **218–219**, 146–160.

Belcher, S. E., 2005: Mixing and transport in urban areas. *Phil. Trans. R. Soc. A*, **363**, 2947–2968.

Böhm, M., J. J. Finnigan, M. R. Raupach, and D. Hughes, 2013: Turbulence structure within and above a canopy of bluff elements. *Boundary-Layer Meteorol.*, **146**, 393–419.

Boudreault, L., S. Dupont, A. Bechmann, and E. Dellwik, 2016: How forest inhomogeneities affect the edge flow. *Boundary-Layer Meteorol.*, dOI 10.1007/s10546-016-0202-5.

Britter, R. E. and S. R. Hanna, 2003: Flow and dispersion in urban areas. *Ann. Rev. Fluid Mech.*, **35**, 469–496.

Chahine, A., S. Dupont, C. Sinfort, and Y. Brunet, 2014: Wind-flow dynamics over a vineyard. *Boundary-Layer Meteorol.*, **151**, 557–577.

Chamecki, M., N. S. Default, and S. A. Isard, 2012: Atmospheric dispersion of wheat rust spores: A new theoretical framework to interpret field data and estimate downwind dispersion. *J. Appl. Meteorol. Climatol.*, **51**, 672–685.

Coceal, O., A. Dobre, T. G. Thomas, and S. E. Belcher, 2007: Structure of turbulent flow over regular arrays of cubical roughness. *J. Fluid Mech.*, **589**, 375–409.

Damschen, E. I., et al., 2014: How fragmentation and corridors affect wind dynamics and seed dispersal in open habitats. *PNAS*, **111**, 3484–3489.

Dupont, S. and Y. Brunet, 2008: Influence of foliar density profile on canopy flow: A large-eddy simulation study. *Agric. For. Meteorol.*, **148**, 976–990.

Dupont, S. and E. G. Patton, 2012: Influence of stability and seasonal canopy changes on micrometeorology within and above an orchard canopy: The CHATS experiment. *Agric. For. Meteorol.*, **157**, 11–29.

Finnigan, J. J., 2000: Turbulence in plant canopies. *Ann. Rev. Fluid Mech.*, **32**, 519–571.

Grove, G. G., 2004: Perennation of *Uncinula necator* in vineyards of eastern washington. *Plant Disease*, **88**, 242–247.

Hanna, S. R. and E. Baja, 2009: A simple urban dispersion model tested with tracer data from Oklahoma City and Manhattan. *Atmos. Environ.*, **43**, 778–786.

Harman, I. N., M. Böhm, J. J. Finnigan, and D. Hughes, 2016: Spatial variability of the flow and turbulence within a model canopy. *Boundary-Layer Meteorol.*, **160**, 375–396.

Huq, P. and P. Franzese, 2013: Measurements of turbulence and dispersion in three idealized urban canopies with different aspect ratios and comparisons with a gaussian plume model. *Boundary-Layer Meteorol.*, **147**, 103–121.

Johnson, L. F., D. E. Roczen, S. K. Youkhana, R. R. Nemani, and D. F. Bosch, 2003: Mapping vineyard leaf area with multispectral satellite imagery. *Comput. Electron. Agric.*, **38**, 33–44.

Judd, M. J., M. R. Raupach, and J. J. Finnigan, 1996: A wind tunnel study of turbulent flow around single and multiple windbreaks, Part 1: Velocity fields. *Boundary-Layer Meteorol.*, **80**, 127–165.

Klein, P., B. Leitl, and M. Schatzmann, 2007: Driving physical mechanisms of flow and dispersion in urban canopies. *Int. J. Climatol.*, **27**, 1887–1908.

McCartney, A. and J. West, 2007: *Dispersal of fungal spores through the air.*, chap. 4, 65–81. Taylor and Francis Group, Boca Raton, FL, USA.

Pady, S. M. and J. Subbayya, 1970: Spore release in uncinula necator. *Phytopathology*, **60**, 1702–1703.

Pan, Y., M. Chamecki, and S. A. Isard, 2014: Large-eddy simulation of turbulence and particle dispersion inside the canopy roughness sublayer. *J. Fluid Mech.*, **753**, 499–534.

Raynor, G. S., J. V. Hayes, and E. C. Ogden, 1974: Particulate dispersion into and within a forest. *Boundary-Layer Meteorol.*, **7**, 429–456.

Santiago, J. L., O. Coceal, and A. Martilli, 2013: How to parameterize urban-canopy drag to reproduce wind-direction effects within the canopy. *Boundary-Layer Meteorol.*, **149**, 43–63.

Settles, G. S., 2006: Fluid mechanics and homeland security. *Ann. Rev. Fluid Mech.*, **38**, 87–110.

Singh, B., B. S. Hansen, M. J. Brown, and E. R. Pardyjak, 2008: Evaluation of the QUIC-URB fast response urban wind model for a cubical building array and wide building street canyon. *Environ. Fluid Mech.*, **8**, 281–312.

Talaie, A., M. Shojaie-Saadee, A. Dadashpour, and M. A. Asgari-Sarcheshmeh, 2011: Fruit quality in five apple cultivars trees trained to intensive training system: Geneva y-trellis. *GENETIKA*, **43**, 153–161.

Thiessen, L. D., J. A. Keune, T. M. Neill, W. W. Turechek, G. G. Grove, and W. F. Mahaffee, 2016: Development of a grower-conducted inoculum detection assay for management of grape powdery mildew. *Plant Pathology*, **65**, 238–249.

Yang, B., A. P. Morse, R. H. Shaw, and K. T. Paw U, 2006: Large-eddy simulation of turbulent flow across a forest edge. Part II: Momentum and turbulent kinetic energy budgets. *Boundary-Layer Meteorol.*, **121**, 433–457.

Yee, E. and C. A. Biltoft, 2004: Concentration fluctuation measurements in a plume dispersing through a regular array of obstacles. *Boundary-Layer Meteorol.*, **111**, 363–415.

CHAPTER 2

MEAN AND TURBULENT FLOW STATISTICS IN A TRELLISED AGRICULTURAL CANOPY

This chapter has been submitted to Boundary-Layer Meteorology as "Mean and Turbulent Flow Statistics in a Trellised Agricultural Canopy," Nathan E. Miller, Rob Stoll, Walter Mahaffee and Eric R. Pardyjak, October 2016.

The architecture of a trellised agricultural canopy shares many similarities with homogeneous plant canopies, windbreaks, and urban canopies. Compared to these other canopies, trellised canopies like vineyards have received less attention and present an interesting, complex, two-dimensional environment. Analysis of meteorological data from an Oregon vineyard demonstrated that the canopy strongly influenced the flow by channelling the mean wind into the vine row direction regardless of the above-canopy wind direction. Additionally, other flow statistics in the canopy sub-layer showed a dependence on the difference between the above-canopy wind direction and the vine row direction. This included an increase in the canopy displacement height and a decrease in the canopy-top shear length scale as the above-canopy winds rotated from row-parallel toward row-orthogonal. Distinct wind-direction based variations were also observed in the components of the stress tensor, turbulent kinetic energy budget, and the energy spectra. Although spectral results suggested that sonic anemometry was insufficient for resolving all of the important scales of motion within the canopy, the energy spectra peaks still exhibited dependencies on the canopy and the wind direction. These variations demonstrated that although the flow within trellised canopies behaves similarly to flow in other canopies under some conditions, directionally dependent functionality needs to be determined over

the range of conditions to which such canopies are exposed if accurate flow predictions are going to be made.

2.1 Introduction

Turbulent transport of momentum, scalars, and heavy particles within plant canopies is strongly impacted by the canopy's effect on the flow field in the lowest portion of the atmospheric boundary layer, the canopy sub-layer (CSL) (Finnigan, 2000). The fluid-structure interaction physics within the CSL are dictated in part by canopy architecture and density (e.g., Dupont and Brunet, 2008; Bailey and Stoll, 2013; Maurer et al., 2015).

Considerable research has examined momentum transport in and above relatively dense homogeneous plant canopies like forests (e.g., Meyers and Baldocchi, 1991; Launiainen et al., 2007; Belcher et al., 2012), corn fields (e.g., Wilson et al., 1982; Pan et al., 2014), and wheat fields (e.g., Legg and Long, 1975; Aylor and Ferrandino, 1989). These canopies are considered homogeneous because they show little consistent variation in height or density at scales at or above the canopy-height or as a function of direction. By comparison, considerably less turbulent transport research has been done in the CSL of heterogeneous plant canopies (canopies with inhomogeneities at the canopy height scale). There is a wide gradation of complexities with heterogeneous canopies, ranging from a single streamwise transition like a forest edge (e.g., Yang et al., 2006; Boudreault et al., 2016), to repeating transitions in the streamwise direction like windbreaks or vineyards (e.g., Judd et al., 1996; Bailey and Stoll, 2013), up to more complex three-dimensional distributions of discrete elements spaced in grid-like patterns of varying densities (e.g., Böhm et al., 2013; Huq and Franzese, 2013). Though these three-dimensionally discrete canopies differ from homogeneous canopies at local scales, planar-mean statistics from each often show little appreciable difference (Harman et al., 2016).

Urban canopies, typified by deep street canyons, have also received considerable attention and have shown similar behavior to vegetative canopies at some scales (e.g., Klein et al., 2007; Hanna and Baja, 2009). Effects like flow channelling along the street canyons and persistent flow phenomena within canyons are well documented

(Hoydysh and Dabberdt, 1994; Belcher, 2005; Addepalli and Pardyjak, 2013; Santiago et al., 2013).

Recently, studies have been done on inherently two-dimensional heterogeneous plant canopy systems (Bailey and Stoll, 2013; Bailey et al., 2014b; Chahine et al., 2014). Examples of systems of this type are vineyards and modern orchards which are experiencing a management trend toward a trellised architecture (Talaie et al., 2011). Canopies of this type exhibit obvious similarities to homogeneous plant canopies, windbreaks, discrete element canopies used in tunnels, and to urban canopies with street canyons (Belcher, 2005; Klein et al., 2007). The similarities with homogeneous plant canopies and windbreaks include the inflected velocity profile, the existence of mixing-layer structures at the canopy top (Bailey and Stoll, 2013), and the impact of the vegetative elements on the flow field, e.g., leaf-scale wake production (Finnigan, 2000). The similarities with urban canopies include effects like flow channelling, inhomogeneous and anisotropic drag, and the possibility of persistent features.

The goal of this study was to investigate the hypothesis that flow field statistics in a discrete two-dimensional canopy differ from those seen in other canopies and vary as a function of the above-canopy wind direction. We used a perennial trellised canopy of *Vitis vinifera* (i.e., wine grape) because of the direct economic impact of grapes and their increasing prevalence throughout the U.S.[1], as well as for the potential application of the knowledge to improving disease management (Mahaffee et al., 2014; Miller et al., 2015; Mahaffee and Stoll, 2016; Thiessen et al., 2016). This work directly investigates the transport mechanisms in the field over a wide range of wind directions using data collected during multiple years. Flow data in the vineyard CSL were collected via field campaigns performed in a commercial vineyard in Oregon (Section 2.2). Results determined from the data collected in the vineyard were then used to elucidate how trellised canopy architecture and local meteorological conditions affect momentum transport characteristics in the vineyard CSL (Section 2.3).

---

[1]USDA National Agricultural Statistics Service, Noncitrus Fruits and Nuts Summaries (usda.mannlib.cornell.edu/MannUsda/viewDocumentInfo.do?documentID=1113)

2.2 Field Campaign

In August of 2011 and 2013, field campaigns (C11 and C13, respectively) were conducted in a vineyard near Monmouth, Oregon. C11 was explained in detail in Miller et al. (2015), hereafter M15.

Similarly to C11, in 2013, a meteorological tower was deployed between two north-to-south oriented vine rows near the center of a vineyard block (≈ 44° 49′ 27.0″ N, 123° 14′ 17.0″ W). The tower held three Campbell Scientific CSAT3 sonic anemometers positioned below the canopy top and three positioned above the canopy top (Fig. 2.1). Each one was pointed due west and their sampling volumes were roughly centered in the aisle. Two of the anemometers above the canopy were positioned at approximately the same heights as in the 2011 experiment while the third (z = 10.1 m) was deployed twice as high as the uppermost anemometer from C11. Collocated with each anemometer was a 12.7 μm fine-wire thermocouple, the data from which were recorded along with the tri-directional wind data from the anemometers.

The canopy surrounding the meteorological tower in 2013 received more cultural management (e.g., hedging and shoot tucking) than in C11 to maintain a canopy thickness of $r_w \approx 0.5$ m and produce a relatively flat face to the individual rows with far fewer stray shoots protruding into the aisles. In 2013, the canopy had increased in height to 2.16 m (h); up from the 1.9 m during C11. The rows spacing (r_s) and the understory height up to the fruiting wire remained unaltered at 2.5 m and 0.74 m, respectively. The leaf area density (LAD) profile for C11 and C13 were determined using the process explained in M15 and were reported in M15 and Bailey et al. (2014a), respectively. The total leaf area index (LAI) of the block was 1.0 in 2013, slightly lower than the 1.4 recorded in 2011.

2.2.1 Data Processing

Statistics were determined using independent 30-minute periods from the meteorological data. All periods with winds coming from behind the tower (165°–195° in C11 and 80°–138° in C13) at any anemometer height were removed from further analysis. Periods with a turbulence intensity (σ_M/M where M was the wind magnitude)

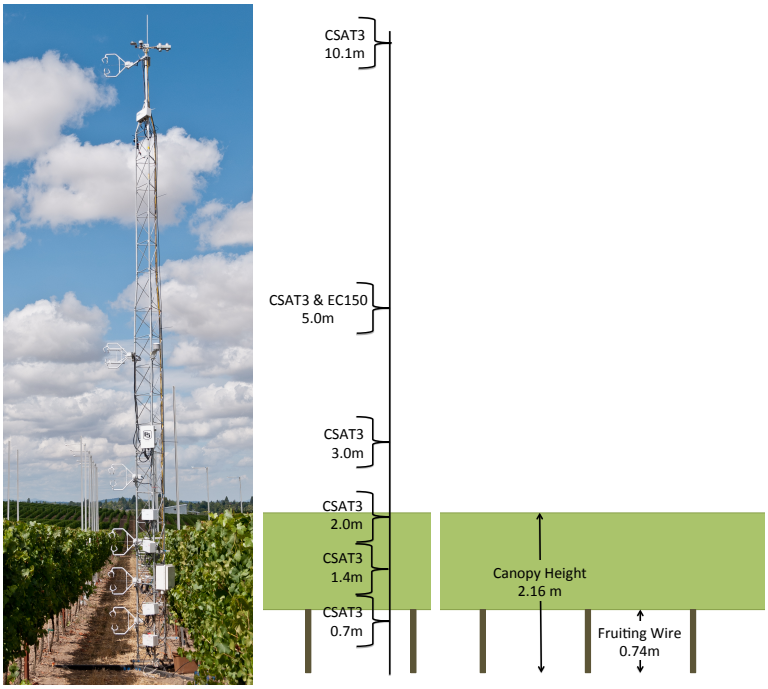

Figure 2.1: A northward looking photo of the meteorological tower in the aisle of the vineyard during the 2013 campaign as well as a schematic of the tower and canopy to provide relevant dimensions.

of > 0.5 at the uppermost anemometer were also excluded from further analysis. Relevant statistics including first, second, and third order characteristics of the velocity components, momentum fluxes, turbulent energy, and energy spectra were determined for each anemometer during each period.

The canopy-top stability was characterised for each period using $\zeta = h/L$. Here, the Obukhov length was defined as $L = -\overline{T_o}u_{*,h}^3/(\kappa g(\overline{w'T'})_h)$, where $\overline{T_o}$ was a reference temperature taken as the temperature at the top of the canopy, $\overline{w'T'}$ was the absolute vertical heat flux, overbars are temporal means of the 30-minute periods, primes represent deviations from the half-hour means, κ is the von Kármán constant (taken as 0.4), g is gravitational acceleration, the subscript h denotes values determined at the canopy top, and the friction velocity was defined as $u_* = \left[\overline{u'w'}^2 + \overline{v'w'}^2\right]^{1/4}$, where u, v, and w are the streamwise, spanwise, and vertical velocities, respectively. All periods were categorised into stability classes, the thresholds for which were determined using the canopy-top fluxes following Mahrt (1998), Launiainen et al. (2007), and Dupont and Patton (2012). The five classifications and their thresholds for C11 were convective (C, $h/L < -0.31$), moderately convective (MC, $-0.31 < h/L \leq -0.01$), neutral (N, $-0.01 < h/L \leq 0.03$), moderately stable (MS, $0.03 < h/L \leq 0.6$), and stable (S, $h/L > 0.6$). For the 2013 data, the same classes (C, MC, N, MS, S) were used but the threshold between the C and MC categories was adjusted to $h/L = -0.2$. The 2013 C and MC threshold likely differed because of the changes in the canopy geometry. For the remainder of this study, the data from C13 were primarily used and were comparable to the C11 data unless otherwise stated.

Due to the inherent symmetry of the geometry of the vineyard, wind-direction dependencies were reduced to only a function of δ, the difference between the mean wind direction at $z = 10.1$ m ($\overline{wd}$) and the vine row direction. Thus $|\delta|$ only ranged from 0° to 90° for row-parallel to row-perpendicular winds, respectively.

Five directional classes were defined for use in comparisons: *parallel* ($|\delta| \leq 10°$), *near-parallel* ($10° < |\delta| \leq 24°$), *row-diagonal* ($24° < |\delta| \leq 42°$), *near-perpendicular* ($42° < |\delta| \leq 62°$), and *perpendicular* ($|\delta| > 62°$) (Table 2.1). These thresholds were chosen based on observations made from the data. Due to the broad range of individual stabilities seen among the relatively limited quantity of S periods and the fact that

Table 2.1: The number of independent 30-minute periods from C13 classified into the separate directional and stability classes.

	C	MC	N	MS	S
Parallel	20	34	12	17	5
Near-Parallel	22	35	15	35	6
Row Diagonal	22	48	36	25	8
Near-Perpendicular	5	69	58	27	5
Perpendicular	3	11	7	26	9

periods of this type should likely be studied with different scaling arguments than those used for the other classes (Sorbjan, 2010; Grachev et al., 2013), the S periods were all excluded from further study as part of this work. The stabilities of the individual C periods also had a broad range. In all but the *perpendicular* case, a sufficient number of periods were obtained to provide usable ensemble statistics. Although most of the C periods were used here, due to the limited number of cases in the *perpendicular* class, the periods from that class were not used. Instead, whenever row-perpendicular profiles of C periods were needed for comparisons, profiles from the *near-perpendicular* class were used. For each of the stability classes, scaling was typically performed using $u_{*,h}$. For highly convective flows, the convective velocity scale (w_*) is often used (Deardorff, 1970), but was not used here. Using estimates of the mixed layer height (z_i) based on balloon soundings[2] from the Salem, OR airport, values of $w_{*,h}$ were found to typically be $\approx 8u_{*,h}$ for the C periods. Fortunately, the use of u_* provided a satisfactory collapse of the C periods, likely because the heights being used were all within the atmospheric surface layer.

The discrete nature of the trellised canopy also necessitated that the statistical profiles be investigated using methods not typically used for homogenous canopies. Due to the channelling effects of the canopy (Section 2.3), a traditional three-dimensional (3D) rotation of the wind data did not provide the same investigative benefit as it does in freestream or homogeneous environments. Under conditions of *perpendicular*

[2]NOAA IGRA (www.ncdc.noaa.gov/data-access/weather-balloon/integrated-global-radiosonde-archive)

flow, the flow direction was essentially identical to $\overline{wd}$ at all heights > h, while within the canopy, the flow was often turned toward row-parallel (Section 2.3). A rotation of the data from the in-canopy anemometers based on $\overline{wd}$ would have resulted in "streamwise" velocities that would not have been representative of the actual wind speed nor oriented in the direction of the actual mean wind at those heights. Thus, the wind components oriented perpendicular to ($u_\perp$) and parallel to ($v_\parallel$) the vine row direction were studied using an approach similar to that used in urban street-canyon flows (e.g., Klein et al., 2007). This method allowed for straightforward interpretations of the patterns seen in the canopy, especially when defining those patterns based on $\overline{wd}$.

The use of a row-parallel and -perpendicular horizontal coordinate system, combine with collapsing dependencies to the 90° range of $|\delta|$ required that $u_\perp$ and $v_\parallel$ be defined as positive in the direction most similar to the primary wind direction. For example, if the mean wind direction was from the southeast at some height, $u_\perp$ was considered positive from the east and $v_\parallel$ was positive from the south.

Although a traditional 3D rotation like a planar fit was not employed, a correction was performed in order to remove a topographical signature discovered in the data. The vineyard location was chosen in part because it is relatively flat, but a slight slope did exist within the tower footprint area. The slope was steepest along a line from ≈ 225° to ≈ 45° and had a downward sloping gradient between ≈ 4% and ≈ 7% depending on the footprint size considered. Many different approaches—including planar fits and moving averages—have been used to correct vertical velocity biases created by topographical influences (Shimizu, 2015). Here, because there were significantly more periods with winds from some directions than others, ensemble averages of the vertical wind angle $\left(\theta = \tan^{-1}\left(\overline{w}/\sqrt{\overline{u_\perp}^2 + \overline{v_\parallel}^2}\right)\right)$ were calculated from the uncorrected data for each 5° compass sector. Examination of the θ versus $\overline{wd}$ data then revealed that a nearly identical and approximately sinusoidal relationship existed for each of the top four anemometers. A sine function that was the average fit to all of the data from the top four anemometers was determined (θ = 2.61°sin(44.18°+$\overline{wd}$)) and was then used to determine the amount of correction needed for θ for each individual period. Using the fit-determined correction, the appropriate vector rotation was applied so

that the topography-induced momentum in w was removed and redistributed into $u_\perp$ and $v_\parallel$. This approach is essentially a combination of the approaches of Su et al. (2004) and Aubinet et al. (2005) and is conceptually identical to an ideal planar fit method (Vickers and Mahrt, 2006). If a constant non-zero mean w needed to be removed, a translation term could be added to the sine fit. That was not done here. Interestingly, the maximum and minimum of the sine function occurred at $\approx 45^\circ$ and 225°, respectively, and therefore matched with the trajectory of the steepest downhill slope in the area immediately around the meteorological tower. The amplitude of the function (2.61°) was equivalent to a 4.5% grade.

2.3 Results

Wind roses of the incoming wind speed and direction of all of the usable periods, regardless of the stability classification, indicated that the wind approached from two primary directions throughout the campaign (Fig. 2.2). It was also seen that the wind speed generally increased with height and that the flow typically became channeled into the vine row direction at the mid-canopy height, the same as in M15. In periods when the flow above the canopy was from the southwest, the flow at the mid-canopy was typically from the south while the flow often appeared to be from the south-southeast in the understory, thus giving similar appearance to the continuous counter-clockwise rotation of the velocity with depth into the canopy reported in Su et al. (2008). In contrast, this same continued rotation into the understory was not seen in the profiles of the velocity for any of the periods with $\overline{wd}$ in the northern quadrant. This suggested that the south-southeastern understory flow was more likely caused by some other effect like local inhomogeneities in the vines. This behavior could not be observed in M15 because no anemometer was deployed in the understory.

2.3.1 Velocity

The turning and channelling of the velocity profile was also observed in the velocity components. When $\overline{wd}$ was *parallel* to the vines, the mean value of the velocity component that was also parallel to the rows was always roughly equal to the mean wind magnitude $\left(M = \overline{\sqrt{u_\perp^2 + v_\parallel^2}}\right)$ at all heights and at the mid-canopy, it was usually

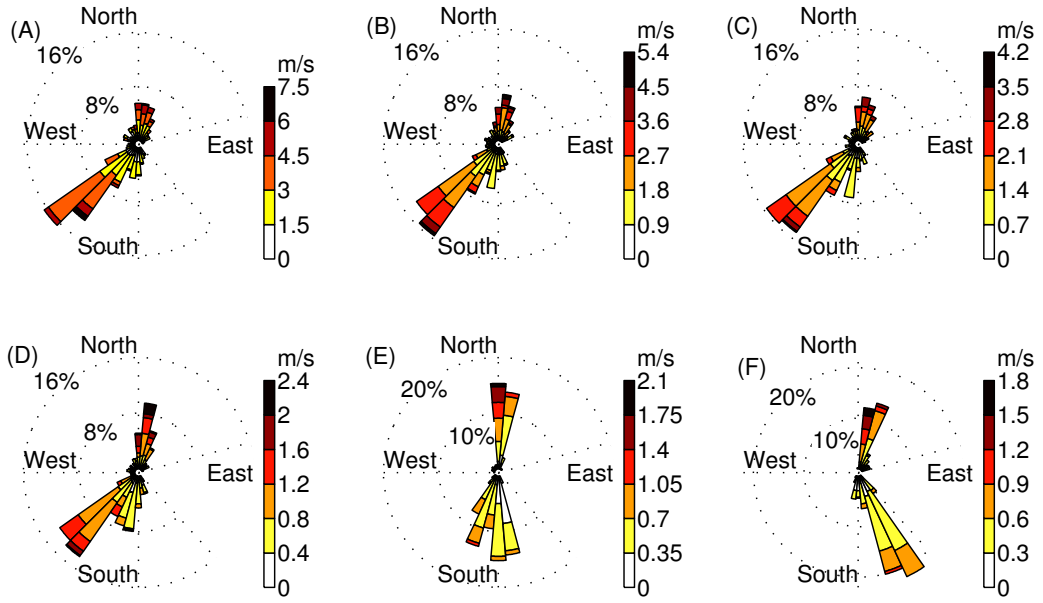

Figure 2.2: Wind roses for the six anemometers using all the usable 30-minute periods. The z = 10.1 m, 5.0 m, 3.0 m, 2.0 m, 1.4 m, and 0.7 m anemometers are shown as (A) through (F), respectively. Vines were oriented north to south.

> 10 times larger than $\overline{u_\perp}$ (Fig. 2.3A). When $\overline{wd}$ was *perpendicular* to the vine rows, $\overline{u_\perp}$ was larger than $\overline{v_\parallel}$ at all heights > h during N periods. At the lowest two anemometer heights, $\overline{v_\parallel}$ became significant and was > $1.2\overline{u_\perp}$ at the mid-canopy anemometer on average. The behavior of the MC periods was essentially indistinguishable from the N periods.

During MS periods, the rotation of the profiles was prevalent at much higher heights than during N periods in each of the categories with $|\delta| > 24°$. In the *perpendicular* category specifically, even though $\overline{u_\perp}$ was > $\overline{v_\parallel}$ at z = 10.1 m, the two became nearly equivalent at 5.0 m, and $\overline{v_\parallel} > 1.4\overline{u_\perp}$ at 3.0 m. In contrast, turning during N periods was almost entirely confined to heights near or below h. This demonstrated that although some amount of rotation was present in the profiles regardless of the stability class, the enhanced rotation of the MS profiles was likely caused by an enhanced connectivity between the canopy and the surface layer, perhaps due to suppressed mixing during the MS periods.

Comparable behaviors were observed in the standard deviations of $u'_\perp$ and $v'_\parallel$ (Fig. 2.3B). For all but the N *near-perpendicular* and *perpendicular* periods and the MC *perpendicular* periods (not shown), $\sigma_{v'_\parallel}/\sigma_{u'_\perp}$ was > 1.0 at all heights on average. This ratio tended to be highest for MS periods and periods with low $|\delta|$ values. For those categories where $\sigma_{u'_\perp}$ was > $\sigma_{v'_\parallel}$ at some height, the largest difference in $\sigma_{u'_\perp}$ and $\sigma_{v'_\parallel}$ was always at the anemometer nearest to $z = h$. At the two anemometer heights that were well within the canopy, those same categories had $\sigma_{v'_\parallel} > \sigma_{u'_\perp}$, showing that even for *perpendicular* periods, the along-row mixing dominated cross-row mixing in the lower canopy.

Profiles of ensemble averages of the wind magnitude, M (Fig. 2.4A) and the standard deviation of M (Fig. 2.4B) followed closely with well-documented profiles of streamwise velocity from other canopies (e.g., Dupont and Patton, 2012). However, slight variations in these profiles based on the stability and directional categories were apparent. Within each stability category, the wind speed below h was always closer to M_h under *parallel* conditions than under *perpendicular* conditions, and *perpendicular* periods typically had higher values of $\sigma_{M'}/u_{*,h}$ than did *parallel* periods at all heights.

The inflection in the velocity profile is known to lead to turbulence-causing insta-

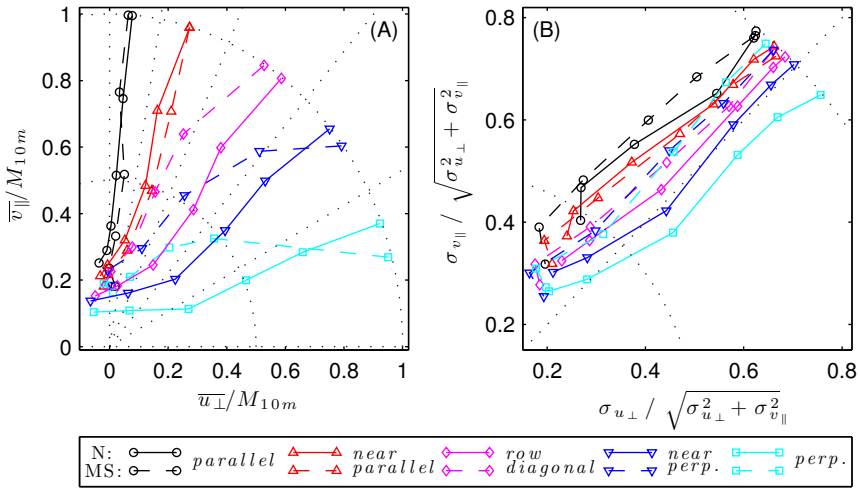

Figure 2.3: Hodographs of the N and MS periods for each δ category (A) and of the scaled standard deviations of the velocity components (B). In (A), $\overline{u_\perp}$ and $\overline{v_\parallel}$ were set as positive at the uppermost anemometer regardless of the quadrant of $\overline{wd}$ for each periods. The signs of $\overline{u_\perp}$ and $\overline{v_\parallel}$ at each other anemometer were determined appropriately based on the sign corrections applied to the values at the highest anemometer. In both (A) and (B), the MC periods' behavior was indistinguishable from the N periods and was therefore excluded for clarity.

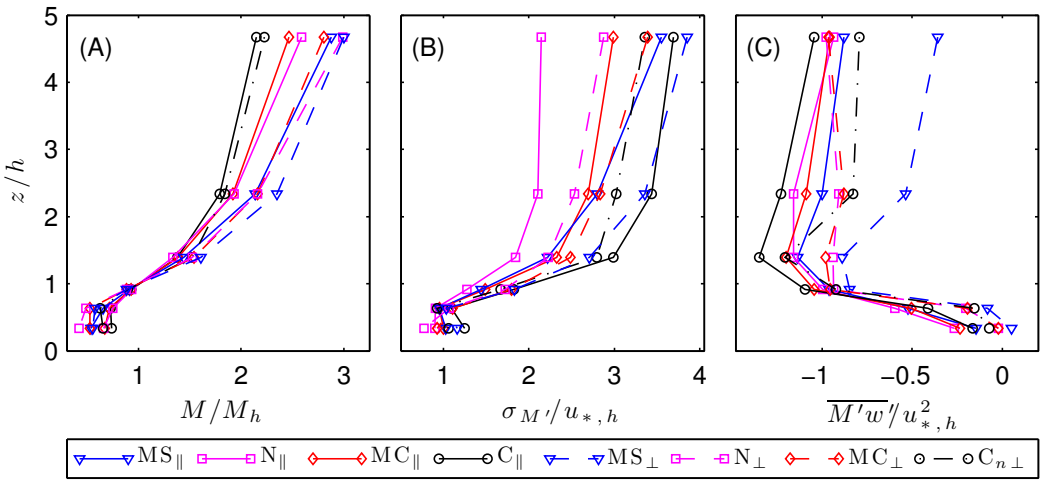

Figure 2.4: Vertical profiles of the mean wind velocity magnitude (A), standard deviations of the wind magnitude (B), and vertical momentum flux determined using the wind magnitude (C). Each stability class for the *parallel* and *perpendicular* categories is shown. The *near-perpendicular* periods were used for the C category in place of the *perpendicular* periods (Section 2.2.1).

bility (Robinson, 1991) and has led many to compare CSL flows to standard mixing layers (Raupach et al., 1996; Finnigan, 2000). The shear length scale $\left(L_s = M_h / \frac{dM}{dz}|_h\right)$ has been used to compare the two and has been shown to vary inversely with canopy density (Bailey and Stoll, 2013). The shear length scale was determined and was studied as a function of δ (Fig. 2.5). Regardless of the stability class, L_s tended to decrease with $|\delta|$. For the N periods specifically, it decreased from $\approx 1.3h$ to $\approx 0.7h$ as $|\delta|$ increased from 0° to ≈ 42° and then appeared to stay relatively constant for $|\delta| > 42°$. The change in slope at $|\delta| = 42°$ was used as justification for the directional category threshold chosen in Section 2.2.1. L_s values from the MC periods were very similar to those of the N periods except at the lowest values of $|\delta|$, for which the L_s values were slightly lower. The MS, L_s values showed considerably more variation than the other stability classes, and although they too were similar to the N values for most δ, they were lower than both the N and MC values for $|\delta| < 25°$. A decrease in L_s with increased static atmospheric stability was also observed in Dupont and Patton (2012).

The decrease in L_s as a function of $|\delta|$ was likely caused by the same effect that causes the density dependence reported by Bailey and Stoll (2013). Specifically, when the winds were roughly parallel to the vine row direction, the frontal area of the vines normal to the wind was relatively small compared to the frontal area seen by row-orthogonal winds. This change in the frontal area behaved similarly to a change in canopy density. This is also supported by the 2011 L_s values being lower on average than the 2013 values for most values of δ—especially for $|\delta| > 38°$–a result that was likely modulated by the LAI (i.e., density) which was larger in 2011 than in 2013.

The shear length scale, as part of the canopy mixing layer analogy, is related to both the vorticity thickness and the average streamwise spacing of structures (Λ) induced by instabilities (Finnigan, 2000). This relationship is believed to be weakened for $L_s > 0.6h$, where Λ becomes approximately constant with a value of $\approx 5h$ (Huang et al., 2009; Bailey and Stoll, 2013). As such, the reduction in L_s with $|\delta|$ could mean that *parallel* periods had a thicker layer of larger structures than did the *perpendicular* periods which had a thinner layer of smaller structures. Because L_s/h was $> 0.6h$ for

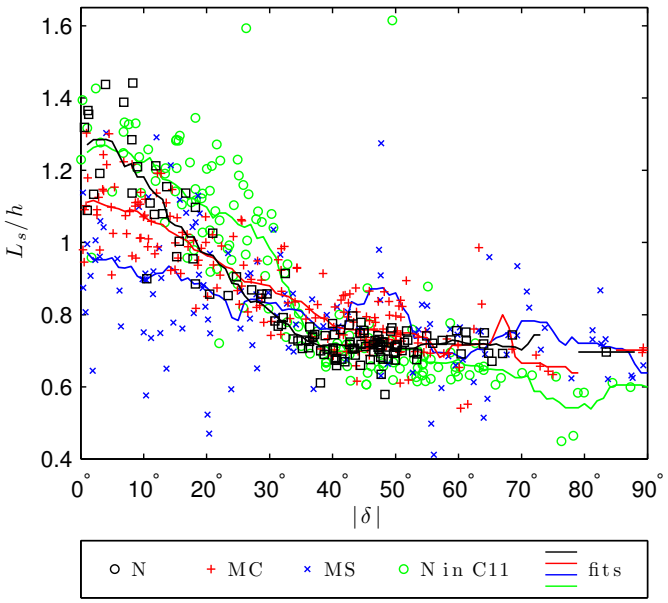

Figure 2.5: The integral shear length scale at the canopy top versus $|\delta|$. The lines represents a moving average of the depicted data with a 10° window size.

all δ, Λ likely stayed relatively constant at $\approx 5h$ for all the periods. One weakness in this conclusion, however, is that it requires that L_s be determined at the height of maximum shear, which may or may not have been at $z = h$ for all δ. For *parallel* periods, the maximum shear typically occurred at $z \approx 3$ m (not shown). L_s values determined at that height were still larger on average than were the values determined for *perpendicular* periods at their height of maximum shear ($z \approx h$), but the trend in L_s/h was less coherent. It was not unexpected that the height of maximal shear would occur at $z > h$ for the *parallel* periods. For L_s values $\geq h$, the ground causes the core of shear-induced structures to be displaced upward to a height above the canopy resulting in an asymmetry in the roller structure at the canopy top. Bailey and Stoll (2016) showed this asymmetry and reported that the roller structure centerline occurred at $z \approx 1.4h$. This equated to $z \approx 3$ m here, consistent with the height at which the inflection in the velocity profile was observed for *parallel* periods.

In addition to the profiles of the velocity magnitude and its components, profiles of higher order velocity statistics showed variability with both wind direction and stability. The standard deviation of the vertical velocity ($\sigma_{w'}$) tended to be the lowest near the ground and increased in value from there to the canopy top (Fig. 2.6A). Above the canopy, the values for all but the most convective periods stayed relatively constant with height, consistent with other studies (e.g., Raupach et al., 1996). The most unstable periods showed a continuous increase in $\sigma_{w'}$ with height and the *parallel* periods specifically did not collapse well with the other profiles. This was likely caused by the difference in u_* and w_* (Section 2.2.1). Values of $\sigma_{w'}/u_{*,h}$ tended to be lower for increased stability, consistent with all but the most stable cases in Dupont and Patton (2012). In the canopy, values of $\sigma_{w'}/u_{*,h}$ were typically lower for periods of *perpendicular* flow than for periods of *parallel* flow. This behavior may be similar to the wake and non-wake effects reported for $\sigma_{w'}$ in Böhm et al. (2013). This was exactly the opposite of the behavior of $\sigma_{M'}/u_{*,h}$ which was larger for *perpendicular* periods than for *parallel* periods within the canopy, thus suggesting a trade-off between vertical and ground-parallel mixing in the lower canopy as $\overline{wd}$ changes.

In the CSL, the skewness of the vertical velocity ($Sk_{w'}$) typically had its most

negative values in each profile near the mid-canopy height (Fig. 2.6D). This is consistent with both experimental and simulated data of other canopy flows (Dupont and Patton, 2012; Bailey and Stoll, 2013; Pan et al., 2014). At the mid-canopy height, the *perpendicular* periods were always more negative than were the *parallel* periods of the same stability class. *Perpendicular* periods also exhibited a large increase in $Sk_{w'}$ between the mid-canopy and the lowest anemometer height, typically reaching values near zero in the understory. The profiles of *parallel* periods presented significantly less change in $Sk_{w'}$ in the lower portions of the canopy and were more negative than the *perpendicular* periods at the lowest anemometer. The behavior of the *perpendicular* and *parallel* periods within the canopy was quite similar to the $Sk_{w'}$ data reported in Böhm et al. (2013) that was taken in wake and non-wake regions, respectively, within a canopy. Similar to Dupont and Patton (2012), the N periods were generally more negative than the non-neutral periods for the anemometers at 3 m and lower. Although the profiles at $z \geq 3$ m were somewhat sporadic, nearly all of the periods had $Sk_{w'} > 0$ at heights above $z = 2h$, a result that is consistent with others' results (Bailey and Stoll, 2013; Pan et al., 2014).

The skewnesses of $u'_{\perp}$ ($Sk_{u'_{\perp}}$) and $v'_{\parallel}$ ($Sk_{v'_{\parallel}}$) were considerably different from each other. $Sk_{u'_{\perp}}$ was always relatively small during periods of *parallel* flow (Fig. 2.6B). During those periods, $\overline{u_{\perp}}$ was essentially the spanwise component of the wind and therefore would be expected to be near zero for all heights (Pan et al., 2014). $Sk_{u'_{\perp}}$ had its highest values at the canopy-top anemometer during periods of *perpendicular* flow, during which $\overline{u_{\perp}}$ was essentially the streamwise component of the wind. At the lowest anemometer height, $Sk_{u'_{\perp}}$ returned to a near-zero value, regardless of the wind direction or stability class, which agrees with Dupont and Patton (2012) and Pan et al. (2014). The skewness of the streamwise component during *parallel* periods, i.e., $Sk_{v'_{\parallel}}$, tended to decrease with $|\zeta|$ at all heights, and peaked at either the canopy top or near the ground depending on the stability class (Fig. 2.6C). The more convective periods tended to peak at the canopy top, while the N and MS periods reached their highest values at the lowest anemometer height. During *perpendicular* flow periods, the skewnesses of the row-parallel component of the wind were relatively small within the canopy. They were not as close to zero as was expected, however, and were

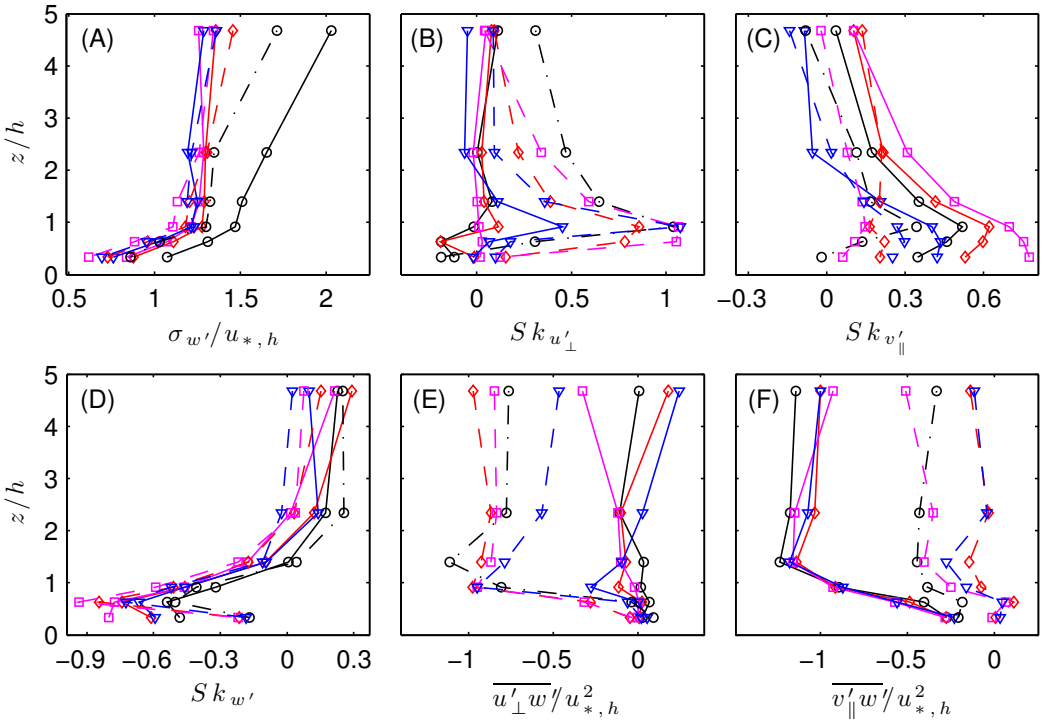

Figure 2.6: Vertical profiles of the standard deviations of the vertical velocity fluctuations (A), the skewness of the row-perpendicular (B), row-parallel (C), and vertical velocity fluctuations (D), and the vertical momentum flux based on the row-perpendicular velocity component (E) and on the row-parallel velocity component (F). The line styles match those used in Fig. 2.4.

not as small as the skewnesses of the spanwise component *parallel* periods (*solid* lines in Fig. 2.6B). Interestingly, the skewnesses of the streamwise component under *perpendicular* flow (*dashed* lines of $Sk_{u'_\perp}$ in Fig. 2.6B) were quite different from those of the streamwise component during *parallel* flow (*solid* lines of $Sk_{v'_\parallel}$ in Fig. 2.6C). While $Sk_{u'_\perp}$ during *perpendicular* times behaved similarly to documented streamwise skewness profiles taken in orchards (Dupont and Patton, 2012) and corn fields (Pan et al., 2014), $Sk_{v'_\parallel}$ during *parallel* times behaved more like the streamwise skewness profiles reported in Böhm et al. (2013) from data collected in a sparse-canopy wind-tunnel study. Well above the canopy, the skewnesses of both $u'_\perp$ and $v'_\parallel$ had values near zero, and no obvious trends with δ or ζ were apparent.

2.3.2 Momentum Flux

The vertical momentum flux based on the wind magnitude ($\overline{M'w'}$) had only a slight increase with height above the canopy regardless of the wind direction and was typically $\approx -u^2_{*,h}$ (Fig. 2.4C). This indicated that the anemometers at $z = 5.0$ and 10.1 m were in the surface layer of the atmospheric boundary layer and thus above the CSL. Within the canopy, the magnitude of the downward flux decreased quickly with depth and periods of *perpendicular* flow decreased to measurably smaller magnitudes than did *parallel* flow periods. When the vertical momentum flux was broken into its row-parallel and -perpendicular contributions, logical trends with respect to δ were observed. As expected, $\overline{u'_\perp w'}$ contributed significantly more to the total vertical momentum flux for *perpendicular* periods than it did for *parallel* periods (Fig. 2.6E). Profiles of $\overline{v'_\parallel w'}$ were the opposite and collapsed to the well-documented stress profile for canopy flows (Finnigan, 2000) during *parallel* periods and were near zero for *perpendicular* periods (Fig. 2.6F).

The net vertical momentum flux into and through the canopy is often described as being composed of two modes, referred to as sweeps (samples with $u' > 0$ and $w' < 0$) and ejections (samples with $u' < 0$ and $w' > 0$) (e.g., Finnigan, 2000). Total contributions from these two modes were determined using the quadrant hole approach with a hole size of $\mathcal{H} = 0$ (Lu and Willmarth, 1973; Bailey and Stoll, 2013). Profiles of the ratio of the contributions to the total momentum flux of ejection and

sweep events (Ej/Sw) based on both $\overline{u'_\perp w'}$ and $\overline{v'_\parallel w'}$ were plotted for comparison (Fig. 2.7). In the upper portions of the canopy, sweeps dominated ejections regardless of the stability, the directional classification, or the wind component being investigated. At heights well above the canopy ($> 4h$), ejections usually became the dominant structure as is expected for a rough-wall boundary layer (Bailey and Stoll, 2013). This behavior is typical of canopy flows (e.g., Su et al., 1998; Bailey and Stoll, 2016). In many reported Ej/Sw profiles, ejections dominated sweeps at heights as low as $1.4h$ (e.g., Bailey and Stoll, 2013), while in others, sweeps dominated ejections up to heights of $> 2h$ (e.g., Su et al., 1998; Thomas and Foken, 2007). The lower height of equivalency determined in some modeling studies was likely caused by an upper boundary that was not sufficiently far from the canopy (Bailey and Stoll, 2013). The same effect is also likely present in wind-tunnel studies. In the vineyard, sweeps dominated ejections up to heights above $2.4h$. The height at which $Ej/Sw = 1$ showed some variation with δ, stability classification, and the velocity component ($u_\perp$ or $v_\parallel$).

The Ej/Sw profiles of $\overline{u'_\perp w'}$ and $\overline{v'_\parallel w'}$ differed when *parallel* and *perpendicular* periods were compared. The profiles of Ej/Sw based on $\overline{u'_\perp w'}$ (Fig. 2.7A) compared well with other studies including Bailey and Stoll (2013) which reported vineyard canopy simulation results under perpendicular flow conditions. This included the ratio reaching a minimum of ≈ 0.55 in the upper canopy and all of the profiles, regardless of stability and wind direction, returning to a value near unity at the lowest anemometer height. *Parallel* periods tended to reach a minimum ratio at the anemometer just below h while the *perpendicular* periods tended to have a minimum ratio at the mid-canopy anemometer height.

The Ej/Sw profiles of $\overline{v'_\parallel w'}$ had notable differences from those of $\overline{u'_\perp w'}$. Although the profiles for *perpendicular* periods showed a similar minimum value to those from $\overline{u'_\perp w'}$, the location of that minimum was always at the anemometer closest to the canopy top. At the mid-canopy and canopy-bottom anemometers, the ratio was nearly always ≈ 1.0. This suggested that sweep structures in the spanwise component at the canopy top under *perpendicular* conditions were not able to penetrate the canopy very deeply. The opposite was true for the Ej/Sw profiles based on $\overline{v'_\parallel w'}$ from *parallel* periods wherein sweep events penetrated considerably farther into the

canopy than they did under *perpendicular* conditions. The Ej/Sw ratio maintained a value of ≈ 0.7 through the canopy to the lowest anemometer, a different behavior than all of the other profiles of Ej/Sw which trended towards unity in the lower canopy.

The vertical flux profiles (Fig. 2.6) and the Ej/Sw profiles (Fig. 2.7) demonstrated the directional dependence in the vertical fluxes using the *parallel* and *perpendicular* categories. The cross-vine ($\overline{u'_\perp v'_\parallel}$) and vertical flux terms of the flux tensor were also studied as a function of δ at heights within the canopy (Fig. 2.8). Only the MC and N classifications are plotted in Fig. 2.8 as they showed the most coherent trends. Periods from the other stability classifications exhibited the same general trends but were considerably more noisy. $\overline{u'_\perp v'_\parallel}$ from the mid-canopy anemometer indicated that the cross-vine flux reached its maximum magnitude at $|\delta| \approx 40^\circ$ (Fig. 2.8A). This was determined using a moving average with a 10° window size, the result of which is depicted in the figure. The fact that the maximum cross-vine flux magnitude did not occur at $|\delta| = 45^\circ$ may be attributed to the natural bias in the orientation of the leaves, which are prone to growing such that their surfaces face outward from the vine into the aisle (Mabrouk et al., 1997; Bailey et al., 2014a). Because leaf-induced drag is known to vary with orientation to the wind, the aligning of the leaf surfaces to being parallel to the vine row direction likely contributes to the nonisotropic drag that would cause the asymmetric behavior of the flux tensor (Schuepp, 1993).

Interestingly, a similar result was found in the component-based vertical momentum fluxes (Fig. 2.8B). When $\overline{u'_\perp w'}$ and $\overline{v'_\parallel w'}$ from the canopy-top anemometer—as fractions of the total stress in the canopy—were plotted against $|\delta|$, it was found that their respective contributions to $u_{*,h}$ became equivalent when $|\delta| \approx 35^\circ$. This was determined based on parabolic fits (Fig. 2.8B). When the data from the mid-canopy anemometer were used, the contributions became equivalent at $|\delta| \approx 42^\circ$ (Fig. 2.8C). We would expect that if the east-west component and the north-south component of the flow in a homogeneous canopy were used to determine vertical fluxes, the crossover point would be at 45°.

The behavior of $\overline{u'_\perp v'_\parallel}$, $\overline{u'_\perp w'}$, and $\overline{v'_\parallel w'}$ within the canopy collectively give a picture of the effect that the discrete nature of the vineyard canopy has on the CSL flow. When $|\delta|$ was either 0° or 90°, the flow behaved somewhat like a homogenous plant

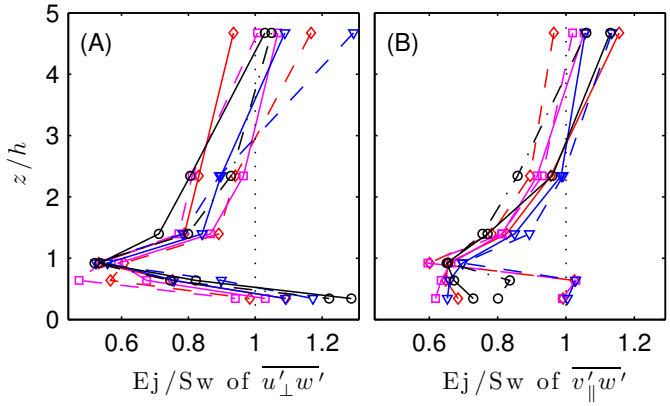

Figure 2.7: The ratio of the contribution of ejections to the contribution of sweeps in the vertical momentum flux. The ratio from the row-perpendicular component ($u'_\perp w'$) is depicted in (A) while the ratio of the flux from the row-parallel component ($v'_\parallel w'$) is shown in (B). The line styles match those used in Fig. 2.4.

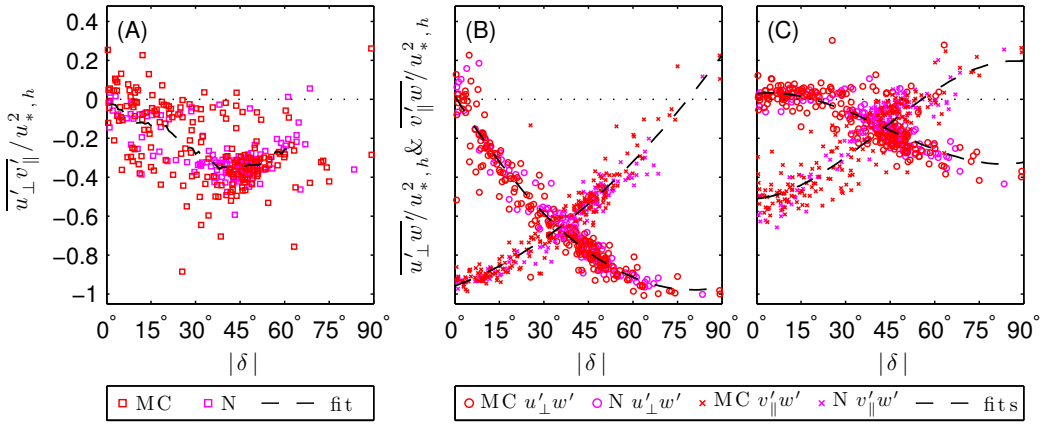

Figure 2.8: The cross-vine flux, $\overline{u'_\perp v'_\parallel}$ at $z = 0.63h$ (A), and the vertical momentum flux based on both the row-perpendicular and -parallel components at $z = 0.91h$ (B) and at $z = 0.63h$ (C). In (A), the *dashed* line represents a moving average of the depicted data with a 10° window size. The *dashed* lines in (B) depict least-squared-error parabolic fits to the data. The *dashed* lines in (C) depict least-squared-error third-order polynomial fits to the data.

canopy and somewhat like the canopies of discrete elements studied by others (e.g., Böhm et al., 2013). On the other hand, when $|\delta|$ was 45°, the flow was considerably different than what has been reported for those canopies. Although the mean flow was channelled into the vine row direction, the stress was not. At $|\delta| = 45°$, $\overline{u'_\perp v'_\parallel}$ was large but not at its peak, and $\overline{u'_\perp w'}$ was contributing more to the total stress than was $\overline{v'_\parallel w'}$. When $|\delta| \approx 40°$, $\overline{u'_\perp v'_\parallel}$ was at its largest potential value, and $\overline{u'_\perp w'} \approx \overline{v'_\parallel w'}$. The forced rotation of the velocity profile into the flow direction of least resistance by the canopy must be the cause of the asymmetric behavior of the components of the stress tensor, each of which exhibited very specific behavior as a function of δ. It is also likely that the open understory of the vineyard complicates this behavior at the lowest anemometer heights.

Of particular interest to this study were the links between the momentum flux dependence and the mean velocity profiles, and the interaction of their specific behaviors as functions of δ. One important integral parameter that provides this link is the displacement height, d. A variety of approaches have been used to estimate d (Sogachev and Kelly, 2016), but here d was determined as the center of the shear stress by integrating the stress profile as,

$$d = \frac{\int_0^h z u_*^2(z) dz}{\int_0^h u_*^2(z) dz}, \tag{2.1}$$

where $u_*^2(z)$ was the friction velocity as a function of height within the canopy (Jackson, 1981; Judd et al., 1996). The results were examined as a function of δ (Fig. 2.9). Data from C11 and C13 were used and the integration was performed on a third order polynomial fit to the stress data from the anemometers with $z \leq 3$ m. It was observed that d/h tended to increase with $|\delta|$, rising from ≈ 0.68 when $|\delta|$ was near 0° up to a value of ≈ 0.85 as $|\delta|$ approached 90°. This pattern motivated the chosen directional categorization thresholds of $|\delta| = 10°$ and 62° (Section 2.2.1) and correlates well with the ejection and sweep observations in the canopy. Specifically, under *parallel* flow, high speed air was able to penetrate deeper into the canopy, resulting in lower Ej/Sw values at the lowest anemometer. Conversely, during *perpendicular* periods, the penetration was shallower and correspondingly the displacement height was larger.

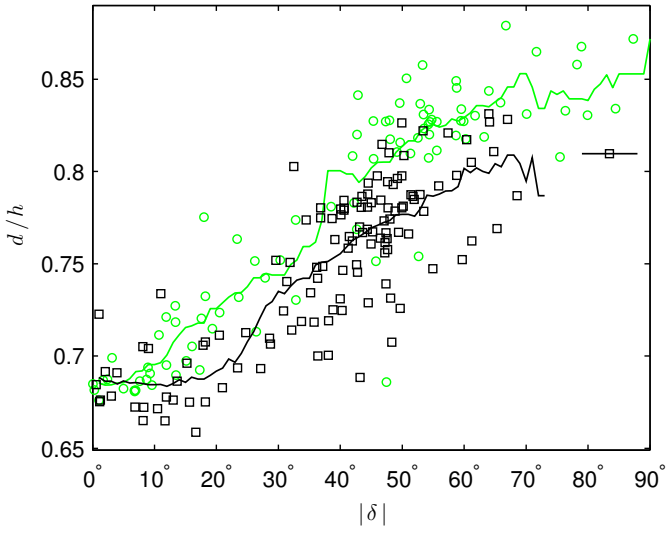

Figure 2.9: The canopy induced displacement height determined from Equation 2.1, shown versus $|\delta|$. The markers and lines match those used in Fig. 2.5.

The observed range of d/h values is nearly indistinguishable from those reported for many previous studies of different canopy types over a wide range of canopy architectures and densities (Parlange and Wilfried, 1989; Kaimal and Finnigan, 1994; Massman, 1997), including vineyard canopies (Bailey and Stoll, 2013; Chahine et al., 2014). The d/h values from C11 were larger on average for any given δ than were the values from C13. The only significant canopy differences between those years were that h was slightly larger in 2013, the LAI was lower, and the LAD profile was altered. All of these changes were due to different canopy management. Bailey and Stoll (2013) reported that for a vineyard of given h and row spacing (r_s), d varied positively with LAI for $\delta = 90°$. Bailey and Stoll (2013) also showed that for a fixed LAD within each vine, coherent eddies could not penetrate as far into the canopy as the LAI was increased by reducing r_s. This is essentially the same effect seen here as a function of δ but with a fixed r_s, specifically, as $|\delta|$ increased, penetration of coherent streamwise structures was reduced and d increased. Likely, the variation from year to year in the d/h values observed here can be attributed to the reduction in LAI from 2011 to 2013. Massman (1997) showed this same positive relationship between LAI and d, and demonstrated a relationship between d and the shape of the LAD profile for a constant LAI. In effect, if more leaf density is concentrated lower in the canopy, d is reduced compared to a top heavy LAD profile with the same LAI. The LAD profile from C11 was more top heavy than was the LAD profile determined in 2013 (Bailey et al., 2014a; Miller et al., 2015). It is likely that both the LAD and LAI changes contributed to the year-to-year difference in d/h.

The variation in d/h as a function of δ could be interpreted as a variation in the net canopy drag exerted on the flow. It would then be logical to parameterize this relationship as a function of the projected frontal area of the vines onto the plane orthogonal to $\overline{wd}$ as suggested earlier (Section 2.3.1). It could also be parameterized as a function of the effective canopy aspect ratio $(r_s - r_w)/h \sin(\delta)$, where r_w is the vine row thickness, as was used in Chahine et al. (2014) or of a sheltering effect as in Massman (1997). When $|\delta|$ was closer to 90°, the canopy likely behaved more like a dense homogenous canopy due to the continuous frontal area, while when $|\delta|$ was near 0°, the signature, on average, was more like that of a sparse canopy because of

the discontinuous frontal area of vines. A simple test of d/h versus $\sin(\delta)$ showed an 82% correlation. This, combine with eddy-penetration results from Bailey and Stoll (2013), would also suggest that the limits of d/h over the full range of δ would be altered if there were a significant change in r_s/h or r_w/h. Such a difference would be essentially equivalent to a change in overall canopy density if the general shape of the LAD profiles was maintained.

2.3.3 Turbulent Kinetic Energy

The total turbulent kinetic energy per unit mass ($\overline{e} = 0.5\overline{u_i'^2}$, where u_i follows index notation as defined in Appendix 1), being essentially the combination of $\sigma_{M'}$ and $\sigma_{w'}$, exhibited similar behavior to them as a function of both δ and height. $\overline{e}$ was always larger above the canopy than in the canopy and also increased as a multiple of $u_{*,h}^2$ with increasing $|\zeta|$. The combination of these effects also resulted in a larger increase in $\overline{e}$ across the canopy top during periods of large $|\zeta|$ compared to periods of nearly neutral stability. Above the canopy, $\overline{e}$ was typically larger during *perpendicular* periods than it was during *parallel* periods. The opposite was true within the canopy. At both the $z = 0.7$ and 1.4 m anemometer heights, every *perpendicular* N period had a lower value of $\overline{e}/u_{*,h}^2$ than every *parallel* N period. The combination of the z and δ dependencies resulted in the ratio of $\overline{e}$ at $z = 1.4$ m to that at $z = 5.0$ m decreasing by $\approx 2/3$ on average as the winds moved from *parallel* to *perpendicular*. This was the case during N periods from both C11 and C13. MS and MC periods also exhibited a decrease, but significantly more spread was observed. This decrease with $|\delta|$ was not unlike the decrease in L_s and the two were likely interrelated. Following the mixing layer analogy, smaller L_s values like those seen during *perpendicular* periods suggest a thinner vorticity thickness composed of smaller structures possibly spaced more closely together. Combine this with the higher d values and the reduced structural penetration depth of the same periods and it is logical that calmer conditions (lower $\overline{e}$) would exist at the mid-canopy and below.

The components of the budget of $\langle\overline{e}\rangle$, where angled brackets represent a spacial average (see Appendix 1), were investigated for their relationship with δ. The average transport budget equation of $\langle\overline{e}\rangle$ in the canopy, using the coordinate system developed

here, was derived as,

$$
\begin{aligned}
0 = &-\left[\langle\overline{u'_\perp w'}\rangle\frac{\partial\langle\overline{u_\perp}\rangle}{\partial z} + \langle\overline{v'_\parallel w'}\rangle\frac{\partial\langle\overline{v_\parallel}\rangle}{\partial z}\right] \\
&-0.5\frac{\partial}{\partial z}\left[\langle\overline{w'u'^2_\perp}\rangle + \langle\overline{w'v'^2_\parallel}\rangle + \langle\overline{w'^3}\rangle\right] \\
&-\left[\langle\overline{u_\perp}\rangle\frac{\partial}{\partial z}\langle\overline{u'_\perp w'}\rangle + \langle\overline{v_\parallel}\rangle\frac{\partial}{\partial z}\langle\overline{v'_\parallel w'}\rangle\right] \\
&+ g\frac{\overline{w'T'}}{\overline{T}} - \epsilon - \mathcal{R}.
\end{aligned}
\tag{2.2}
$$

Details on the individual terms, the nomenclature, and the assumptions used for this equation are shown in Appendix 1. For reference, the first three lines on the right-hand side of Equation 2.2 are shear production, turbulent transport, and wake production of $\overline{e}$, respectively. The terms on the fourth line are buoyancy production, dissipation, and the budget residual. Because of the coordinate system used here, this form differs slightly from that used by others (e.g., Brunet et al., 1994; Kaimal and Finnigan, 1994).

The dissipation of $\langle\overline{e}\rangle$ was calculated using the second-order longitudinal structure function based on Kolmogorov's 2/3 law as,

$$
\epsilon = \left\langle\!\!\left\langle \frac{D_{uu}(r)^{3/2}}{C^{3/2}r} \right\rangle\!\!\right\rangle, \tag{2.3}
$$

where $D_{uu}(r) = [\![(u_s(x_s + r) - u_s(x_s))^2]\!]$ is the longitudinal structure function, u_s is the wind velocity aligned along the streamwise axis (x_s) at each height, r is a separation distance between readings of u_s along the streamwise axis determined by assuming Taylor's frozen turbulence hypothesis, C is a constant, and the $[\![\,]\!]$ represent an average over all possible velocity pairs separated by r within a single 30-minute period (Monin and Yaglom, 1975; Saddoughi and Veeravalli, 1994). The $\langle\!\langle\,\rangle\!\rangle$ represent an average taken over the inertial subrange, which is the range of scales over which isotropy can be assumed and the ratio of D_{uu} and $r^{2/3}$ is approximately constant. The inertial subrange was defined here as all r greater than 0.1 m and smaller than $(z - d)/2$ for the top two anemometer heights and smaller than d for the lowest four anemometer heights. This range of r assured that only the appropriate portion of D_{uu} versus r was used in the inertial-subrange averaging, and is very similar to the ranges identified by others as appropriate for a 2/3 power relationship between D_{uu}

and r (Monin and Yaglom, 1975). Although the use of Taylor's frozen turbulence hypothesis is not strictly valid within the CSL, it has often been used in similar applications to this (e.g., Nelson et al., 2011). Additionally, considerable quality checking was performed to ensure that isotropy was indeed observed in the data in the range of r used and it was determined that this approach was satisfactory even for the discontinuous vineyard canopy. Regardless of these assurances, the values determined in this manner should be treated with caution and conclusions based on its use should be validated in other ways when possible (this is done in Section 2.3.4). The constant coefficient C has been reported with values ranging from 1.5 to 2.3 and a value of 2.0 was used here (Monin and Yaglom, 1975; Stull, 1988; Pope, 2000).

Examination of the contributions of the individual terms of Equation 2.2 indicated a dependance on δ and on stability (Fig. 2.10). The shear production typically dominated the wake production term and usually reached its peak at or just above the canopy. This was similar to the shear production peak observed in other canopies (e.g., Christen et al., 2009; Böhm et al., 2013). The portion of the shear production based on $v_{\parallel}$, i.e., $\langle\overline{v'_{\parallel}w'}\rangle\partial\langle\overline{v_{\parallel}}\rangle/\partial z$, was dominant over the portion based on $u_{\perp}$ during *parallel* periods. The opposite was true during *perpendicular* periods. During the *row-diagonal* periods, the two portions were nearly equivalent in their production contributions, i.e., $\langle\overline{u'_{\perp}w'}\rangle\partial\langle\overline{u_{\perp}}\rangle/\partial z \approx \langle\overline{v'_{\parallel}w'}\rangle\partial\langle\overline{v_{\parallel}}\rangle/\partial z$. At z = 2 m, the total production due to shear, taken as the sum of the two components of the shear production term, increased by > 50% during N periods as $|\delta|$ increased from 0° to 90°. This increase was attributed mostly to the increase in $d\langle\overline{u_{\perp}}\rangle/dz$ with $|\delta|$, which was considerably more significant than the corresponding decrease in $d\langle\overline{v_{\parallel}}\rangle/dz$. As would be expected, $d\langle\overline{u_{\perp}}\rangle/dz$ was ≈ 0 for *parallel* winds and reached its maximum during *perpendicular* periods. This behavior was consistent for all of the stability classes. At z = 3 m, the total shear production was larger than it was at z = 2 m when δ = 0°. As $|\delta|$ increased to 90°, however, the total shear production at z = 3 m decreased by $\approx$ 25%, resulting in less total shear production at that height than at z = 2 m during *perpendicular* periods. Thus, the height at which peak shear production took place decreased from $z \approx 3$ m to $z \approx 2$ m over the limits of $|\delta|$. This was particularly obvious during N periods but was again relatively consistent for all stability classes. Finally, for MC

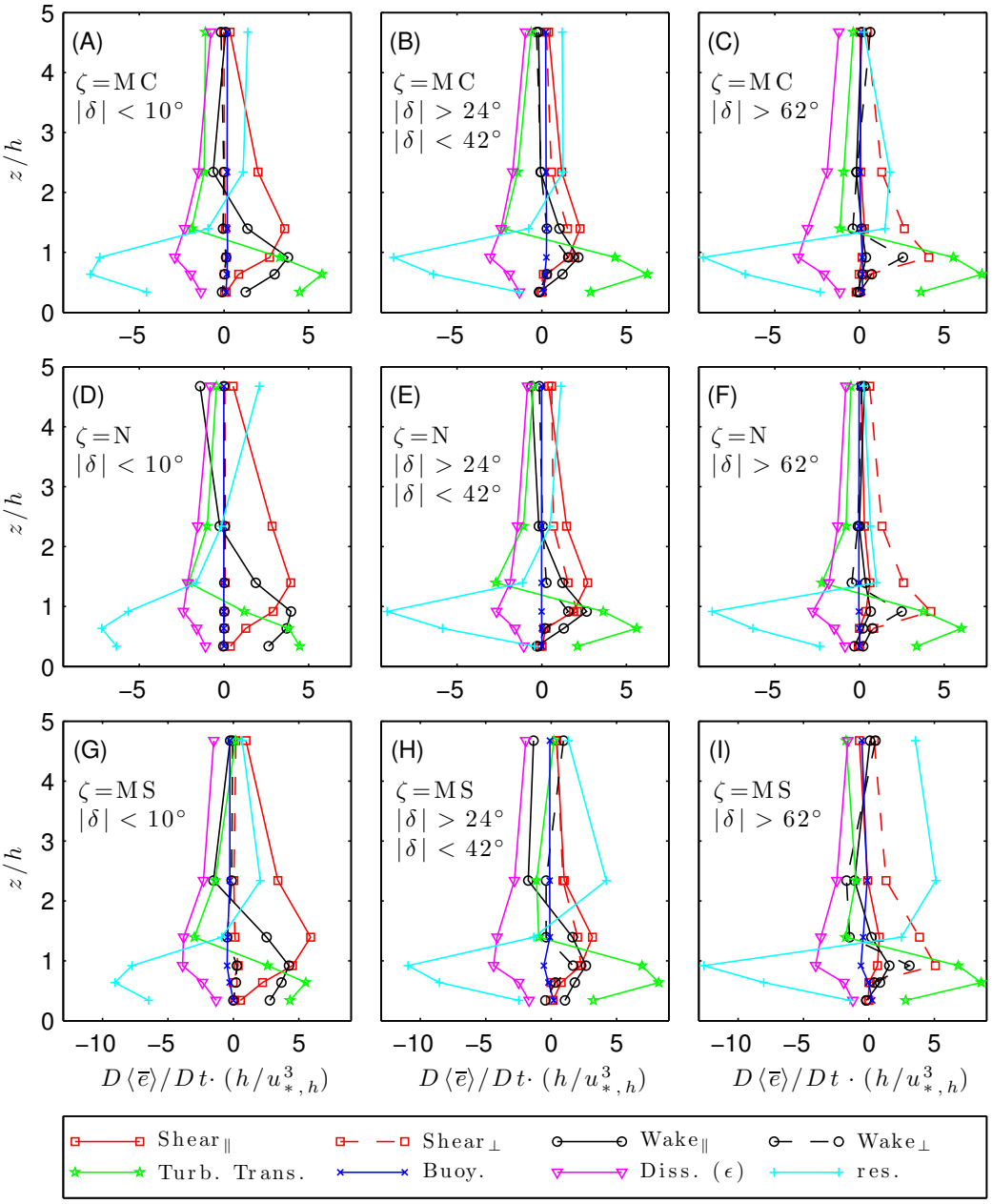

Figure 2.10: Vertical profiles of the terms of the budget of $\langle \overline{e} \rangle$ (Equation 2.2). (A), (B), and (C) show MC periods, (D), (E), and (F) show N periods, and (G), (H), and (I) show MS periods. (A), (D), and (G) show *parallel* periods, (B), (E), and (H) show *row-diagonal periods*, and (C), (F), and (I) show *perpendicular* periods.

and N periods, the total shear production at the mid-canopy anemometer height tended to decrease over $0° < |\delta| \leq 42°$ and then slowly increase again for $|\delta| > 42°$. At the mid-canopy anemometer, the total shear production decreased to < 30% of its *parallel* value when the winds were *row-diagonal*. It then recovered to ≈ 65% of its *parallel* value when the winds were *perpendicular*. This was linked to the behavior of the vertical momentum flux components at the mid-canopy (Fig. 2.8C) and to the behavior of the velocity gradients with $|\delta|$ which was somewhat similar to that seen above the canopy as described previously. At the mid-canopy, the MS periods simply showed a general decrease in the total shear production of $\langle\overline{e}\rangle$ with $|\delta|$. The behavior of the shear production of $\langle\overline{e}\rangle$ at all heights was consistent with the canopy mixing-layer analogy arguments made with relation to L_s (Section 2.3.1). Specifically, the thicker mixing layer centered near z = 3 m that likely existed during *parallel* periods decayed into a thinner layer centered near $z = h$ during *perpendicular* ones.

The components of the wake production term also shifted their dominance as $|\delta|$ increased. Specifically, they followed a logical patten where $\langle\overline{u_\perp}\rangle\partial\langle\overline{u'_\perp w'}\rangle/\partial z$ dominated during *perpendicular* periods, $\langle\overline{v_\parallel}\rangle\partial\langle\overline{v'_\parallel w'}\rangle/\partial z$ dominated during *parallel* periods, and $\langle\overline{u_\perp}\rangle\partial\langle\overline{u'_\perp w'}\rangle/\partial z \approx \langle\overline{v_\parallel}\rangle\partial\langle\overline{v'_\parallel w'}\rangle/\partial z$ during *row-diagonal* periods. The wake production was always strongest at the canopy top regardless of δ, similar to other canopy flows (e.g., Raupach et al., 1996; Böhm et al., 2013). At that height, the sum of the two normalized wake-production components decreased by ≈ 40% with $|\delta|$ during N periods, suggesting that the total wake production was of more significance to the total budget during *parallel* periods than during *perpendicular* times at the canopy top. This was primarily caused by an asymmetric balance between $u_\perp$ and $v_\parallel$ over the full range of δ. When δ was zero, $u_\perp = 0$ and $v_\parallel = 4u_{*,h}$. When $|\delta| = 90°$, $v_\parallel = 0$ and $u_\perp = 2u_{*,h}$. Tests using other normalizations (in place of u_*^3) suggested that the reduction in the relative contribution of the wake production term was likely due more to the increase in the contribution of the shear production rather than an actual reduction in the magnitude of the wake production term. Finally, as $|\delta|$ increased, the height below the peak at which the total wake production appeared to return to zero tended to increase. As a result, the span of heights over which the wake production was significant decreased with $|\delta|$ even though the height of the peak stayed constant

at $z \approx h$.

The turbulent transport term behavior was similar to other studies (e.g., Raupach et al., 1996; Christen et al., 2009). It was negative just above h, positive within the canopy, and reached a peak magnitude near $h/2$. Here, it also appeared that for *parallel* periods, the turbulent transport at the mid- and lowest-canopy anemometers was nearly equal. As $|\delta|$ increased away from *parallel*, however, the mid-canopy turbulent transport generally increased while the lowest level anemometer showed a decrease. This led to an upward shift in the height of the peak turbulent transport magnitudes and a much sharper gradient in turbulent transport in the lower canopy. This is another indicator of the generally less turbulent flow conditions in the lower portions of the canopy for increased $|\delta|$. Despite the turbulent transport term's behavior with δ, it expectantly remained the most significant source of $\langle \overline{e} \rangle$ in the lower canopy for all δ (Finnigan, 2000).

The magnitude of the buoyancy production term was considerably smaller than the other production terms and for the N and MC periods, it was nearly constant with height. During MC periods, it was generally positive for all values of δ and at all heights. The buoyancy term was generally negative for MS periods and therefore acted as a sink at all heights except for the lowest one, at which it became positive for most of the MS periods. The same convergence of the vertical heat flux into the canopy presented in M15 was seen in the 2013 data (not shown). This convergence was the likely cause of the similar shape in the buoyancy profiles regardless of δ. The flux convergence and sign change of the buoyancy terms agree with the idea that CSLs stay relatively neutral under a wide range of conditions due to canopy induced mechanical mixing (Christen et al., 2009).

The dissipation of $\langle \overline{e} \rangle$ was found to be the most negative near the canopy top, and to follow a shape similar to that reported by many others (e.g., Meyers and Baldocchi, 1991; Brunet et al., 1994; Yue et al., 2008). The magnitude of the dissipation decreased considerably with decreasing height into the canopy and with height above the canopy, where it essentially mirrored the trends seen in the sum of the shear production terms.

Finally, as is often the case in studies of this type, the residual term tended to

be the term of highest magnitude within the canopy and was essentially balancing the major production terms at those heights (e.g., Brunet et al., 1994; Böhm et al., 2013). At the canopy top, the residual tended to increase somewhat with increasing $|\delta|$. This may indicate an increase in the relevance of the unresolved dispersive flux terms as $|\delta|$ increased.

2.3.4 Energy Spectra

The spectral energy densities ($E_{u_i}(f)$) of the three components of the wind velocity were investigated at each of the anemometer heights for each of the directional and stability classifications. The energy densities were premultiplied by the frequency (f), normalized by $u_{*,h}^2$, and were studied as a function of $fh/M(z)$. The quantity $fh/M(z)$ can be interpreted as the ratio between the dominant canopy length scale h and a turbulence length scale associated with f (through Taylor's frozen turbulence hypothesis) at each anemometer height. This was especially useful when comparing the scaled frequency associated with the most dominant turbulent scale, i.e., the frequency at the peak of the premultiplied spectra ($fh/M|_{max}$), across multiple heights and directional-stability classes. The premultiplied spectra were smoothed by a log-linear binning of fh/M and by taking ensemble averages within each category. The scaling used here resulted in a collapse of the inertial subranges of the spectra taken from each anemometer height, regardless of the velocity component being studied. Although the periods from the C and S stability classes were not extensively investigated as part of this work, and the spectra from those classes are not depicted here, the values of $fh/M|_{max}$ for those classes were determined so comparisons could be made to the other classes.

The spectra of w (Fig. 2.11) demonstrated that the dominate scale of energy production in w was typically larger than the local canopy scales (h, r_s) regardless of the anemometer height. For frequencies much smaller than $fh/M|_{max}$, at which $M(z)/f$ was also larger than z, the anemometers saw only random "outside effects" and the spectra varied linearly with the frequency, resulting in a +1 slope in that region. The inertial subrange (ISR), at frequencies above $fh/M|_{max}$, never appeared to have a constant $-2/3$ slope. This was not unexpected for the anemometers within

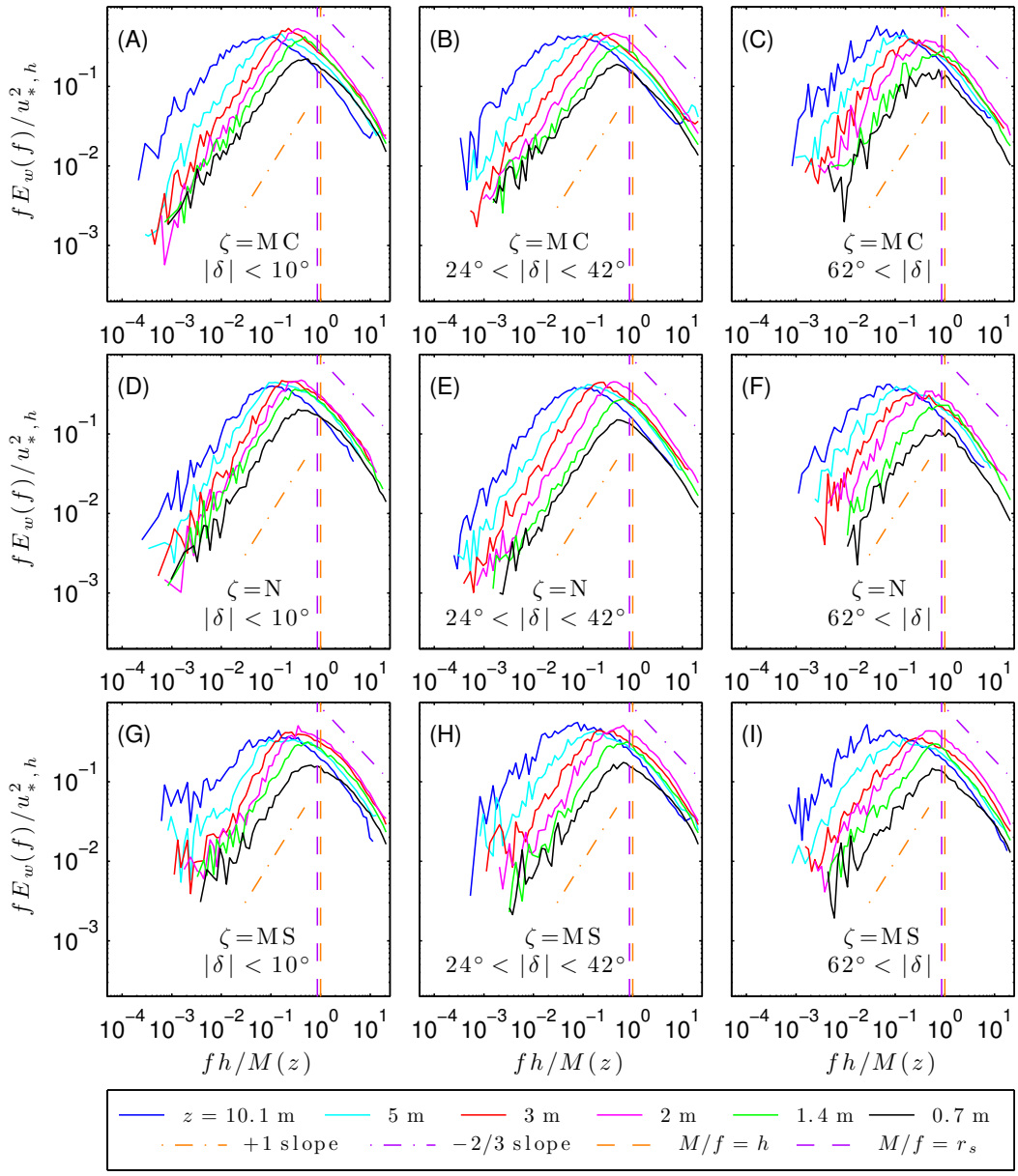

Figure 2.11: Ensemble-averaged premultiplied spectral densities of the vertical velocity for three of the directional and three of the stability classifications. (A), (D), and (G) show *parallel* periods, (B), (E), and (H) show *row-diagonal* periods, and (C), (F), and (I) show *perpendicular* periods. (A), (B), and (C) show MC periods, (D), (E), and (F) show N periods, and (G), (H), and (I) show MS periods.

the canopy, but even those well above the canopy never showed a consistent range of frequencies for which the spectral slope was −2/3. This is discussed in more detail below.

The non-dimensional frequency associated with the peak in the premultiplied w spectra, $fh/M|_{max}$, showed variation as a function of z, ζ, and δ (Fig. 2.12). The change in $fh/M|_{max}$ with z for the anemometer heights above the canopy was expected simply because a constant length scale, h, was used in the scaling instead of z (Perry et al., 1986). Within the canopy, however, $fh/M|_{max}$ became nearly constant with z and had a value that suggested that the dominant turbulent length scale was typically only slightly larger than h (Fig. 2.12A). The data from both C11 and C13 showed that $fh/M|_{max}$ usually increased with stability regardless of the wind direction or the anemometer height (Fig. 2.12B). This is in line with Kaimal and Finnigan (1994) and meant that as the stability increased, the dominant turbulent scale within the flow trended from larger to smaller scales and approached h in the lower portions of the canopy for the most stable periods. $fh/M|_{max}$ tended to increase with $|\delta|$ within the canopy and to stay relatively constant—or slightly decrease—with $|\delta|$ above the canopy. This was consistent across the MS, N, and MC classes (only the N periods are depicted). At the mid-canopy and lowest anemometers specifically, $fh/M|_{max}$ increased by > 50% and > 79% as $|\delta|$ increased from 0° to 90°, respectively (Fig. 2.12C). A value of $fh/M|_{max}$ of 0.86 (= h/r_s) is equivalent to the dominant length scale of the w-spectra being equal to r_s. This was very similar to the values seen in the lower canopy during *perpendicular* periods and periods with $\zeta > 0$. The increase in $fh/M|_{max}$ with $|\delta|$ was likely related to the change in the height of the velocity profile's inflection point which was previously described as having moved from $\approx 1.5h$ to $\approx h$ as $|\delta|$ passed from *parallel* to *perpendicular*.

If M_h had been used in place of $M(z)$ in the scaling of fh as done by others (e.g., Dupont and Patton, 2012), $fh/M_h|_{max}$ would still have increased with $|\delta|$ but not as dramatically. This is explained by the fact that $M(z)$ within the canopy changes more dramatically with δ than does M_h. Thus, $fh/M|_{max}$ is only slightly larger than $fh/M_h|_{max}$ in the canopy during *parallel* periods, but $fh/M|_{max}$ was considerably higher than $fh/M_h|_{max}$ during *perpendicular* periods. Others have predicted and

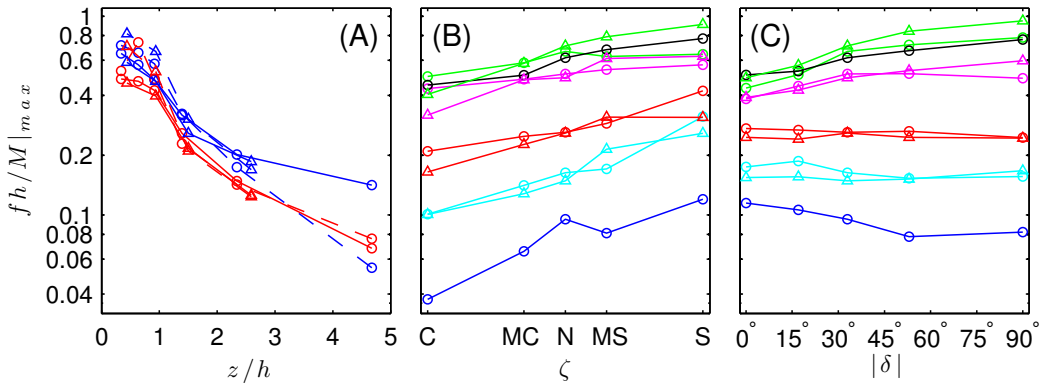

Figure 2.12: Scale of the peak of the premultiplied spectral energy density, $fh/M|_{max}$, as a function of the height z (A), canopy-top stability (B), and $|\delta|$ (C). The data from C13 are depicted as *circles* while data from C11 are depicted as *triangles*. In (A), the line types and colors are identical to that used in Fig. 2.4. The line colors in (B) and (C) are identical to those used in Fig. 2.11. The colors of the four lines for the 2011 data in (B) and (C) were chosen to match the lines for the 2013 data which had the most similar value of z/h. Only data from *row-diagonal* periods are shown in (B) and only N periods are shown in (C).

found that within the CSL, $fh/M_h|_{max}$ = 0.45 ± 0.05 (Kaimal and Finnigan, 1994). The fact that $fh/M|_{max}$ was mathematically identical to $fh/M_h|_{max}$ at $z = h$ allowed us to directly compare our canopy-top values with others. At the anemometer nearest to $z = h$, $fh/M|_{max}$ varied between 0.38 and 0.51 in 2013 and between 0.39 and 0.60 in 2011 over the full range of $|\delta|$ under N conditions. The values determined here were therefore nearly always in the expected range, except perhaps for the *perpendicular* cases wherein the signature of the row spacing likely pushed $fh/M|_{max}$ higher than is typical for a more homogenous canopy.

The premultiplied spectra of $u_\perp$ showed some measurable differences compared to the spectra of the w (Fig. 2.13). During *parallel* periods, the spectra behaved much like that expected for the spanwise wind component in CSL flows (Kaimal and Finnigan, 1994). Specifically, a range of slopes were observed at low frequencies, ranging from a +1 slope for the anemometers in the canopy to much flatter or even negative slopes for the anemometers above the canopy top. During non-neutral periods, this often resulted in dual peaks, separated by nearly two decades, for the anemometers at the canopy top and above (Fig. 2.13A and G). During *perpendicular* periods, when $u_\perp$ was essentially the streamwise component of the wind, the spectra behaved like that expected for the streamwise component of the wind in the CSL and similarly to those reported in Dupont and Patton (2012). Dual peaks in the spectra of $u_\perp$ were also observed during a variety of other direction-stability-height combinations, but were most prevalent at heights just above the canopy during non-neutral periods (e.g., Figs. 2.13B and I) and in the canopy understory during MS periods regardless of δ (e.g., Figs. 2.13G and H). In the understory, the higher-frequency peak was at $fh/M \approx 0.5$, and was thus comparable to the typical values of $fh/M|_{max}$ seen for the w-spectra within the canopy. The lower-frequency peak was typically at $fh/M \approx 0.03$ which is equivalent to a turbulent length scale of $\approx 33h$, or ≈ 70 m. This peak and the lower-frequency peaks in the spectra from the anemometers above the canopy may have been caused by the terrain-induced effects explained in Section 2.2.1, or possibly by the presence of a dirt track between the vineyard blocks ≈ 70 m west of the tower. At the anemometer closest to the canopy top, where $fh/M(z) \approx fh/M_h \approx fz/M(z)$ and our scaling matched those used by others, $fh/M|_{max}$ from the spectra of $u_\perp$ was

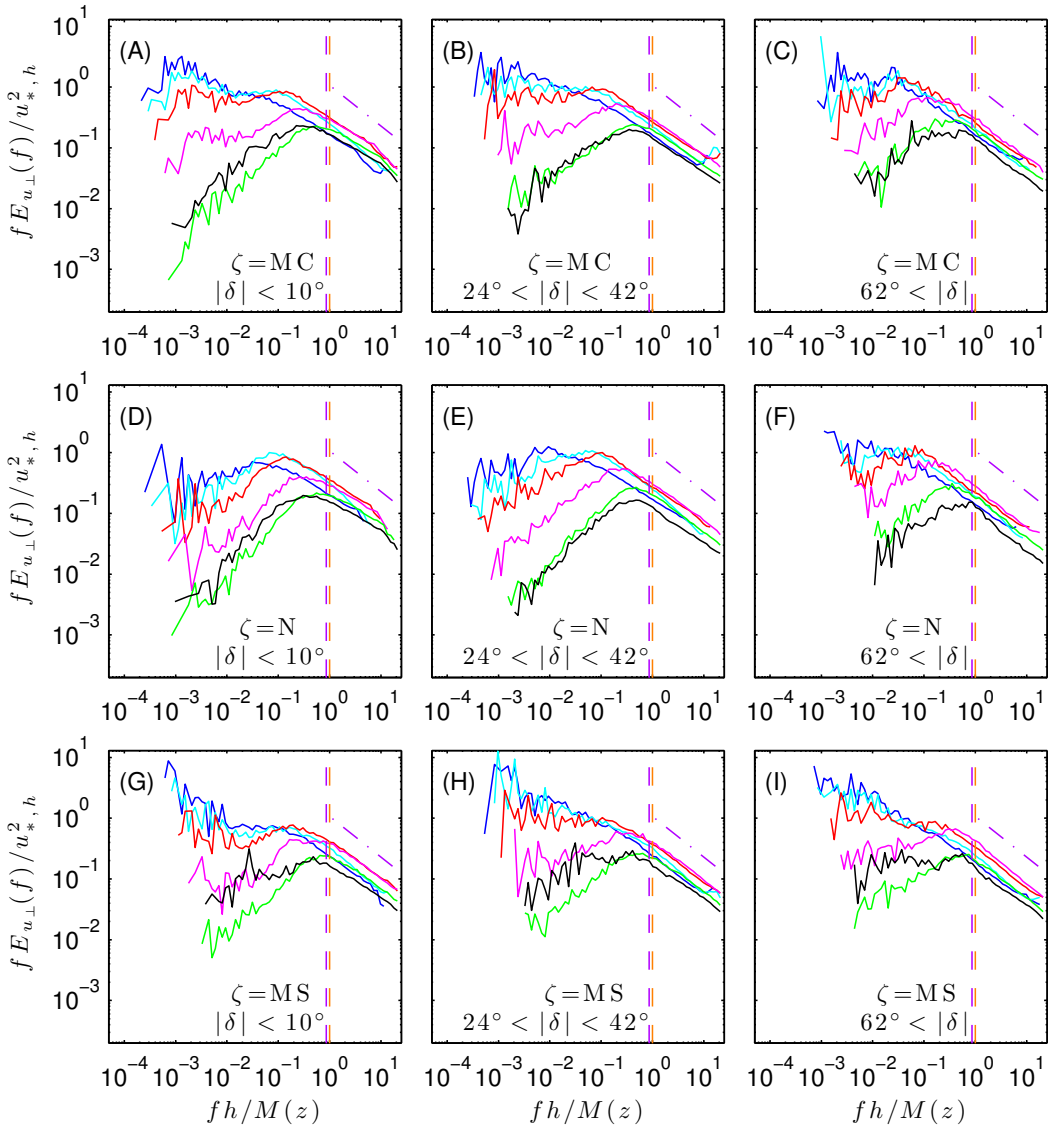

Figure 2.13: Ensemble-averaged premultiplied spectral energy densities of $u_\perp$ for three of the directional and three of the stability classifications. (A), (D), and (G) show *parallel* periods, (B), (E), and (H) show *row-diagonal* periods, and (C), (F), and (I) show *perpendicular* periods. (A), (B), and (C) show MC periods, (D), (E), and (F) show N periods, and (G), (H), and (I) show MS periods. The line styles match those used in Fig. 2.11.

0.30 for *parallel* periods and 0.15 for *perpendicular* periods. Others have shown that the streamwise and spanwise components of the wind typically have values of ≈ 0.15 and between 0.1 and 0.35, respectively (Kaimal and Finnigan, 1994).

The spectra of $v_{\parallel}$ was somewhat similar to that seen for $u_{\perp}$ but with some distinct differences (Fig. 2.14). Again a variety of slopes were observed at low frequencies, but generally, N periods had slightly positive slopes, MC periods had near zero slopes, and MS periods had negative slopes, regardless of δ or height. This is consistent with the slopes reported in Dupont and Patton (2012) for each stability class, respectively. For each height in each directional-stability class, whenever a single value for $fh/M|_{max}$ for the spectra of $v_{\parallel}$ and for the spectra of $u_{\perp}$ could be reasonably determined, the value from the $v_{\parallel}$ spectra was always smaller. This may mean that even when one component was essentially the streamwise component and the other was the spanwise component, the dominant length scale of the row-parallel velocity component was always larger than was the dominant length scale from the row-orthogonal component. Even when the above canopy winds were blowing perpendicular to the vine rows, the streamwise velocity in the CSL was dominated by a smaller turbulent length scale than was the spanwise, row-parallel velocity component. This finding is believed to be directly attributable to the influence of the canopy on the structure of the turbulence in the CSL. This is also similar to the evidence above related to the vorticity thickness and the fact that row-parallel winds typically penetrated more deeply into the canopy than did row-orthogonal winds. Not only was it the case that row-parallel winds penetrated more deeply and had a larger vorticity thickness, the row-parallel component also penetrated more deeply than did the row-orthogonal component even when the winds were not specifically row-parallel. At the anemometer closest to the canopy top, $fh/M|_{max}$ for the $v_{\parallel}$ spectra was 0.13 for *parallel* periods and 0.22 for *perpendicular* periods and therefore nearly equal to what was expected for the streamwise and spanwise components.

To test whether a slope of $-2/3$ was ever truly observed in an ISR of the premultiplied spectral densities, the compensated spectra ($\epsilon^{-2/3}k^{5/3}E_{u_i}(k)$) were analysed (Fig. 2.15). The compensated spectra for all three velocity components for each period were calculated using the dissipation rate values calculated via Equation 2.3. Spectral den-

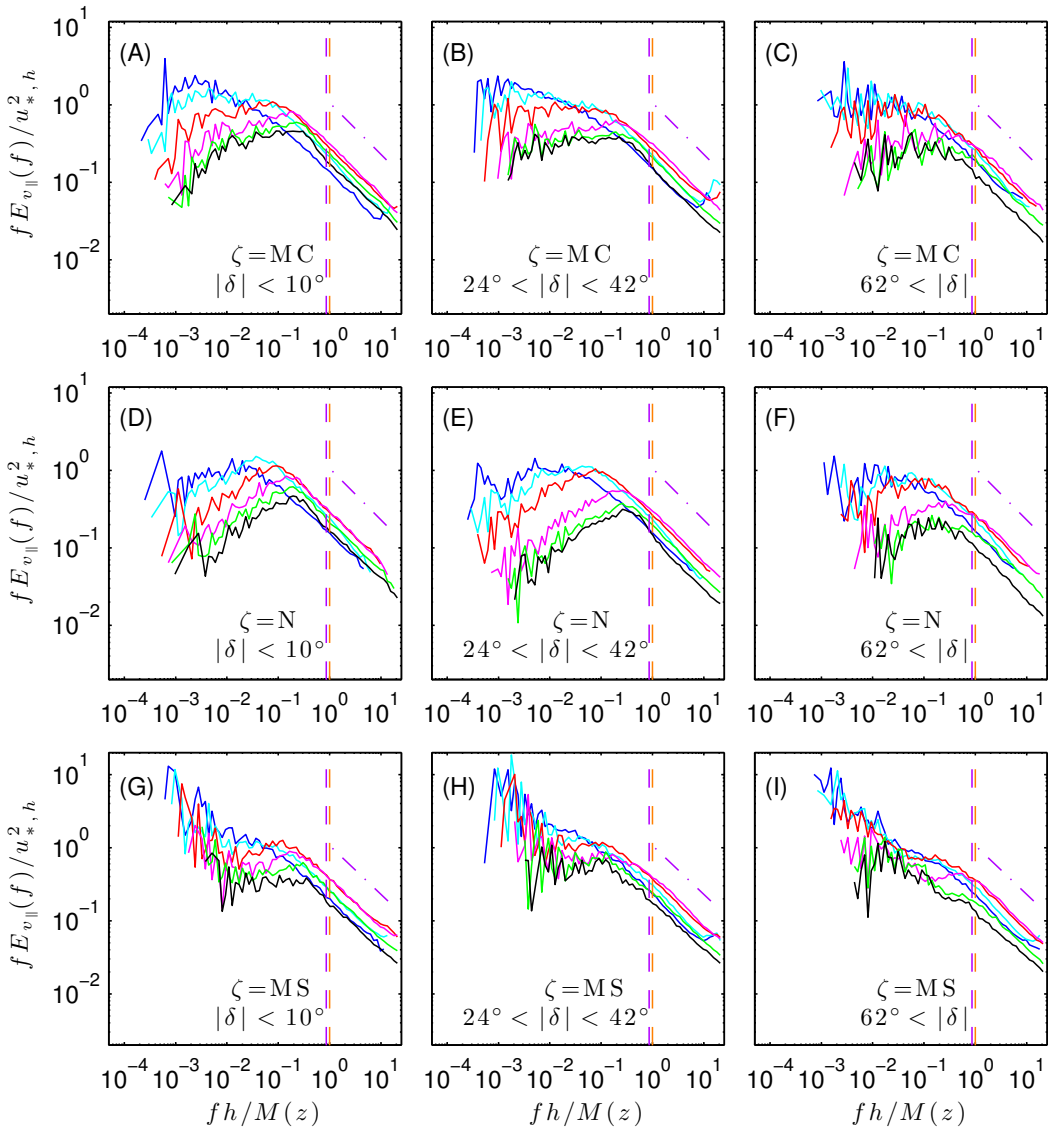

Figure 2.14: Ensemble-averaged premultiplied spectral energy densities of $v_\parallel$ for three of the directional and three of the stability classifications. (A), (D), and (G) show *parallel* periods, (B), (E), and (H) show *row-diagonal* periods, and (C), (F), and (I) show *perpendicular* periods. (A), (B), and (C) show MC periods, (D), (E), and (F) show N periods, and (G), (H), and (I) show MS periods. The line styles match those used in Fig. 2.11.

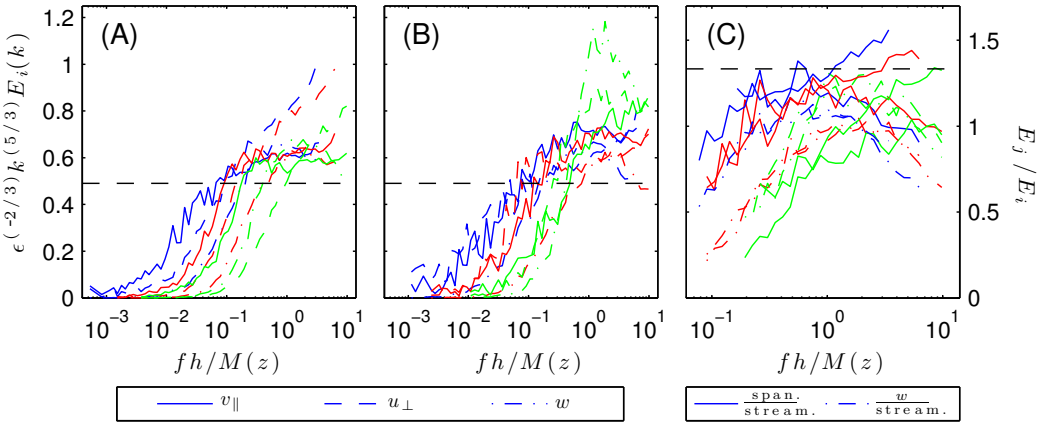

Figure 2.15: The compensated spectral energy densities for all three velocity components shown for *parallel* (A) and *perpendicular* periods (B) under N conditions along with the ratios of the orthogonal velocity components to the streamwise velocity component (C) for each of the pairs depicted in (A) and (B). The line colors match those used in Fig. 2.11. The lower and upper horizontal *dashed* lines in (A) and (B) are at the classical Kolmogorov constants of C_1 and C_1', respectively, while the horizontal *dashed* line in (C) is at $E_{u_j}/E_{u_k} = 4/3$.

sities taken in wavenumber space were used in place of the densities taken in frequency space as used above. This was necessary for proper nondimensionalization and in order to allow for comparisons to the classical Kolmogorov constants of $C_1 = 1.5 \times 18/55$ for the streamwise component and $C_1' = 4/3 \times C_1$ for the spanwise and vertical velocity components (Saddoughi and Veeravalli, 1994). Although compensated spectra from only three heights are shown, they are representative of the behavior seen at all six anemometer heights. In the ISR, the compensated spectra should be independent of wavenumber (or frequency) and the components should collapse to the Kolmogorov constants, regardless of z as long as z is in the surface layer.

For *parallel* periods, $v_\parallel$, which was essentially the streamwise component of the wind, showed over a decade of frequencies for which the compensated spectra were virtually wavenumber independent, regardless of height (Fig. 2.15A). The same behavior was not seen in the spectra of $u_\perp$ or w however. The spectra of $u_\perp$, the spanwise component, never exhibited a flat region and continued to climb throughout the entire range of resolved frequencies. This indicated that in the range of frequencies over which an ISR would typically be observed, the slope in the premultiplied spectra was shallower than the $-2/3$ theory (compare to Fig. 2.13D). A shallower-than-expected slope in the ISR would indicate that some mechanism other than dissipation was also contributing to the energy of $u_\perp$ at frequencies much higher than those associated with h and r_s and that energy was likely being added at many frequencies within the typical ISR range. Unfortunately, the use of sonic anemometry limits our ability to more fully investigate this behavior. Unlike the spectra for both $v_\parallel$ and $u_\perp$, the compensated spectra for w showed neither a flat region nor did it continue to increase over all frequencies. In the range of frequencies for which $\epsilon^{-2/3} k^{5/3} E_{v_\parallel}(k)$ was virtually constant, $\epsilon^{-2/3} k^{5/3} E_w(k)$ showed a continuous change in slope from being quite positive at lower frequencies to being quite negative at the highest resolved frequencies, and only tangentially passed through a slope of zero without maintaining it for any consistent frequency range. In terms of the premultiplied spectra, this would mean that at frequencies over which an isotropic ISR would be expected to exist, there was a continuous change in slope from being more shallow than $-2/3$ to being steeper than $-2/3$ (Fig. 2.11). This behavior is nearly identical to that reported in Dupont

and Patton (2012). The frequency at which the spectral slope was briefly equal to the expected ISR slope was typically approximately one order of magnitude higher than $fh/M|_{max}$, suggesting that perhaps at scales of $h/10$, local isotropy in w was realized.

The components of the compensated spectra taken during *perpendicular* periods were very similar to those observed during *parallel* periods except that the spectra of $u_\perp$ (the streamwise component) exhibited a wavenumber-independent ISR while the spectra of $v_\parallel$ (the spanwise component) showed a continuous increase over all f (Fig. 2.15B).

The fact that the ISRs in the compensated spectra collapsed across anemometers of different heights was evidence that the dissipation profiles in Fig. 2.10 had the correct shape. Unfortunately, the fact that the streamwise spectra typically collapsed to a value closer to C_1' than to C_1, along with the fact that the spanwise and vertical components never showed a consistent ISR as predicted by Kolmogorov's theory, is evidence that components of the $\langle \overline{e} \rangle$ budget other than shear production and ϵ may have still been active in the scale range where the ISR would have been expected (Perry et al., 1986). It may have also been that we were unable to determine accurate values of ϵ, perhaps due to the shortcomings of the use of Taylor's frozen turbulence hypothesis. More highly resolved instruments, that were capable of resolving dissipation scales and producing consistent $-2/3$ slopes in the ISRs, would have been necessary in order to produce more accurate values of ϵ (Nelson et al., 2007).

Regardless of the lack of a consistent observable ISR in the vertical or spanwise velocity spectra, the ratios of those spectra to the spectra of the streamwise component were calculated and are represented by E_{u_j}/E_{u_k}, where u_j indexes over the spanwise component and w while u_k is the streamwise component that is appropriate for the respective directional classes. Within the range of frequencies over which an ISR was observed in the streamwise velocity component, this ratio typically had values of ≈ 1.0. E_{u_j}/E_{u_k} tended to decrease with decreasing z, with the anemometer at $z = 10.1$ m showing average ratios closer to the expected isotropic value of 4/3 than did the anemometer at $z = 1.4$ m which had ratios < 1.0 at some frequencies. In CSLs, it is

not uncommon for E_{u_j}/E_{u_k} to diverge from the 4/3 typically seen in surface layers and the values determined here were very similar to those seen in a variety of other canopies, specifically 1.1 ± 0.15 (e.g., Brunet et al., 1994; Christen et al., 2009).

2.4 Conclusions

The trellised vineyard architecture had a significant effect on the flow field in the CSL. The discrete two-dimensional nature of the canopy led to turning of the velocity profile and biased the flow direction in the canopy toward being row-parallel regardless of the above canopy wind direction. Standard CSL flow statistics tended to vary as a function of how far from row-parallel that wind direction was. Row-parallel winds were significantly different from row-orthogonal winds and these differences were linked to the projected frontal area seen by the wind or to a nonisotropic drag created by the vine and leaf orientations. Regardless of the cause, asymmetric variations in variables including skewness profiles, stress tensor components, and ejection-to-sweep ratios were observed as functions of $|\delta|$. The behavior of these variables is an indication that turbulent flow structures may also change with δ, a hypothesis that would be very difficult to test in the vineyard and would likely require wind-tunnel experiments or Large-Eddy Simulation. Additionally, as $|\delta|$ increased, the standard log-law velocity profile was displaced upwards but the height of the inflection point in the velocity profile was reduced. This resulted in a steeper gradient in the velocity profile at the canopy top and thus led to a decrease in L_s over the same range. Because of the tie between L_s and the vorticity thickness in the canopy mixing-layer analogy, it could be said that the vorticity thickness also decreased. This was substantiated in the behavior of the production terms of the turbulent kinetic energy budget which generally showed that as $|\delta|$ increased, production increased at the canopy top and decreased both above the canopy and in the lower canopy. The canopy mixing-layer analogy would also suggest that the average streamwise spacing between coherent structures may have decreased with $|\delta|$, but because L_s was always $> 0.5h$, Λ may have stayed relatively constant at $\approx 5h$. A change in the size of the coherent structures in the CSL as a function of $|\delta|$ was supported by the variation in $fh/M|_{max}$. It appeared to show that as $|\delta|$ increased, the turbulent

length scale of the spectral peak at the anemometers within the canopy trended from being approximately twice the canopy height during *parallel* periods to being very near to r_s and h during *perpendicular* periods. The spectral energy densities of the three velocity components also demonstrated that despite an inertial subrange being present for the streamwise component, none developed for the spanwise component, even at the uppermost anemometer. For the vertical velocity component, the slope of the spectra in the same range of frequencies over which the ISR was observed in the streamwise component tended to continuously get steeper with increasing frequency but was never consistent with ISR theory for any significant range of frequencies. Better instruments for measuring spectra within canopies would be recommended if higher resolution of the ISR and dissipation ranges is necessary. Collectively, this information gives considerable insight into the complex impacts that the vineyard canopy has on the flow of the CSL.

2.5 Acknowledgments

This work was funded by the United States Department of Agriculture (USDA) project 5358-22000-039-00D, the National Science Foundation grant AGS 1255662, and the University of Utah's Global Change and Sustainability Center. The use trade, firm, or corporation names in this publication are for information and convenience of the reader. Such use does not constitute an endorsement or approval by the USDA or the Agriculture Research Service of any product or service to the exclusion of others that may be suitable. We also thank the staff of the USDA-ARS labs in Corvallis, Oregon for their considerable time, effort, and assistance in running the field campaigns.

2.6 Appendix 1: Derivation of Turbulent Kinetic Energy Budget

Following Raupach and Shaw (1982), the budget of $\overline{e}$ in a canopy can be written as,

$$\frac{D\langle\overline{e}\rangle}{Dt} = \frac{\partial\langle\overline{e}\rangle}{\partial t} + \underbrace{\langle\overline{u_i}\rangle\frac{\partial\langle\overline{e}\rangle}{\partial x_i}}_{\text{Advec.}} = \underbrace{-\langle\overline{u_i'u_j'}\rangle\frac{\partial\langle\overline{u_i}\rangle}{\partial x_j}}_{\text{Shear}} \underbrace{-0.5\frac{\partial\langle\overline{u_i'u_j'u_j'}\rangle}{\partial x_i}}_{\text{Turb.}}$$
$$\underbrace{-0.5\frac{\partial\langle\overline{u_i'u_i'}''\overline{u_j}''\rangle}{\partial x_j}}_{\text{Disp.}} \underbrace{-\langle\overline{u_i'u_j'}''\frac{\partial\overline{u_i}}{\partial x_j}\rangle}_{\text{Wake}} + \underbrace{g\frac{\overline{w'T'}}{\overline{T}}}_{\text{Buoy.}} - \epsilon - \mathcal{R}1, \tag{2.4}$$

where primes represent deviations from temporal averages which are represented as overbars, double primes represent deviations from spacial averages (taken over volumes of very small Δz with Δx and Δy each larger than the local scales of the canopy architecture) represented by angled brackets, g is the acceleration due to gravity, ϵ is the dissipation rate of $\langle\overline{e}\rangle$ due to work being done against the viscosity, $\mathcal{R}1$ is the budget residual, which here represents the pressure transport term which cannot usually be explicitly calculated, and index notation ($u_i = \{u_\perp, v_\parallel, w\}$ and $x_i = \{x_\perp, y_\parallel, z\}$ for this coordinate system) is used for simplicity (Brunet et al., 1994; Kaimal and Finnigan, 1994). The labeled terms represent mean advection of $\langle\overline{e}\rangle$ into the averaging volume, shear production, turbulent transport, dispersive transport, wake production, and buoyancy production of $\langle\overline{e}\rangle$ inside the averaging volume, respectively.

The budget equation can be considerably simplified through standard assumptions used for canopy flows and sonic anemometers. However, due to the coordinate system used here and the discrete nature of the vine architecture, some terms that are often neglected in other studies, like those performed on streamwise aligned coordinates in homogeneous canopies, had to be retained. Additionally, although Taylor's hypothesis would suggest that our anemometer signal could be interpreted as a spatial signal, such a dubious approach is ill-advised in a canopy and assuredly should not be assumed to accurately represent the heterogeneity of the vineyard. We can, however, assume that the temporal average taken from the anemometer data also approximates the spatial average as has been done in many previous studies (e.g., Meyers and Baldocchi, 1991), thus making use of the temporally-spatially averaged budget appropriate. If instead the budget of $\overline{e}$ could be investigated at multiple spatial locations within the vineyard canopy, simply using a temporally averaged version may

be more useful in understanding transport, especially near the vine "faces."

First, out of lack of interest for temporal variations at timescales larger than 30-minutes and because only quasi-steady 30-minute periods of data were used, the unsteady term was set to zero.

Through the index notation, the advection term is the summation of three individual components, all of which are zero by definition. Although $\partial\overline{e}/\partial x_\perp$ may be non-zero locally within the wakes of individual vines, when spatial averaging is used, such spatial variations disappear from the advection term and are instead accounted for in the dispersive transport term. The spatial averaging causes $\langle\overline{e}\rangle$ to be a constant within the averaging volume and thus $\partial\langle\overline{e}\rangle/\partial x_\perp = \partial\langle\overline{e}\rangle/\partial y_\parallel = 0$. This same rule can be applied to any term wherein the slope of a spatially averaged variable is to be determined in either the $x_\perp$ or $y_\parallel$ direction. By definition, a planar-averaged variable has no slope along any axis on the plane. Likewise, although $\overline{w}$ may be persistently non-zero at some points within the canopy, $\langle\overline{w}\rangle$ must be zero (assuming an accurate tilt correction and neglecting subsidence at spatial scales larger than that used for $\langle\rangle$). We therefore assumed that the anemometers were placed within the aisle in such a way that no persistent features in w caused $\overline{w}$ to not equal $\langle\overline{w}\rangle$.

The shear production term is the summation of nine individual terms each including a component of the stress tensor. The six terms containing $\partial\langle\rangle/\partial y_\parallel$ and $\partial\langle\rangle/\partial x_\perp$ are zero by definition as described above. Additionally, any term containing $\partial/\partial y_\parallel$ can be said to be zero due to the continuity of the canopy in the row-parallel direction. The two remaining terms which contain $\partial\langle\overline{w}\rangle/\partial x_i$ are zero due to the spatial averaging of $\overline{w}$ but would likely be of interest when using only local ensemble averaging of spatially resolved data. This leaves only the two terms which contain the components of the vertical momentum flux paired with the vertical gradients of their respective velocity components, i.e., $\langle\overline{u'_\perp w'}\rangle\partial\langle\overline{u_\perp}\rangle/\partial z + \langle\overline{v'_\parallel w'}\rangle\partial\langle\overline{v_\parallel}\rangle/\partial z$.

The turbulent transport term can also be expanded into nine components, six of which have either $\partial\langle\rangle/\partial x_\perp$ or $\partial\langle\rangle/\partial y_\parallel$ and are therefore zero. This leaves only the three terms with $\partial/\partial z$. Based on the observed behavior of the cross-vine momentum flux in Section 2.3 and the discontinuity of the canopy in the row-perpendicular direction, it is likely that terms like $\partial(\overline{u'_\perp v'^2_\parallel})/\partial x_\perp$ would be of some significance in a local budget

of e even if such cannot be resolved with this approach and data.

The dispersive transport term in Equation 2.4 appears due to the spatial averaging procedures performed on the advection term in the temporally averaged budget of e. Again, six of the nine components of the dispersive transport term are zero because they contain $\partial\langle\rangle/\partial x_\perp$ or $\partial\langle\rangle/\partial y_\parallel$. The final three terms are $\partial/\partial z[\langle\overline{u_\perp'^2}''\overline{w}''\rangle + \langle\overline{v_\parallel'^2}''\overline{w}''\rangle + \langle\overline{w'^2}''\overline{w}''\rangle]$. Because it was assumed that the data from the anemometers accurately represent a spatial average and deviations in the data can only be treated as temporal deviations, we are unable to resolve any terms that contain dispersive components that arise from the spatial decomposition of the temporally averaged budget equation. Fortunately, the sum of these three terms should be small compared to the other terms of the budget and will be accounted for in a budget residual, $\mathcal{R}2$. Böhm et al. (2013) showed that the dispersive transport term was only non-zero in a small portion of the upper canopy and never had a magnitude greater than $\approx 25\%$ of the wake production term at those heights.

The wake production term only exists within Equation 2.4 as a byproduct of the spatial averaging procedures performed on the shear production term. It is within the wake production term that the energy associated with spatial gradients at scales smaller than the averaging scale of $\langle\rangle$ is accounted for. Following the work of Raupach and Shaw (1982), many other studies (e.g., Brunet et al., 1994; Raupach et al., 1996; Böhm et al., 2013) have used $\langle\overline{u_i}\rangle\partial/\partial x_j\left[\langle\overline{u_i'u_j'}\rangle + \langle\overline{u_i}''\overline{u_j}''\rangle\right]$ as an equivalent for the wake production term. This approach can then be expanded into 18 individual terms. All but four of those terms are zero for the same reasons discussed above, i.e., $\langle\overline{w}\rangle = \partial\langle\rangle/\partial y_\parallel = \partial\langle\rangle/\partial x_\perp = 0$. Of the remaining four terms, two contain the dispersive form of the Reynolds stress based on $u_\perp$ and $v_\parallel$ and they cannot be determined with the anemometer data because of our inability to approximate both temporal and spatial deviations. For this reason, the two terms containing the dispersive form of the Reynolds stress have to be neglected and will also appear in $\mathcal{R}2$. Fortunately, Bailey and Stoll (2013) showed that $\overline{u_\perp}''\overline{w}''$ was never more than $\approx 20\%$ of the total vertical flux in a vineyard-like canopy under *perpendicular* conditions and was only non-zero in a small span of heights just below the mid-canopy. Poggi et al. (2004) also showed that the ratio of $\overline{u_\perp}''\overline{w}''/\overline{u_\perp'w'}$ varies as a function of canopy density and that for even

the most extreme canopy case, the ratio never exceeded $\approx 40\%$.

All of these assumptions and simplifications reduced the full budget of e (Equation 2.4) to the version shown as Equation 2.2, all of the terms of which could be solved for with the anemometer data in the vineyard. The two residual terms as defined here were simply combined into one term $\mathcal{R}$ because the contributions can not be individually partitioned. It is important to understand, however, that some portion of the residual arose from a physical process (pressure transport) that is difficult to collect while some other portion is attributed to spatial variations which cannot be explicitly solved for with a single tower of anemometers.

2.7 References

Addepalli, B. and E. R. Pardyjak, 2013: Investigation of the flow structure in step-up street canyons - mean flow and turbulence statistics. *Boundary-Layer Meteorol.*, **148**, 133–155.

Aubinet, M., et al., 2005: Comparing CO_2 storage and advection conditions at night at different carboeuroflux sites. *Boundary-Layer Meteorol.*, **116**, 63–94.

Aylor, D. E. and F. J. Ferrandino, 1989: Dispersion of spores released from an elevated line source within a wheat canopy. *Boundary-Layer Meteorol.*, **46**, 251–273.

Bailey, B. N., M. Overby, P. Willemsen, E. R. Pardyjak, W. F. Mahaffee, and R. Stoll, 2014a: A scalable plant-resolving radiative transfer model based on optimized gpu ray tracing. *Agric. For. Meteorol.*, **198–199**, 192–208.

Bailey, B. N. and R. Stoll, 2013: Turbulence in sparse, organized vegetative canopies: A large-eddy simulation study. *Boundary-Layer Meteorol.*, **147**, 369–400.

Bailey, B. N. and R. Stoll, 2016: The creation and evolution of coherent structures in plant canopy flows and their role in turbulent transport. *J. Fluid Mech.*, **789**, 425–460.

Bailey, B. N., R. Stoll, E. R. Pardyjak, and W. F. Mahaffee, 2014b: Effect of vegetative canopy architecture on vertical transport of massless particles. *Atmos. Environ.*, **95**, 480–489.

Belcher, S. E., 2005: Mixing and transport in urban areas. *Phil. Trans. R. Soc. A*, **363**, 2947–2968.

Belcher, S. E., I. N. Harman, and J. J. Finnigan, 2012: The wind in the willows: Flows in forest canopies in complex terrain. *Annu. Rev. Fluid Mech.*, **44**, 479–504.

Böhm, M., J. J. Finnigan, M. R. Raupach, and D. Hughes, 2013: Turbulence structure within and above a canopy of bluff elements. *Boundary-Layer Meteorol.*, **146**, 393–419.

Boudreault, L., S. Dupont, A. Bechmann, and E. Dellwik, 2016: How forest inhomogeneities affect the edge flow. *Boundary-Layer Meteorol.*, doi 10.1007/s10546-016-0202-5.

Brunet, Y., J. J. Finnigan, and M. R. Raupach, 1994: A wind tunnel study of air flow in waving wheat: single-point velocity statistics. *Boundary-Layer Meteorol.*, **70**, 95–132.

Chahine, A., S. Dupont, C. Sinfort, and Y. Brunet, 2014: Wind-flow dynamics over a vineyard. *Boundary-Layer Meteorol.*, **151**, 557–577.

Christen, A., M. W. Rotach, and R. Vogt, 2009: The budget of turbulent kinetic energy in the urban roughness sublayer. *Boundary-Layer Meteorol.*, **131**, 193–222.

Deardorff, J. W., 1970: A numerical study of three-dimensional turbulent channel flow at large Reynolds numbers. *J. Fluid Mech.*, **41**, 453–480.

Dupont, S. and Y. Brunet, 2008: Influence of foliar density profile on canopy flow: A large-eddy simulation study. *Agric. For. Meteorol.*, **148**, 976–990.

Dupont, S. and E. G. Patton, 2012: Influence of stability and seasonal canopy changes on micrometeorology within and above an orchard canopy: The CHATS experiment. *Agric. For. Meteorol.*, **157**, 11–29.

Finnigan, J. J., 2000: Turbulence in plant canopies. *Ann. Rev. Fluid Mech.*, **32**, 519–571.

Grachev, A. A., E. L. Andreas, C. W. Fairall, P. S. Guest, and P. O. Persson, 2013: The critical richardson number and limits of applicability of local similarity theory in the stable boundary layer. *Boundary-Layer Meteorol.*, **147**, 51–82.

Hanna, S. R. and E. Baja, 2009: A simple urban dispersion model tested with tracer data from Oklahoma City and Manhattan. *Atmos. Environ.*, **43**, 778–786.

Harman, I. N., M. Böhm, J. J. Finnigan, and D. Hughes, 2016: Spatial variability of the flow and turbulence within a model canopy. *Boundary-Layer Meteorol.*, **160**, 375–396.

Hoydysh, W. G. and W. F. Dabberdt, 1994: Concentration fields at urban intersections: Fluid modeling studies. *Atmos. Environ.*, **28**, 1849–1860.

Huang, J., M. Cassiani, and J. D. Albertson, 2009: The effects of vegetation density on coherent turbulent structures within the canopy sublayer: A large-eddy simulation study. *Boundary-Layer Meteorol.*, **133**, 253–275.

Huq, P. and P. Franzese, 2013: Measurements of turbulence and dispersion in three idealized urban canopies with different aspect ratios and comparisons with a gaussian plume model. *Boundary-Layer Meteorol.*, **147**, 103–121.

Jackson, P. S., 1981: On the displacement height in the logarithmic velocity profile. *J. Fluid Mech.*, **111**, 15–25.

Judd, M. J., M. R. Raupach, and J. J. Finnigan, 1996: A wind tunnel study of turbulent flow around single and multiple windbreaks, Part 1: Velocity fields. *Boundary-Layer Meteorol.*, **80**, 127–165.

Kaimal, J. C. and J. J. Finnigan, 1994: *Atmospheric Boundary Layer Flows: Their Structure and Measurement*. Oxford University Press.

Klein, P., B. Leitl, and M. Schatzmann, 2007: Driving physical mechanisms of flow and dispersion in urban canopies. *Int. J. Climatol.*, **27**, 1887–1908.

Launiainen, S., et al., 2007: Vertical variability and effect of stability on turbulence characteristics down to the floor of a pine forest. *Tellus*, **59B**, 919–936.

Legg, B. J. and I. F. Long, 1975: Turbulent diffusion within a wheat canopy: II. Results and interpretation. *Quart. J. Roy. Meteorol. Soc.*, **101**, 611–628.

Lu, S. S. and W. W. Willmarth, 1973: Measurements of the structure of Reynolds stress in a turbulent boundary layer. *J. Fluid Mech.*, **60**, 481–511.

Mabrouk, H., A. Carbonneau, and H. Sinquet, 1997: Canopy structure and radiation regime in grapevine. I. Spatial and angular distribution of leaf area in two canopy systems. *Vitis*, **36**, 119–123.

Mahaffee, W., S. Schwebs, F. Hand, D. Gubler, B. Bailey, and R. Stoll, 2014: Improving management of grape powdery mildew with new tools and knowledge. *Practical Winery & Vineyard*, **April**, 59–67.

Mahaffee, W. F. and R. Stoll, 2016: The ebb and flow of airborne pathogens: Monitoring and use in disease management decisions. *Phytopath.*, **106**, 420–431.

Mahrt, L., 1998: Stratified atmospheric boundary layers and breakdown of models. *Theoret. Comput. Fluid Dynamics*, **11**, 263–279.

Massman, W. J., 1997: An analytical one-dimensional model of momentum transfer by vegetation of arbitrary structure. *Boundary-Layer Meteorol.*, **83**, 407–421.

Maurer, K. D., G. Bohrer, W. T. Kenny, and V. Y. Ivanov, 2015: Large-eddy simulations of surface roughness parameter sensitivity to canopy-structure characteristics. *Biogeosciences*, **12**, 2533–2548.

Meyers, T. P. and D. Baldocchi, 1991: The budgets of turbulent kinetic energy and Reynolds stress within and above a deciduous forest. *Agric. For. Meteorol.*, **53**, 207–222.

Miller, N. E., R. Stoll, W. Mahaffee, T. M. Neill, and E. Pardyjak, 2015: An experimental study of momentum and heavy particle transport in a trellised agricultural canopy. *Agric. For. Meteorol.*, **211–212**, 100–114.

Monin, A. S. and A. M. Yaglom, 1975: *Statistical Fluid Mechanics: Mechanics of Turbulence*, Vol. 2. The MIT Press, Cambridge, Mass.

Nelson, M. A., E. R. Padyjak, M. J. Brown, and J. C. Klewicki, 2007: Properties of the wind field within the Oklahoma City Park Avenue street canyon. Part II: Spectra, cospectra, and quadrant analyses. *J. Appl. Meteorol. Climatol.*, **46**, 2055–2073.

Nelson, M. A., E. R. Padyjak, and P. Klein, 2011: Momentum and turbulent kinetic energy budgets within the park avenue street canyon during the Joint Urban 2003 field campaign. *Boundary-Layer Meteorol.*, **140**, 143–162.

Pan, Y., M. Chamecki, and S. A. Isard, 2014: Large-eddy simulation of turbulence and particle dispersion inside the canopy roughness sublayer. *J. Fluid Mech.*, **753**, 499–534.

Parlange, M. and B. Wilfried, 1989: Regional roughness of the Landes forest and surface shear stress under neutral conditions. *Boundary-Layer Meteorol.*, **48**, 69–81.

Perry, A. E., S. M. Henbest, and M. S. Chong, 1986: A theoretical and experimental study of wall turbulence. *J. Fluid Mech.*, **165**, 163–199.

Poggi, D., G. G. Katul, and J. D. Albertson, 2004: A note on the contribution of dispersive fluxes to momentum transfer within canopies. *Boundary-Layer Meteorol.*, **111**, 615–621.

Pope, S., 2000: *Turbulent Flows*. Cambridge University Press, U. K., 771 pp.

Raupach, M. R., J. J. Finnigan, and Y. Brunet, 1996: Coherent eddies and turbulence in vegetation canopies: The mixing-layer analogy. *Boundary-Layer Meteorol.*, **78**, 351–382.

Raupach, M. R. and R. H. Shaw, 1982: Averaging procedures for flow within vegetation canopies. *Boundary-Layer Meteorol.*, **22**, 79–90.

Robinson, S. K., 1991: Coherent motions in the turbulent boundary layer. *Ann. Rev. Fluid Mech.*, **23**, 601–639.

Saddoughi, S. G. and S. V. Veeravalli, 1994: Local isotropy in turbulent boundary layers at high Reynolds number. *J. Fluid Mech.*, **268**, 333–372.

Santiago, J. L., O. Coceal, and A. Martilli, 2013: How to parameterize urban-canopy drag to reproduce wind-direction effects within the canopy. *Boundary-Layer Meteorol.*, **149**, 43–63.

Schuepp, P. H., 1993: Tansley Review No. 59 Leaf boundary layers. *New Phytol.*, **125**, 477–507.

Shimizu, T., 2015: Effect of coordinate rotation systems on calculated fluxes over a forest in complex terrain: A comprehensive comparison. *Boundary-Layer Meteorol.*, **156**, 277–301.

Sogachev, A. and M. Kelly, 2016: On displacement height, from classical to practical formulation: Stress, turbulent transport and vorticity considerations. *Boundary-Layer Meteorol.*, **158**, 361–381.

Sorbjan, Z., 2010: Gradient-based scales and similarity laws in the stable boundary layer. *Quart. J. Roy. Meteorol. Soc.*, **136**, 1243–1254.

Stull, R. B., 1988: *An Introduction to Boundary Layer Meteorology*. Kluwer Academic Publishers, Dordrecht, 670 pp.

Su, H.-B., H. P. Schmid, C. S. D. Grimmond, C. S. Vogel, and A. J. Oliphant, 2004: Spectral characteristics and correction of long-term eddy-covariance measurements over two mixed hardwood forests in non-flat terrain. *Boundary-Layer Meteorol.*, **110**, 213–253.

Su, H.-B., H. P. Schmid, C. S. Vogel, and P. S. Curtis, 2008: Effects of canopy morphology and thermal stability on mean flow and turbulence statistics observed inside a mixed hardwood forest. *Agric. For. Meteorol.*, **148**, 862–882.

Su, H.-B., R. H. Shaw, K. T. Paw U, C.-H. Moeng, and P. P. Sullivan, 1998: Turbulent statistics of neutrally stratified flow within and above a sparse forest from large-eddy simulation and field observations. *Boundary-Layer Meteorol.*, **88**, 363–397.

Talaie, A., M. Shojaie-Saadee, A. Dadashpour, and M. A. Asgari-Sarcheshmeh, 2011: Fruit quality in five apple cultivars trees trained to intensive training system: Geneva y-trellis. *GENETIKA*, **43**, 153–161.

Thiessen, L. D., J. A. Keune, T. M. Neill, W. W. Turechek, G. G. Grove, and W. F. Mahaffee, 2016: Development of a grower-conducted inoculum detection assay for management of grape powdery mildew. *Plant Pathology*, **65**, 238–249.

Thomas, C. and T. Foken, 2007: Flux contribution of coherent structures and its implications for the exchange of energy and matter in a tall spruce canopy. *Boundary-Layer Meteorol.*, **123**, 317–337.

Vickers, D. and L. Mahrt, 2006: Contrasting mean vertical motion from tilt correction methods and mass continuity. *Agric. For. Meteorol.*, **138**, 93–103.

Wilson, J. D., D. P. Ward, G. W. Thurtell, and G. E. Kidd, 1982: Statistics of atmospheric turbulence within and above a corn canopy. *Boundary-Layer Meteorol.*, **24**, 495–519.

Yang, B., A. P. Morse, R. H. Shaw, and K. T. Paw U, 2006: Large-eddy simulation of turbulent flow across a forest edge. Part II: Momentum and turbulent kinetic energy budgets. *Boundary-Layer Meteorol.*, **121**, 433–457.

Yue, W., C. Meneveau, M. B. Parlange, W. Zhu, H. S. Kang, and J. Katz, 2008: Turbulent kinetic energy budgets in a model canopy: Comparisons between LES and wind-tunnel experiments. *Environ. Fluid Mech.*, **8**, 73–95.

CHAPTER 3

AN EXPERIMENTAL STUDY OF MOMENTUM AND HEAVY PARTICLE TRANSPORT IN A TRELLISED AGRICULTURAL CANOPY

Agricultural and Forest Meteorology 211–212 (2015) 100–114

Contents lists available at ScienceDirect

Agricultural and Forest Meteorology

journal homepage: www.elsevier.com/locate/agrformet

An experimental study of momentum and heavy particle transport in a trellised agricultural canopy

Nathan E. Miller[a], Rob Stoll[a,*], Walter F. Mahaffee[b], Tara M. Neill[b], Eric R. Pardyjak[a]

[a] Department of Mechanical Engineering, University of Utah, Salt Lake City, UT, United States
[b] USDA Agricultural Research Service, Horticulture Crops Research Unit, Corvallis, OR, United States

ARTICLE INFO

Article history:
Received 25 April 2014
Received in revised form 15 May 2015
Accepted 1 June 2015

Keywords:
Canopy flow
Dispersion
Particle transport
Vineyard experiments

ABSTRACT

Turbulent particle dispersion in plant canopies plays an important role in many agricultural and forestry ecosystems. Most research on dispersion in plant canopies has focused on dispersal patterns in homogeneous dense canopies and/or on patterns far from the source. To study near-source particle dispersion in a sparse agricultural canopy, a series of point-source particle release events was conducted in a commercial vineyard. Analysis of the wind velocity data indicated that the majority of the flow in the open spaces between the vine rows was channeled parallel to the vine rows regardless of the direction of the mean wind above the canopy. Although this channeling led to significant turning of the mean velocity, profiles of turbulent statistics taken at times when the above-canopy winds were nearly parallel to the vine rows showed similar behavior to canopy flow profiles in previous studies. The particle release events were conducted using fluorescent microspheres with similar physical characteristics to the spores of multiple airborne fungal pathogens of grapes (diameter = 10–45 μm, density = 1.0 g/cm^3). Microspheres were released from two vertical positions within the canopy and monitored using a dense three dimensional impaction trap array in the near-source region (1–5 canopy heights downwind). The shape of the microsphere plumes was strongly impacted by the flow channeling within the canopy. Specifically, the plumes' maximum concentrations were typically channelled down the aisle in which they originated. The spanwise concentration profile also tended to be skewed from the release aisle toward the mean wind direction above the canopy. This was believed to be caused by the wind directional shear created by the difference between the mean wind direction above the canopy and the vine row direction as well as the filtering effects of the plants themselves.

1. Introduction

Turbulent dispersion in a plant canopy differs from dispersion in the free atmospheric boundary layer (ABL) because of the interplay between the canopy architecture and the local meteorological conditions. Within plant canopies, enhanced turbulent intermittency (Finnigan, 2000) can drastically alter dispersion gradients (Ferrandino, 1993). In addition, the canopy's plant density has a direct impact on the canopy-atmosphere interaction and the characteristics of dispersion (Bailey et al., 2014).

Most previous studies of momentum transport and particle dispersion in plant canopies have focused on dense canopies (e.g., Aylor and Ferrandino, 1989; Dwyer et al., 1997; Finnigan, 2000; Thomas and Foken, 2007; Yue et al., 2007; Su et al., 1998) or on forest clearings and edge flows (e.g., Yang et al., 2006; Dupont and Brunet, 2008; Detto et al., 2008; Cassiani et al., 2008). Significantly fewer experimental (e.g., Weiss and Allen, 1976; Verhoef et al., 1997; Novak et al., 2000; Böhm et al., 2013) and numerical (e.g., Su et al., 2008; Huang et al., 2009; Bailey and Stoll, 2013; Bailey et al., 2014) studies have focused on sparse canopies where the canopy had discontinuities at length scales on the order of the canopy height. These few primarily focused on momentum transport with the experimental studies often using wind tunnel or water channel canopy models with a single type of canopy architecture (e.g., arrays of cylinders, see: Raupach et al., 1980; Judd et al., 1996; Novak et al., 2000; Poggi et al., 2004; Böhm et al., 2013). One exception to this is the experiment of Patton et al. (2011) which reported measurements of momentum transport in a sparse walnut orchard. In the numerical studies, the analysis typically treated the canopy as horizontally homogenous (e.g., Dupont and Brunet, 2008; Huang et al., 2009).

* Corresponding author. Tel.: +1 8015813405.
E-mail addresses: nmiller@eng.utah.edu (N.E. Miller), rstoll@eng.utah.edu (R. Stoll), tara.neill@ars.usda.gov (T.M. Neill), pardyjak@eng.utah.edu (E.R. Pardyjak).

http://dx.doi.org/10.1016/j.agrformet.2015.06.003
0168-1923/

The majority of the experimental field studies that have examined particle transport in plant canopies have been performed in dense canopies (e.g., Raynor et al., 1974; Aylor and Ferrandino, 1989; Gleicher et al., 2014). In addition to a focus on dense canopies, the information about particle plume spread dynamics has often been limited by low particle sampling densities that are only along a single arc or plane. The studies have used their data for applications including the validation of Lagrangian particle models (Aylor et al., 2001), average canopy vertical particle flux modeling (Chamecki et al., 2012), and maximum concentration tracking (Hanna and Baja, 2009). A few studies have used three-dimensional sampling arrays but have focused on more qualitative spread evaluation (Raynor et al., 1974) or on model validation and not specifically on the three-dimensional plume shape (Gleicher et al., 2014). These studies were also performed in dense canopies and did not use dense enough arrays to characterize the plume shape in the near-source region. None of these studies examined both momentum and particle transport in a sparse plant canopy.

Exceptions to the focus on dense canopies include Novak et al. (2000) and Poggi et al. (2004) which investigated the effect of canopy density on momentum transport. These studies did not investigate the density effects on particle transport and were still performed on relatively homogenous canopies. Considerably fewer studies have focused on sparse non-homogenous canopies (e.g., Weiss and Allen, 1976; Bailey and Stoll, 2013; Bailey et al., 2014). Bailey and Stoll (2013) and Bailey et al. (2014) used numerical simulations to study transport within two-dimensional row oriented canopies when the wind was blowing orthogonally to the row direction. They found that momentum and particle transport in these canopies are functions of canopy architecture. In particular for momentum transport, the horizontal heterogeneity created by the row structure had an impact on second- and third-order momentum statistics, resulted in significant dispersive fluxes in the lower part of the canopy, and preferentially located coherent structure events. When examining massless non-depositing particles, they found that canopy heterogeneity increased vertical particle fluxes, decreased residence time of particles in the canopy, and decreased the persistence of particle motions.

The focus of this study was on sparse perennial agricultural canopies organized into rows. These types of canopies are typified by trellised canopies of *Vitis vinifera* (grape vineyards). Grape vineyard canopies are approximately two-dimensional with large open spaces creating discontinuities at length scales on the order of the canopy height. This geometry directly impacts the mean velocity field resulting in a rotation of the mean wind towards the row direction (Weiss and Allen, 1976) with direct consequences for vine biophysiology (Tarara et al., 2005). Grape vineyard canopies were of interest due to their direct economic impact (USDA, 2013), the increased use of trellised canopies in a variety of crops (Talaie et al., 2011), and because they share many characteristics with other canopies of importance in agricultural and urban applications including wind breaks (Patton et al., 1998; Raupach et al., 2001; Bouvet et al., 2006; Speckart and Pardyjak, 2014) and urban street canyons (Belcher, 2005; Klein et al., 2007; Addepalli and Pardyjak, 2013).

We hypothesized that the sparse geometry of grape vineyard canopies and other canopies with similar characteristics, through its influence on the mean wind and local fluxes, would play a central role in determining particle dispersion dynamics within and above the canopy. Specifically, we expected that the canopy would affect the mean advection direction, the rate of plume spread, and the shape of the spanwise profile of the plume. To test this hypothesis, a field campaign (Section 2) was conducted in a vineyard in Western Oregon. Particle transport was studied through a series of controlled particle release experiments using polyethylene microspheres with a size range similar to spores of multiple fungal grape pathogens. A high density, three-dimensional array of samplers was used to collect the microspheres allowing for the plume shape to be investigated in detail. The momentum transport statistics within the vineyard (Section 3) and the results of the release events were used to elucidate the canopy's influence on particle dispersion (Section 4).

2. Field campaign

The field study was performed during September and October 2011 in a commercial vineyard in the Willamette valley near Monmouth, Oregon at ≈44° 49′ 28.0″ N, 123° 14′ 17.0″ W. The vineyard is a relatively flat site of ≈43 hectares with vine rows oriented to within ±2° of true north-to-south. The experiments were conducted in the southeast portion of the field where the plant growth was the most homogeneous. The wind at this location came primarily from the north and southwesterly directions providing a maximum upstream fetch (>350 m) composed of nearly continuous trellised vines. The terrain had a west-to-east downslope of ≈2.4% and a south to north down slope of ≈0.8%.

Throughout the experiment, a meteorological tower (Fig. 1) with four Campbell Scientific CSAT3 sonic anemometers was placed in the aisle between two rows of vines with the anemometers pointing to true north. The anemometers were placed at heights of 5, 2.9, 1.8, and 0.8 m. The lowest two anemometers were placed such that the bottom and top of the canopy immediately around the tower were within their sampling volumes. Additionally, the sampling volume of the 1.8 m anemometer was aligned with the canopy's top-most trellis wire. The anemometers collected tri-directional wind data [streamwise (u), spanwise (v), and vertical (w)] and the sonic temperature (T) at each height. The meteorological data were recorded 24 h/day at 20 Hz using a Campbell Scientific CR5000 Datalogger.

The surrounding canopy had an average height (h) of 1.90 m with local variation from one plant to the next (Fig. 1). The vine rows were spaced (r_s) at 2.49 m on center and were ≈0.46 m wide leaving aisles of ≈2 m wide. The leaf area density (*LAD*, one-sided area of leaves per canopy volume) profile (Fig. 2) was determined by randomly selecting ten vines within the sample area, counting the number of shoots per vine, and randomly removing a shoot from the left and right of the trunk. Leaves from each shoot were removed and digitally assessed for leaf area using Assess Image Analysis Software (The American Phytopathological Society, St. Paul, MN). The leaf area index (*LAI*, area of leaves per area of ground) was determined based on the same data and was found to be 1.4 for the whole vineyard block. When an individual row of vines was considered with the ground directly beneath it the *LAI* was 7.5. Similar *LAI* values were reported in Johnson et al. (2003) for vineyards of comparable architecture.

2.1. Meteorological data processing

The data from the meteorological tower was partitioned into independent continuous 30-min periods. This period length was sufficient to ensure convergence of flux statistics while maintaining flow steadiness. The mean wind direction for each period at each anemometer height was determined and periods with southerly winds between 165° and 195° (coming from behind the tower) at any height were excluded from further analysis. A three-dimensional coordinate rotation was then applied to the wind velocity data of the $z = 5$ m anemometer for each period so that only u had an average >0 (see Pardyjak and Cuerva, 2007). The wind velocity data for the lower three anemometers were rotated following the rotation determined at the 5 m anemometer.

Standard relevant statistics including the average streamwise velocity at $z = 5$ m ($\overline{u}$) and the mean wind direction at that height

Fig. 1. A picture and schematic of the meteorological tower in the vineyard as well as other relevant canopy dimensions. Photographer was facing due South. The top anemometer was at 5.0 m above the ground and thus ≈3.1 m above the average canopy top.

($\overline{wd}$) were determined for each of the 30-min periods. The friction velocity (u_*) was also determined at the canopy top as,

$$u_{\star,h} = \left[\overline{u'w'}^2 + \overline{v'w'}^2\right]_h^{1/4}, \quad (1)$$

where the overlines represent time-averaged mean values taken over the 30-min period and the primes represent deviations from those means. The subscript h is used to indicate values determined at the canopy height, as is a standard practice for vegetative canopy flows (e.g., Dupont and Patton, 2012; Bailey and Stoll, 2013).

The local atmospheric stability was assessed at the canopy top for each period and was defined as the ratio of h to the Obukhov length (L) determined at that height. The Obukhov length was defined by,

$$L = \frac{-T_o u_{\star,h}^3}{\kappa g(\overline{w'T'})_h}, \quad (2)$$

where κ was the von Kármán constant (=0.4), T_o was the mean absolute temperature at h, g was the acceleration due to gravity, and T was linearly detrended to eliminate large diurnal variations. The periods were then grouped into five categories identified as convective (C, $h/L < -0.31$), moderately convective (MC, $-0.31 < h/L \leq -0.01$), neutral (N, $-0.01 < h/L \leq 0.03$), moderately stable (MS, $0.03 < h/L \leq 0.6$), and stable (S, $h/L > 0.6$) following Mahrt (1998), Launiainen et al. (2007), and Dupont and Patton (2012).

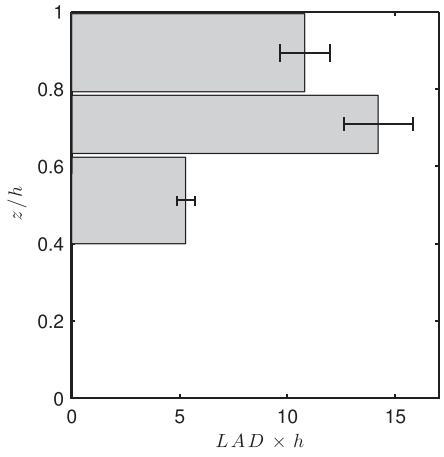

Fig. 2. The profile of the leaf area density for the vineyard canopy. The error bars represent one standard deviation in the LAD among the vines that were tested.

2.2. Point release dispersion experiments

Several research studies have used biological particles (e.g., Aylor and Ferrandino, 1989; Klein et al., 2003) or inert particles as biological surrogates (e.g., Hage, 1961; Bouvet et al., 2006) to characterize particle transport in plant canopies. We used fluorescent polyethylene microspheres. Six microsphere release events were conducted at times when $\overline{wd}$ was approximately parallel to the row direction (from the North). Both yellow (UVPMS-BY2-1.00, Cospheric LLC) and orange (UVPMS-BO-1.00, Cospheric LLC) microspheres with >90% within the diameter range of 10–45 μm were released in the canopy during each event. To determine the diameter distributions, microspheres were suspended in 0.05% v/v Tween 20 solution, pipetted onto a hemocytometer plate, and a custom glass cover slip was used to orient the microspheres into one focal plane. Images were then taken using a Leica MZFLIII fluorescence stereo microscope with a 360/40 nm excitation filter, Leica DFC 310FX camera, and Leica Application Suite image capture software (Leica Microsystems, Wetzlar, Germany). The images were analyzed using Assess Image Analysis Software (The American Phytopathological Society, St. Paul, MN). Three microsphere suspensions with two sub-samples per suspension were analyzed and the size distributions determined.

The average diameters for the microspheres were 30.2 and 34.1 μm for the yellow and orange spheres, respectively. The diameters corresponding to the microspheres of average mass were 32.8 and 35.5 μm, respectively. The microspheres' size range included the average hydraulic diameter of *Erysiphe necator* (grape powdery mildew) spores, ≈27 μm with a range of 20–36 μm (Braun, 1995). Other pathogens of grapes, including *Botrytis cinerea* (diameters of 8–12 μm Jarvis, 1977) and *Plasmopara viticola* (diameters of 30–50 μm Waterhouse, 1973), also have sporular hydraulic diameters within the microsphere diameter range. The microspheres had a density (1.005 g/cm^3) similar to many fungal spores (Gregory, 1973). Past studies have found that the terminal settling velocity

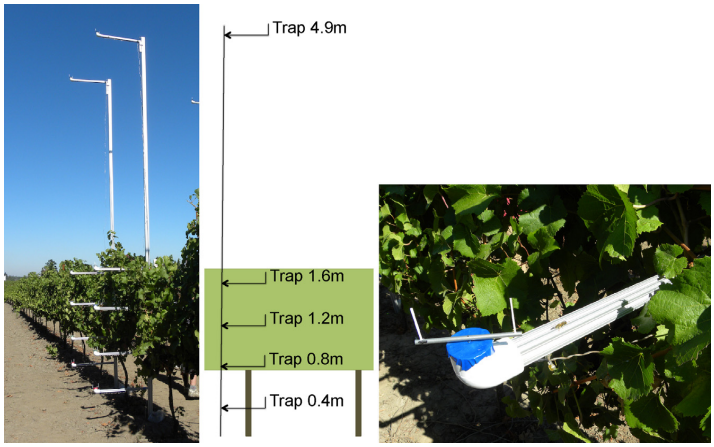

Fig. 3. A picture of an impaction trap tower in the vineyard with a schematic showing the impaction trap heights, as well as a picture of an individual rotating arm impaction trap.

for unit density, sub-100 μm spheres (Chamberlain, 1975) and for fungal spores (Gregory, 1973) can be accurately predicted using Stokes law. Based on Stokes law the settling velocities for microspheres with diameters of 30–35 μm vary from 2.8 cm/s to 3.9 cm/s, respectively.

During each release event, the two colors of microspheres were released simultaneously from separate release devices at different heights, H_r (Table 1). The devices were positioned one above the other within an aisle of the canopy and ≈0.25 m west of the nearest row of vines. The release devices were made of 10.5 cm polypropylene funnels with press-fit precision machined aluminum tips. An orifice of 210 μm in each tip provided a steady flow of microspheres from the funnels when they were vibrated using micro-vibration motors similarly to Bouvet et al. (2006).

The concentration of the released microspheres was sampled at 100 separate locations downwind of the source during each release event. The collection was done using custom rotating arm impaction traps based on Thiessen et al. (2015) and similar to Davis et al. (1997), Aylor and Flesch (2001), and Chamecki et al. (2012). The traps consisted of Mabuchi RF-520C-17410 DC motors supplied with 6 volts (~2550 RPMs) and a sampling arm with a 38 mm radius. The two sample rods were 1.5 mm × 1.5 mm × 40 mm polystyrene coated with a thin film of high vacuum grease (Dow Corning, Midland, MI). Traps were mounted at five different heights on 20 towers. The towers were custom made using 80/20 aluminum T-channel (Fig. 3) and were arranged in an array downwind of the source (Fig. 4). The array consisted of four lines of towers, each oriented orthogonally to the vine row direction at different downwind distances. The impaction traps and release devices were simultaneously turned on and off remotely using controllers on an Xbee wireless mesh network (Digi International Inc.).

The sample rods from each impaction trap were collected then imaged with the fluorescence stereo microscope. To avoid sampling error created by flow alteration at either end of the sampling rods, only 14.2 mm near the center of the length of the sample rods was used. The collection efficiency of this area of the rods was >99.98% according to the modified Stokes theory of Moran et al. (2013).

Table 1
Microsphere release event information for each of the six release events. The duration of each event is listed as well as the mass of each color of microspheres released in that time, and the height from which the different colored microspheres were released.

Event	Duration (min)	Color	Mass (g)	H_r (m)
1	5	Y	0.20	1.7
		O	0.16[a]	0.7
2	5	Y	0.24	1.7
		O	0.37	0.7
3	7	Y	0.16	1.2
		O	0.83	0.7
4	7	Y	0.23	1.2
		O	0.59	0.7
5	7	Y	0.50	1.7
		O	0.34	0.7
6	7	Y	0.73	1.7
		O	0.88	0.7

[a] Mass released was likely higher. See Section 4.

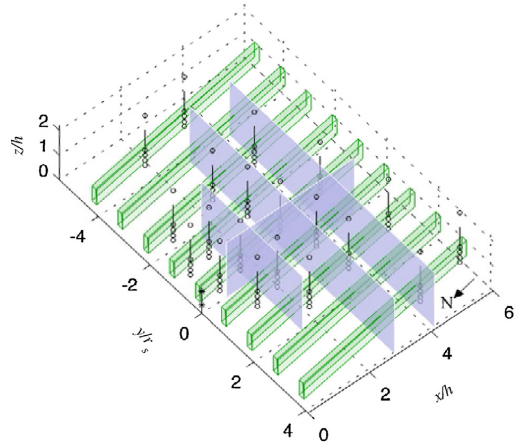

Fig. 4. An example schematic of the vineyard (green boxes) showing the three $y-z$ planes and the $x-z$ plane that Π was interpolated onto using a tri-linear approach (*gray surfaces*) for release event number 5. The locations of the individual impaction traps (*black circles*), and the release mechanisms (*black stars*) are also shown. The left-hand-rule coordinate system is set such that x follows $\overline{wd}$ and y is perpendicular to it.

The number of microspheres, of each color, collected by each impaction trap, for each event, was counted and converted into a scaled concentration, Π, with units of m^{-2}. It was defined as,

$$\Pi = \frac{\mathcal{M}\,\overline{u_h}}{\mathcal{V}\,q} \tag{3}$$

where $\mathcal{M}$ was the total mass of microspheres collected, $\mathcal{V}$ was the total volume swept by the trap during the release event, $\overline{u_h}$ was a streamwise velocity scale taken as the wind speed at the canopy top, and q was the plume source strength in g/s determined from the total mass released and the release event duration. The swept volume was calculated using the speed of each individual impaction trap motor determined in the field with an optical tachometer, the duration of the release event, and the area of the photographed portion of the sample rods. The mass was calculated using the number of microspheres on the sample rods and the average mass of the microspheres. The use of the average mass may have introduced some error into the values for Π, particularly at locations where few microspheres were collected. The standard deviations of the microsphere masses were 69% and 47% of the means for the yellow and orange microspheres, respectively. Values for Π for each impaction trap for each plume are included in the Supplementary Data as Appendix B.

Tri-linear interpolation was used to transfer the Π data at each of the trap locations onto five planes of interest within the tower array. Plume shape characteristics like the plume width are typically defined on planes that run orthogonally to the mean plume advection direction which is usually defined by the mean wind direction. The ordinal directions in the canopy were assigned a coordinate system of $+x'$ to the south and $+y'$ to the west with the origin at the release location. A rotated coordinate system based on $\overline{wd}$ was also defined for each event with the streamwise direction denoted as x and the spanwise axis denoted as y with positive values to the right when viewed from the release location. The first three interpolation planes that Π was transferred to were defined orthogonally to the x axis at distances of x = 3.0, 5.5, and 8.0 m (1.57h, 2.89h, and 4.21h) and stretching from the lowest impaction trap height (0.4 m) to the top impaction trap height (4.9 m) and from the extreme west to extreme east edges of the tower array (Fig. 4). Plume shape parameters are evaluated in Section 4 using these $y-z$ planes. The fourth plane was along x and spanned from approximately x/h = 0.8 to the downwind edge of the tower array, and again from the lowest to the highest impaction trap height. The final interpolation plane was the $x-y$ plane at the height of the impaction traps that were closest to but lower than H_r.

3. Momentum transport results

Wind direction and magnitude were examined using wind roses composed of data from all of the 30-min periods with winds from acceptable directions (Fig. 5). Periods with southerly winds between 165° and 195° (coming from behind the tower) at any height were excluded from further analysis. The wind velocity generally decreased at lower heights in the canopy and the flow within the canopy was channeled parallel to the vine rows regardless of $\overline{wd}$. While $\overline{wd}$ was primarily from the north and southwesterly directions, the flow in the canopy came primarily from one small sector at due north with a few periods from the south-southwesterly direction. The flow channeling was consistent with previous vineyard observations where the amount of turning was related to the incident wind direction with respect to the canopy elements (Weiss and Allen, 1976; Tarara et al., 2005).

The more convective periods had increased likelihood of northerly winds, while more stable periods were likely to occur

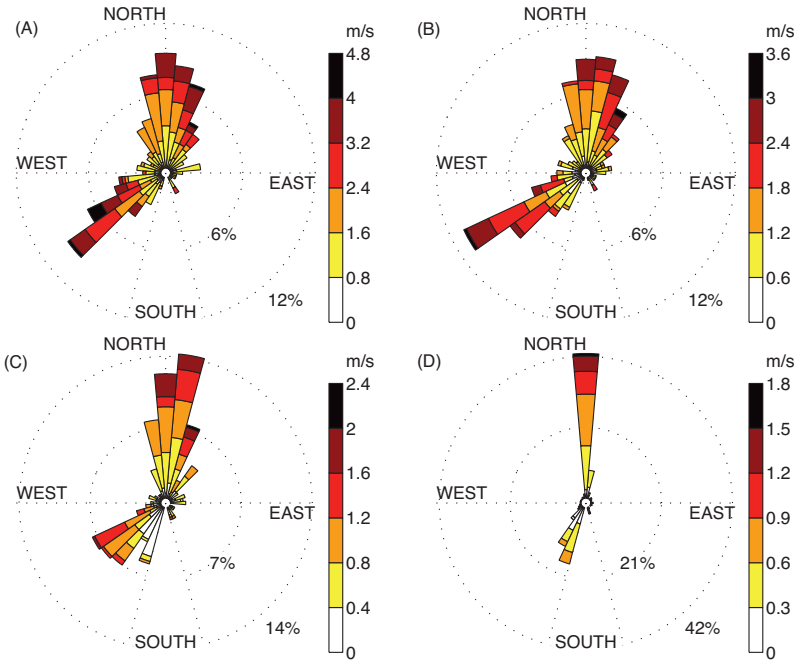

Fig. 5. Wind roses of the 399 half-hour periods showing the percentage of periods per directional sector and the percentage of periods in different windspeed categories. (A), (B), (C), and (D) are for the 5 m, 2.9 m, 1.8 m, and 0.8 m anemometers, respectively. Each directional segment is 10° wide and is centered at multiples of 10°. The segments between 165° and 195° were removed due to tower wake interference.

Table 2
The number of 30-min periods in each of the 10 direction-stability classifications as well as the average streamwise velocity determined at $z = 5$ m and at the canopy top, the friction velocity, and the turbulent temperature scale ($\theta_{*,h} = -\overline{w'T_h'}u_{*,h}^{-1}$) both determined at the canopy top for the periods in each category. Standard deviations calculated across the periods in each category are included after the ± symbols. The stability class thresholds were defined in Section 2.1.

Direction	Stability	Period Count	$\overline{u}$ (m/s)	$\overline{u_h}$ (m/s)	$u_{*,h}$ (m/s)	$\theta_{*,h}$ (°)
Parallel	C	3	1.48 ± 0.23	0.75 ± 0.12	0.19 ± 0.02	−0.58 ± 0.21
	MC	44	2.29 ± 0.90	1.14 ± 0.46	0.27 ± 0.10	−0.19 ± 0.13
	N	10	2.51 ± 0.70	1.25 ± 0.39	0.28 ± 0.08	0.003 ± 0.04
	MS	24	1.45 ± 0.51	0.63 ± 0.30	0.14 ± 0.05	0.08 ± 0.05
	S	5	1.50 ± 1.27	0.66 ± 0.70	0.14 ± 0.15	1.21 ± 2.28
Cross	C	14	0.98 ± 0.33	0.50 ± 0.18	0.14 ± 0.05	−0.52 ± 0.39
	MC	106	2.15 ± 0.92	0.97 ± 0.42	0.29 ± 0.12	−0.22 ± 0.16
	N	80	2.64 ± 0.92	1.10 ± 0.35	0.34 ± 0.13	0.02 ± 0.03
	MS	94	1.27 ± 0.42	0.45 ± 0.21	0.12 ± 0.05	0.11 ± 0.07
	S	19	0.96 ± 0.24	0.26 ± 0.06	0.05 ± 0.01	0.17 ± 0.06

with winds out of the west and south. This behavior is attributed to the topography of the region. During convective times (typically during the midday and afternoon hours), the winds exhibited upvalley flow (Whiteman, 2000), blowing up the Willamette Valley from north to south. During stable times (typically at night) the winds had lower speed and blew downslope from the hills to the west toward the Willamette River or down the valley following the direction of the river, south to north.

The 0.8 m anemometer wind rose indicated that the channeled flow direction was between either 155° and 215° or 355° and 15°. All periods with $\overline{wd}$ (the mean wind direction at $z = 5$ m) within one of these ranges were considered to be periods of *parallel flow* and were used to determine standard profiles for *parallel flow* in the vineyard. All remaining periods were categorized as *cross flow*. Average meteorological statistics, including the streamwise velocity at $z = 5$ m as well as the velocity, friction velocity, and temperature scale at the canopy top for the periods in each of the five stability classes and two direction classes were determined (Table 2).

The microsphere release events were all performed when $\overline{wd}$ was between 346° and 22°. Hence, they were categorized as having been done during times of *parallel flow*. Four of the release events were categorized as MC, one as N, and one as MS (see Table 3 in Section 4). For the remainder of the momentum analysis, only these three categories of *parallel flow* were considered.

Meteorological profiles for the MC, N, and MS categories showed that periods with MC stability exhibited different behavior than the MS periods (Fig. 6). The MC velocity profile had a shallower slope than the MS profile, but the two exhibited nearly equivalent downward momentum fluxes (Fig. 6A and B, respectively). These profiles are comparable to those reported in previous canopy studies (e.g., Aylor and Ferrandino, 1989; Finnigan, 2000; Dupont and Patton, 2012). The periods with a MC stability had higher temperatures near the ground and a steep decline (compared to the MS periods and the dry lapse rate) to 5 m while the MS periods had relatively low but uniform temperatures in the canopy with warmer air aloft (Fig. 6C). The N periods had behavior between the MC and MS periods.

The contrasting temperature slopes contributed to the MC periods exhibiting upward heat flux in and above the canopy, the MS periods exhibiting a downward flux over the same height range, and the N periods exhibiting mixed upward and downward fluxes (Fig. 6F). The erratic behavior of the N profile was attributed to a combination of near-zero heat fluxes and the low number of N sampling periods. The observed near neutral temperature profile in the canopy for the MS periods (Fig. 6C) was likely caused by a heat flux convergence into the canopy. While the MC heat fluxes were approximately constant with height, the MS heat flux had a sharp decline in magnitude between the lowest two anemometer levels. Some MS periods even exhibited a positive heat flux at the mid-canopy, as depicted by the error-bars. The decline in the flux in the canopy suggested that relatively warm air was brought down into the canopy from above and was not transferred down through the canopy at the same rate. This same behavior was seen by Dupont and Patton (2012) in their study of a walnut canopy and can likely be explained by the sheltering effects of the canopy itself. During MS periods, typically seen around sunset, it was likely that due to the low energy storage capacity and the latent losses inherent in leaves, the canopy elements decreased in temperature much faster than did the ground. The ground, which had high energy storage capacity, negligible latent losses, and reduced convective losses (compared to ground with no canopy sheltering it), stayed warm for a longer period after sunset, resulting in a heat flux convergence over the height of the canopy. Urban canopy studies have also reported that the canopy sublayer often exhibits a near-neutral stability even when the larger scale forcing was non-neutral (e.g., Hanna et al., 2003).

The normalized velocity standard deviation profile shapes (Figs. 6D and E) were similar across the MC, N, and MS stability classes. The MS periods had the expected decrease in the magnitude of σ_u and σ_w compared to the the other classes, but this decrease is largely explained by u_* and thus the profiles still collapsed for all of the stability classes. The collapse of the vertical momentum flux profiles and the velocity standard deviation profiles, in conjunction with the near neutral temperature profiles within the canopy, suggested that any decrease in mechanical mixing that would have been expected during MS periods (represented by $u_{*,h}$ or $\overline{u_h}$) was compensated for by the sensible heat flux convergence into the canopy. The result was nearly equivalent levels of mixing in the canopy regardless of stability.

Table 3
Table of the meteorological conditions determined during each release event including; $\overline{u}$, $\overline{u_h}$, δ, $u_{*,h}$, and h/L.

Event	Date	Local Time	$\overline{u}$ (m/s)	$\overline{u_h}$ (m/s)	δ (°)	$u_{*,h}$ (m/s)	h/L
1	9/28/11	17:15	2.99	1.13	14.6	0.3315	−0.0024
2	9/28/11	18:28	2.19	0.73	−13.6	0.2150	0.0906
3	9/30/11	11:04	2.73	0.93	21.2	0.3610	−0.0820
4	9/30/11	12:55	2.97	1.04	12.2	0.3651	−0.0511
5	10/13/11	12:01	2.93	0.98	10.7	0.3366	−0.0320
6	10/13/11	13:41	3.13	1.18	−5.7	0.3602	−0.0143

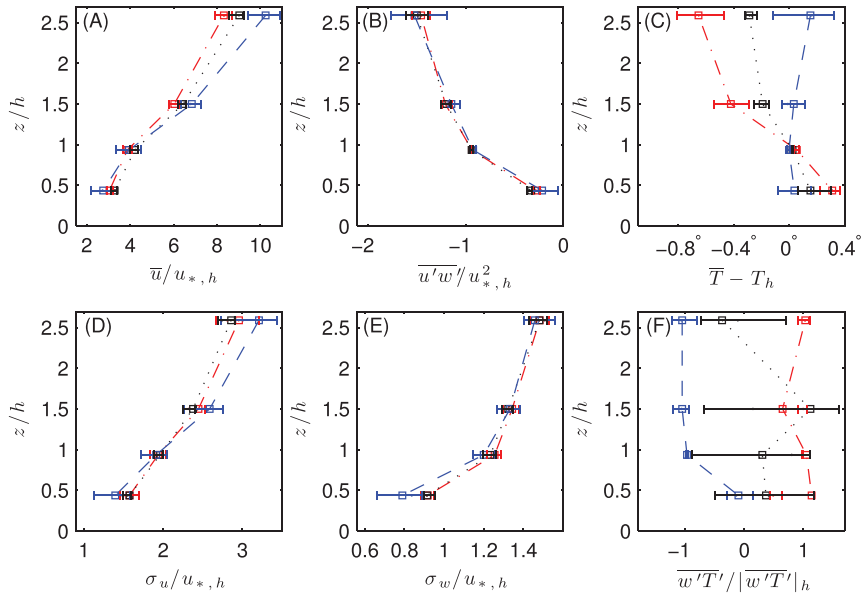

Fig. 6. Mean profiles of the streamwise velocity (A), the vertical momentum flux (B), the temperature (C), the standard deviation of the streamwise velocity (D), the standard deviation of the vertical velocity (E), and the vertical heat flux (F). Variables are normalized using $u_{*,h}$ (Eq. (1)), the temperature at the canopy top (T_h), and the absolute values of the heat flux at the canopy top ($|\overline{w'T'_s}|_h$). The MC periods are *red* with *dot-dashed lines* connecting the means (□). The N periods are *black* with *dotted lines* connecting the means. The MS periods are *blue* with *dashed lines* connecting the means. The error bar ends show the 25th and 75th percentiles of the 30-min periods in each category. The number of periods in each category are listed in Table 2.

4. Dispersion experiment results

Concentrations within each of the 12 microsphere plumes were sampled at 100 locations downwind of the source. This provided a relatively high resolution three-dimensional representation of the near-source plume shape. Most previous dispersion studies in plant canopies sampled concentrations at considerably fewer locations and only along one axis or in one plane (e.g., Aylor and Ferrandino, 1989; Chamecki et al., 2012; Prussin et al., 2014). The few studies that have used three-dimensional arrays (e.g., Raynor et al., 1974; Gleicher et al., 2014) have been in relatively homogeneous and dense canopies and were not able to fully characterize the plume shape in the near-source region. The high-density three-dimensional array used here allowed for improved analyses of the plume shape with fewer *a priori* assumptions like those made by previous researchers including assumptions about plume spread in undersampled or unsampled coordinate directions, assumptions about flow or plume homogeneity, or assumptions about plume symmetry in the spanwise direction.

The mean meteorological conditions including values for $\overline{u}$, $\overline{u_h}$, δ, $u_{*,h}$, and h/L were determined for each of the six release events (Table 3). δ was defined as the difference between $\overline{wd}$ and the row direction (north to south). In this way, δ ranged between -90° and 90° with 0° indicating the wind direction was perfectly parallel to the vines, and $\pm 90^\circ$ meaning it was perfectly perpendicular. A negative δ represented winds from a counter-clockwise rotated direction compared to the vine row direction (westerly), and a positive δ represented winds from a clockwise rotated direction (easterly). All of the release events were conducted during afternoon hours when the winds were similar in speed and direction. The same statistics given in Table 3 were also calculated for 30-minute periods within which the release events were centered. In all six cases the values were nearly indistinguishable from the release period values, suggesting that the meteorological conditions were relatively steady during the events. The data necessary to create profiles of $\overline{u}$, u_*, σ_u, σ_v, σ_w, $\overline{T}$, and $\overline{w'T'}$ for each of the release events can be found in the Supplemental Data as Appendix B.

As an example of the plume shapes observed in the vineyard, the interpolated Π $x-z$ planes for release event 5 are shown along with the $x-y$ planes at the impaction trap height just below H_r (Fig. 7). The actual impaction trap data on the $x-y$ planes were included with the interpolated isolines. Impaction trap data were not included on the $x-z$ planes because no impaction traps landed exactly on that plane (Fig. 4). The highest Π values were observed nearest to the source and decayed with height and in the downwind direction. This behavior compares well with what has been seen in many previous studies, specifically those with three-dimensional arrays in canopies (e.g., Raynor et al., 1974). It was observed that at larger downwind distances ($x > 4h$) Π approached a uniform distribution with height, especially within the canopy. This led to the signature of H_r in the plume being less distinguishable. These same plume features have been reported in other studies (e.g., Huq and Franzese, 2013; Gleicher et al., 2014). The effect of microsphere settling was also identifiable in the $H_r = 1.7$ m plume from the decreasing height of the maximum Π values with downwind distance. The channeling of the flow by the vine rows appeared to have caused the plume to also be channeled into the row direction. This was evidenced by the location of the maximum concentration traveling down the release aisle rather than in the mean wind direction. For release events 2 and 6, when δ was $<0^\circ$ the plume centerline appeared to migrate from the release aisle to the neighboring aisle within $\approx 2h$ downwind of the source (Figs. A3 and A9 of Appendix A of the Supplemental Material).

The three $y-z$ interpolation planes for release event 3 also showed the effect that H_r had on the height of the plume centerline, especially near the source (Fig. 8). The plume shape's lack of dependence on H_r at large downwind distances was manifested

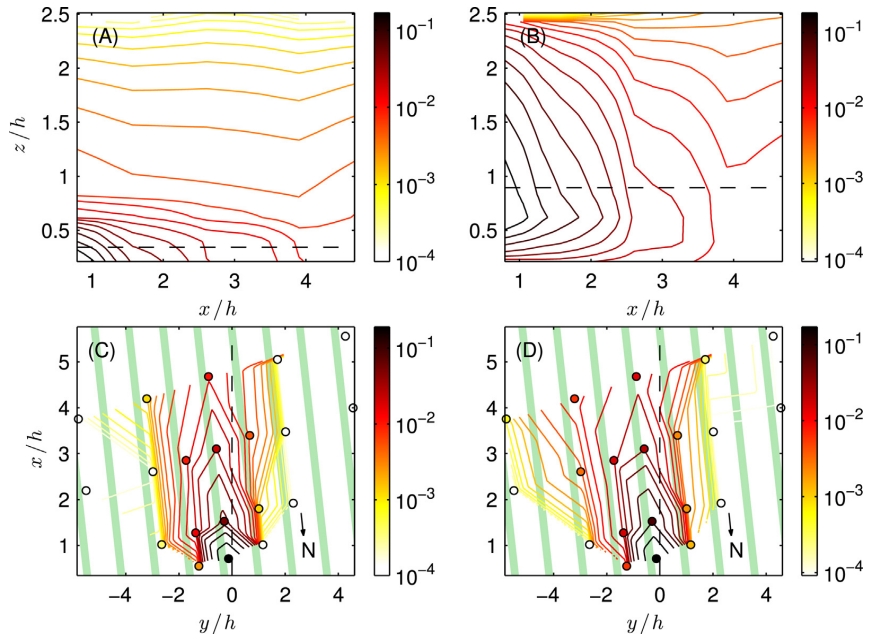

Fig. 7. Scaled concentrations (Π), on a logarithmic scale, from release event 5. (A) and (B) depict the interpolation onto the $x-z$ plane for the plumes with $H_r = 0.7$ m and $H_r = 1.7$ m, respectively. The *black dashed lines* in (A) and (B) represent H_r and the wind was from left to right. (C) and (D) depict the $x-y$ planes for the plume with $H_r = 0.7$ m and $H_r = 1.7$ m, respectively, taken at the impaction trap height just below H_r. The isolines depict the interpolated data while the Π values determined from the impaction traps at their respective locations are shown as the *colored circles*. The *black dashed lines* in (C) and (D) represent $\overline{wd}$, the wind is from bottom to top, and the *green patches* represent the vine rows. (For interpretation of the references to color in this figure legend, the reader is referred to the web version of this article.)

similarly to Fig. 7 in that at the $x = 4.21h$ planes the two plumes appeared very similar. The channeling of the plume by the canopy was again apparent as the maximum Π value did not always occur at $y = 0$ as would be expected if the canopy were not present. The plumes not included in Fig. 8 (Figs. A1–A10 of Appendix A of the Supplemental Material) also exhibited this behavior and indicated that the impact of channeling was related to δ, i.e., for larger $|\delta|$, the effect of the canopy on the plume was greater. This is similar to the channeling effects seen in Hoydysh and Dabberdt (1994) and Yee and Biltoft (2004) for urban flows where the maximum concentration was channeled down street canyons even when the upstream wind was not aligned with those canyons. The main difference between these urban examples and the vineyard is that the vineyard plume channeling is incomplete. It instead appeared to have features characteristic of both an urban channeled plume and of plumes typical of homogenous canopies or the atmospheric surface layer.

The channeling of the plume by the canopy also seemed to have led to the plume concentrations having a spanwise skewness directed from the aisle the plume was channeled down toward $\overline{wd}$. This was most easily observed in the difference in the concentration gradients in the spanwise direction on either side of the concentration maximum (e.g., Fig. 8(D)). It is possible to see a skewness in a spanwise profile of an otherwise non-skewed plume if the plane being studied is not truly orthogonal to the mean plume advection direction. To check that this was not the cause of the skewness seen in the interpolated data and because the in-canopy winds exhibited significant channeling into the row direction (Fig. 5), spanwise profiles taken orthogonally to the vine row direction were also investigated. Consistent behavior between spanwise profiles taken orthogonally to both $\overline{wd}$ and the vine row direction would indicate that the observed skewness was physical and not a function of studying a non-orthogonal plane of a non-skewed plume.

Data on planes taken orthogonally to the vine row direction were available from the uninterpolated impaction trap concentrations (Fig. 4). Individual spanwise profiles of Π taken from those planes confirmed that a spanwise skewness (γ_y) was indeed present in the plumes (Fig. 9). For the $H_r = 1.7$ m plume of release event 1 ($\delta > 0°$), steeper gradients in the profiles were seen to the left of the release aisle and longer tails were seen to the right (toward $\overline{wd}$). The $H_r = 1.7$ m plumes from events 2 and 6 ($\delta < 0°$) tended to have a steeper drop in the concentration to the right of the source and longer tails to the left of the release aisle (again toward $\overline{wd}$). Plumes not depicted in Fig. 9 exhibited similar behavior. Event 6 had the lowest $|\delta|$ and the most nearly symmetric spanwise profiles. A clear example of the skewness behavior of the plumes is depicted in Fig. 9(B) where the skewnesses for events 1 and 2 are approximately mirrored and the profile for event 6 is nearly symmetric. This again indicated that the plumes' shapes, and specifically γ_y, were related to δ and that as $|\delta|$ increased, so apparently did $|\gamma_y|$.

At the x' locations nearest to the source, the concentrations generally decreased with height below H_r. Similar behavior is reported in Aylor and Ferrandino (1989), Yee and Biltoft (2004), and Gleicher et al. (2014). As was observed in Fig. 7, at distances of $x' > 4h$, the shape of any individual plume did not appear to change significantly as a function of the height within the canopy. This was specifically identifiable in the spanwise profiles for event 6 (Fig. 9, subplots (C), (F), and (I)).

Variation in plume shape was apparent with increasing distance x' from the source. This included a clear decrease in the maximum concentrations and changes in γ_y. For event 2, γ_y was negative within the canopy at the first two downwind distances even when

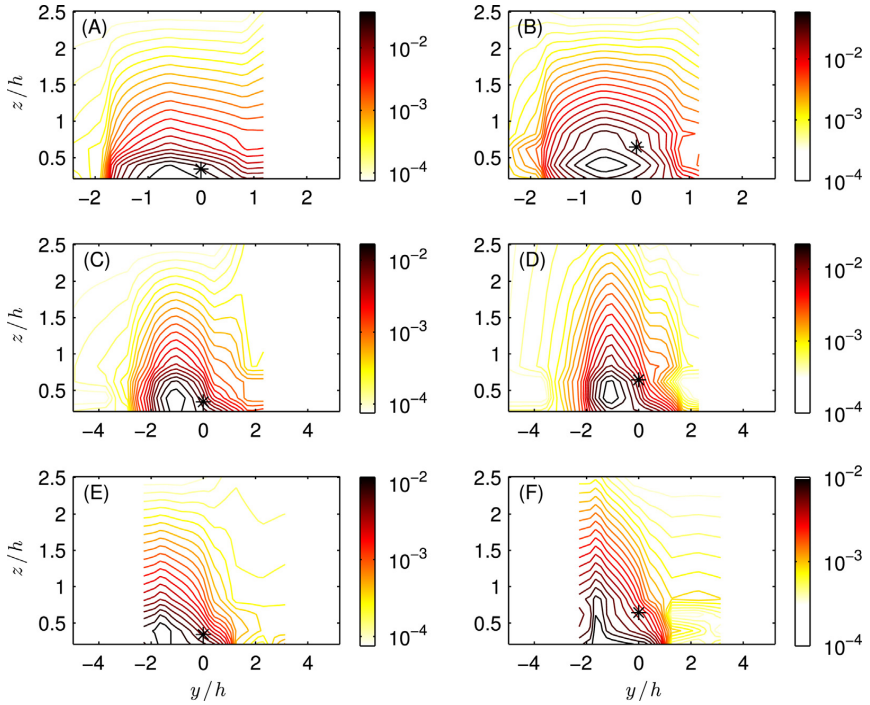

Fig. 8. Scaled concentrations (Π), on a log-scale, at the three downwind cross-wind interpolation planes as viewed from the source location looking along the x axis for release event 3. (A), (C), and (E) depict the plume with H_r = 0.7 m while (B), (D), and (F) depict the plume with H_r = 1.7 m. (A) and (B) are at $x = 1.57h$, (C) and (D) are at $x = 2.89h$, and (E) and (F) are at $x = 4.21h$. The '*' symbols depict the source location on the x axis (i.e. at H_r and $y = 0$).

the maximum concentration appeared to migrate one aisle to the left of the source (visible in the location of the peak in Fig. 9(B)). At the third x' distance however, γ_y appeared to approach zero. This effect was likely due to turbulent mixing causing a general smoothing of the plume profiles. The spanwise profiles for the impaction traps that were located above the canopy (not shown) exhibited more erratic behavior than was seen in the profiles in the canopy. The peak value in these profiles was typically seen at the impaction trap location nearest to the plume centerline defined by $\overline{wd}$. This suggested that because the channeling effects were not present in the freestream, the microspheres that escaped the canopy were typically advected along $\overline{wd}$.

A primary goal of this study was to elucidate the relationship between canopy architecture and plume shape characteristics. Specifically we desired to quantify the plume spread, the spanwise skewness, and the offset of the plume centerline from $\overline{wd}$. Plume spread quantification has been done by many previous researchers using a variety of techniques. Raynor et al. (1970) defined the plume width as the distance between the points on either side of the centerline where the concentration dropped to 10% of the centerline value. Others who had sufficient data density determined the spanwise standard deviation of the plume (σ_y) by its statistical definition (e.g., Gryning et al., 1979; Peterson et al., 1999; Yee et al., 2006). Skelsey et al. (2008) and Prussin et al. (2014) tuned a combination of exponential, power, and Gaussian functions to field data in order to investigate the plumes' shapes. Perhaps the most common approach has been to fit a Gaussian distribution function to the spanwise and/or vertical profiles so that the standard deviations of the plume could be determined statistically from the fit (e.g., Yee and Biltoft, 2004; Venkatram et al., 2013; Huq and Franzese, 2013). Of those mentioned, only Skelsey et al. (2008) defined both σ_y and the standard deviation of the plume in the vertical (σ_z) simultaneously in a single formulation. One reason most others did not do this was that data was not available in both dimensions. None of the cited studies have attempted to quantify a skewness in the spanwise profiles. Because of the observed skewness in the spanwise profiles here (Figs. 7, 8, and 9), and the three-dimensionality of our array, we simultaneously defined σ_y, σ_z, and γ_y through a single formulation.

The spanwise and vertical spread of the plume were determined by fitting a two-dimensional modified Gaussian distribution to the data at each of the three $y-z$ interpolation planes. The skewness of the plumes was accounted for by including a skewness term in the Gaussian fit. The term was drawn from the Skew-Normal Distribution Function (SNDF) described in Azzalini (1985). The two-dimensional skewed Gaussian function that was fit to the data was,

$$\Pi = \frac{A}{2\pi\omega_y\sigma_z}\exp\left(\frac{-(y-\xi_y)^2}{2\omega_y^2}\right)\left[1+\mathrm{erf}\left(\frac{\alpha_y(y-\xi_y)}{\omega_y\sqrt{2}}\right)\right]\left[\exp\left(\frac{-(z-H_e)^2}{2\sigma_z^2}\right)+\exp\left(\frac{-(z+H_e)^2}{2\sigma_z^2}\right)\right], \quad (4)$$

where A was a streamwise magnitude decay parameter, ξ_y was a spanwise offset parameter used to account for channeling, α_y was the skewness parameter in the skewness term, and H_e was the effective height of the plume source defined as $H_e = H_r - \Delta h$ (where Δh was the distance the plume fell after exiting from the release device, analogous to the plume rise used in studies of buoyant plumes (Turner, 1994)). Because a skewness parameter was

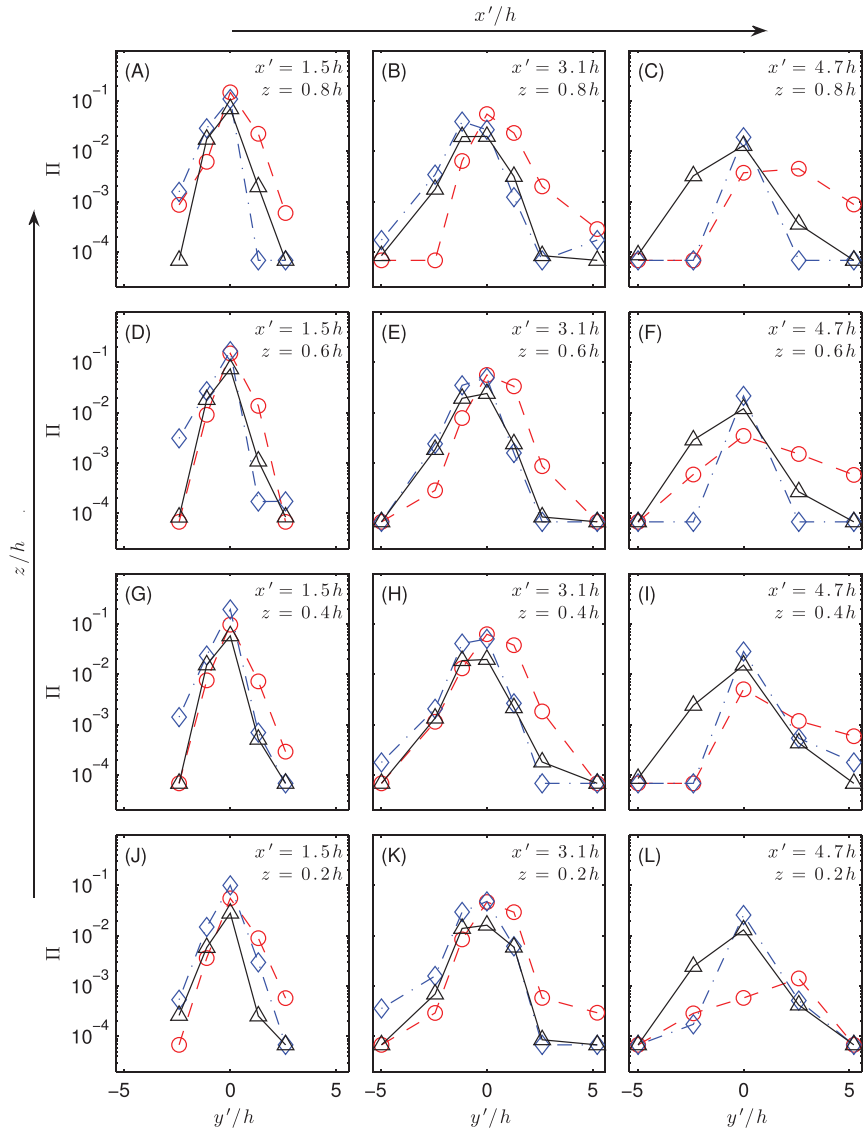

Fig. 9. Spanwise profiles of the scaled concentrations (Π) taken at three separate x' distances from the source for the H_r = 1.7 m plume from events 1, 2, and 6. (A), (B), and (C) depict data from the 1.6 m impaction traps; (D), (E), and (F) are from the 1.2 m impaction traps; (G), (H), and (I) are from the 0.8 m impaction traps; and (J), (K), and (L) are from the 0.4 m impaction traps. (A), (D), (G), and (J) are at $x' = 1.5h$; (B), (E), (H), and (K) are at $x' = 3.1h$, and (C), (F), (I), and (L) are at $x' = 4.7h$. The abscissa is the spanwise distance (y') from the vine row direction normalized by the canopy height (h). The data from event 1 is represented by a *red dashed* line, event 2 is represented by a *blue dot-dashed* line, and event 6 is depicted by a *black solid* line. Symbols for the three events are defined in Table 4. The concentration for impaction traps that collected zero microspheres was set to an arbitrary low value that was less than the traps' minimum detection limits so that an estimation of the concentration gradient could be visualized. (For interpretation of the references to color in this figure legend, the reader is referred to the web version of this article.)

included, ω_y was used in place of the standard Gaussian standard deviation variable σ_y, but the two were related through the SNDF skewness parameter α_y as,

$$\sigma_y = \sqrt{\omega_y^2 \left(1 - \frac{2\alpha_y^2}{\pi\left(1+\alpha_y^2\right)}\right)}. \quad (5)$$

The y location of the mean of the SNDF and therefore of the spanwise concentration profile is related to the offset and skewness parameters as,

$$\mu_y = \xi_y + \omega_y \alpha_y \sqrt{\frac{2}{\pi\left(1+\alpha_y^2\right)}}. \quad (6)$$

If the spanwise skewness were zero then the location of the mean is equal to the offset parameter and also equal to the location of

Table 4
Table of the r^2 values for the fit of Eq. (4) to the interpolated Π data for each microsphere plume at each $y-z$ plane. r^2 was defined as $1-\sum_i(\Pi_{o,i}-\Pi_{I,i})^2/\sum_i(\Pi_{o,i}-\langle\Pi_I\rangle)^2$, where Π_o values were from the optimized version of Eq. (4), Π_I were the interpolated values taken in the field, the subscript i was for an individual index at one of the three $y-z$ planes, and $\langle\rangle$ represented a mean taken over the plane. Symbols are specified for use in the Figs. 10–13.

Event	Symbol	H_r [m]	$x/h=1.57$	$x/h=2.89$	$x/h=4.21$
1	○	1.7	0.994	0.976	0.888
		0.7	0.993	0.955	0.910
2	◊	1.7	0.970	0.969	0.950
		0.7	0.969	0.976	0.945
3	×	1.2	0.928	0.925	0.906
		0.7	0.986	0.967	0.963
4	□	1.2	0.937	0.924	0.854
		0.7	0.933	0.897	0.820
5	*	1.7	0.989	0.969	0.969
		0.7	0.993	0.982	0.958
6	△	1.7	0.992	0.986	0.977
		0.7	0.989	0.970	0.977

the maximum concentration in the spanwise profile. Unfortunately there is no analytical solution for the location of the maximum ($\mu_{y,max}$) in the SNDF. The statistical skewness of the spanwise profile, as taken from the SNDF is,

$$\gamma_y = \left(2-\frac{\pi}{2}\right)\left(\frac{\left(2\alpha_y^2\right)^{3/2}}{\left(\pi\left(1+\alpha_y^2\right)-2\alpha_y^2\right)^{3/2}}\right). \tag{7}$$

Eq. (4) was fit to the data by way of a multi-variable optimization performed in MATLAB (The MathWorks, Inc., version R2010a). The optimization employed the trust-region approach described in Coleman and Li (1996). This included solving for A, σ_z, ω_y, ξ_y, α_y, and Δh at each of the three interpolated $y-z$ planes. For each of the plumes, a minimum of 115 interpolated points were used on each of the three $y-z$ planes. Increases in the interpolation resolution resulted in minimal variation in the values of the shape parameters.

It is important to note that due to the discrete nature of the canopy architecture and the low spanwise spatial resolution of the array relative to the architecture, Eq. (4) should not be perceived as an exact instantaneous representation of the spanwise concentration profile but instead as a tool to estimate average plume spread parameters. Eq. (4) was found to fit the field data very accurately (Table 4) thus giving credence to use of the statistics of the fit for plume shape investigation.

The values for σ_y and σ_z determined for each of the plumes through the multi-variable optimization were the first to be examined. They were non-dimensionalized by spanwise and vertical length scales L_y and L_z, respectively, and plotted as functions of a flight time scale $t=x/\overline{u_h}$ normalized by spanwise and vertical Lagrangian turbulent timescales defined as $T_y=L_y/\sigma_v$ and $T_z=L_z/\sigma_w$, respectively, where σ_v is the standard deviation of the spanwise velocity (Fig. 10). The turbulent timescales were meant to approximate the horizontal and vertical decorrelation timescales in the canopy and therefore velocity data from the canopy top were used (Table 3). These relations were used in Huq and Franzese (2013) and are analogous to those used by others for approximating deccorrelation time scales at the middle of the atmospheric boundary layer (e.g., Hanna, 1981; Degrazia et al., 2001). L_y was set equal to $r_s/2$ and L_z to the canopy height h (Castro et al., 2006).

As the plumes were advected downwind the widths and heights tended to increase. Some correlation was observed between the smoothness of the increase and the quality of the curve fit to the data (Table 4). The plumes for which the curve fit approach best matched the data showed the smoothest and most consistent

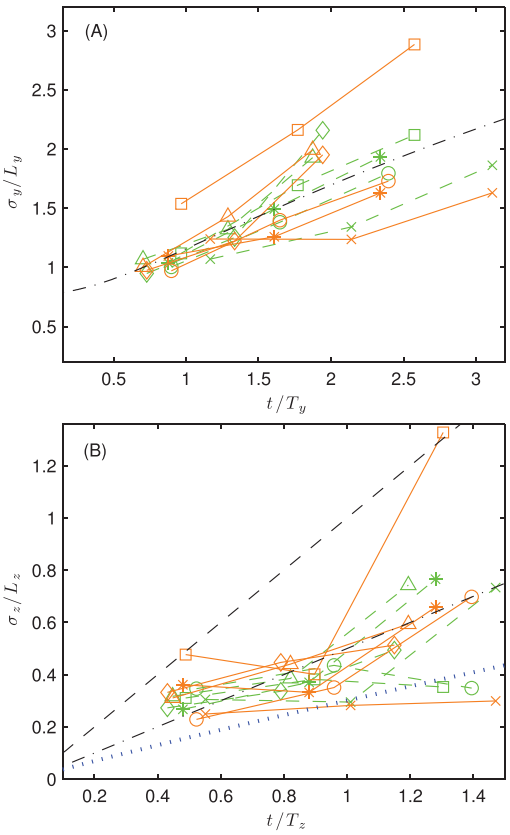

Fig. 10. The standard deviations of the plumes, σ_y (A) and σ_z (B), as well as estimates from formulations found in the literature. Plumes with $H_r \geq 1.2$ m and $H_r = 0.7$ m are represented as *green* and *orange* symbols (Table 4) with *dashed* and *solid* lines, respectively. The *black dot-dashed* line in (A) represents Eq. (8) with $\sigma_{y0}=h/2$ m. The *black* lines in (B) represent Eq. (9) with the *dashed* line using $b=1.0$ and the *dot-dashed* line using $b=0.5$, both with $\sigma_{z0}=0$ m. The *blue dotted* line represents the Pasquill-Gifford formulation for plume spread under Pasquill's class C stability. (For interpretation of the references to color in this figure legend, the reader is referred to the web version of this article.)

growth. The more sporadic lines may have been caused by the shortcomings of the curve fit and not the physics of those plumes. The significant spread of the σ_z values found here is partially attributed to poor concentration resolution near the ground. Particularly for the plumes with $H_r=0.7$ m, when Eq. (4) was fit to the data, a high level of uncertainty was seen in σ_z because the maximum Π was typically seen at the lowest impaction traps and no information was available below 40 cm.

There was no obvious trend observed based on the atmospheric stability at the time of the event. This was attributed to the near-constant level of mixing in the canopy regardless of the stability class (Section 3).

For comparison, the σ_y values for all 12 plumes were plotted along with the relationship used by Franzese and Huq (2011). This relationship, derived from the theory of Taylor (1921) for use in estimating plume spread when $t \approx T_y$, was,

$$\sigma_y^2 = \sigma_{y0}^2 + 2L_y^2\left(\exp\left(\frac{-t}{T_y}\right)+\frac{t}{T_y}-1\right), \tag{8}$$

where σ_{y0} was the spanwise standard deviation of the plume at the point source (Fig. 10A). The plume spread at the source has been shown to be governed by multiple mechanisms (Allwine et al., 2002) and has been related to the relevant scales of the surrounding canopy obstacles (Hanna et al., 2003; Hanna and Baja, 2009). The formulation is shown using $\sigma_{y0} = h/2$ which was recommended by Hanna et al. (2003) for urban canopies. The behavior of σ_z was compared to,

$$\sigma_z^2 = \sigma_{z0}^2 + \frac{b^2 t^2 L_z^2}{T_z^2}, \tag{9}$$

where b was an empirical constant and σ_{z0} was the vertical standard deviation of the plume at the point source. This relationship was used in Franzese and Huq (2011) and Huq and Franzese (2013) and was derived based on Hunt and Weber (1979). Franzese and Huq (2011) reported that values for b of 1.0 and 0.5 worked well for daytime and nighttime conditions, respectively. Eq. (9) with both b values is shown (Fig. 10B) with $\sigma_{z0} = 0$ for both formulations. The Pasquill-Gifford formulation for vertical plume spread under Pasquill's class C stability regime was also included for comparison (Turner, 1994). Class C was used because five of the six release events were performed under MC stability. The Pasquill-Gifford formulation does not include a non-zero initial plume spread and is only applicable for larger transport distances. Neither Eq. (9) nor the Pasquill-Gifford formulation was developed specifically for application to spread within plant canopies, but they approximately covered the range of values and slopes observed in the data. A value of $b = 0.5$ appeared to produce the closest fit to the average of the field data regardless of the stability class of the release event.

It was observed that due to the channeling of the plume within the canopy aisles, the spanwise location of the maximum concentration followed the row direction and therefore, through simple geometry, was offset from $\overline{wd}$ following,

$$\mu_{y,\max} = -x \tan(\delta). \tag{10}$$

After fitting Eq. (4) to each $y-z$ plane of each of the plumes, the spanwise locations of the maximum concentrations were determined numerically. The impaction trap array (Fig. 4) included only one row of trap towers in each aisle and as a result $\mu_{y,max}$ could only be reliably determined to an accuracy of which aisle it was contained in. It was possible that the maximum concentration could have existed at a different spanwise location within the aisle than where the impaction trap was located, and though such a variation could not be known or recreated from the collected data, it would not change the conclusion here that the maximum was always channeled along the aisle of the source. Additionally, there were a few cases where the plume centerline appeared to migrate from the release aisle to one of the neighboring aisles at some distance downwind of the source (Fig. A9). After initially being channeled down the release aisle, enough microspheres were able to migrate to a neighboring aisle that the location of maximum concentration also moved over. When the plume centerline moved one aisle to the west of the source aisle, $\mu_{y,max}$ increased by $\approx 1.0 r_s$, the upper line in Fig. 11. Such a migration of the centerline was possible when $\delta > 0$ and was more likely to occur as $|x\tan(\delta)|$ increased. We hypothesize that such a movement of the plume centerline is almost certain when $|x\tan(\delta)| > r_s$ but more experimentation is needed to test this. When the plume centerline moved one aisle to the east, during events with $\delta < 0$, $\mu_{y,max}$ decreased by $\approx 0.3 r_s$. This was different from the events when $\delta > 0$ because the release device was not centered in the aisle and a smaller change in $\mu_{y,max}$ was sufficient for the plume center to change aisles (Figs. A3 and A9 of Appendix A of the Supplemental Material). This is depicted as the lowest of the three black dot-dashed lines in Fig. 11.

In nearly two-thirds of the pairs of μ_y and $\mu_{y,max}$ values determined from the multi-variable optimization (12 plumes × 3 x distances), $|\mu_y| < |\mu_{y,max}|$ so that the location of μ_y was closer to $\overline{wd}$ than was $\mu_{y,max}$. An approximation of $\mu_y = 2\mu_{y,max}/3$ was determined using a linear regression of all of the pairs where $|\mu_y| < |\mu_{y,max}|$. In four of the pairs where $|\mu_y| > |\mu_{y,max}|$, the plume appeared to have migrated to the neighboring aisle after $\mu_{y,max}$ exceeded $0.3 r_s$ with $\delta < 0$.

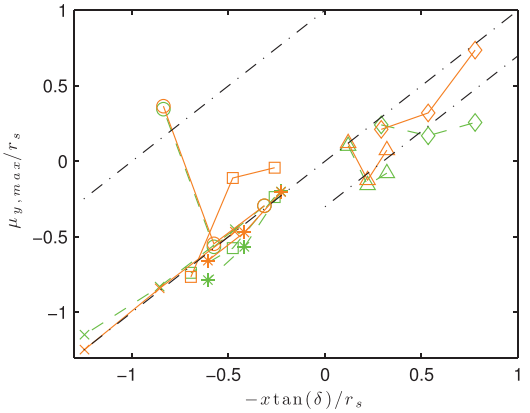

Fig. 11. The location of the numerically determined maximum Π in each plume as a function of the downwind distance and the wind direction. Plumes with $H_r \geq 1.2$ m and $H_r = 0.7$ m are represented as *green* and *orange* symbols (Table 4) with *dashed* and *solid* lines, respectively. The *black dot-dashed* lines represent Eq. (10) with offsets included to account for when the plume centerline migrated to a neighboring aisle. (For interpretation of the references to color in this figure legend, the reader is referred to the web version of this article.)

By definition, the skewness of the SNDF is related to the percentage of the standard deviation that is skewed to one side of μ_y. This also meant that $\mu_{y,max}$ and the skewness were not independent variables and that some relationship must exist between them. Based on these definitions we expected that γ_y would be related to $(\mu_y - \mu_{y,max})/\sigma_y$. However, because no analytical solution exists for $\mu_{y,max}$ in the SNDF, none can exist for this relationship either. The values for γ_y were plotted against $(\mu_y - \mu_{y,max})/\sigma_y$ determined for each of the plumes (Fig. 12). An estimation of the relationship between the variables defined by,

$$\gamma_y = \operatorname{erf}\left(\frac{\pi(\mu_y - \mu_{y,\max})}{2\sigma_y}\right), \tag{11}$$

was determined to match the data exceptionally well. Using a simple random number generation approach, the maximum absolute error that this estimation produced when compared to the optimized γ_y values was only 0.02. Typically for the events where $\delta > 0$, $\mu_{y,max} < \mu_y < 0$. This resulted in $\gamma_y > 0$, meaning that the spanwise concentration profile was skewed from the location of $\mu_{y,max}$ toward the axis of $\overline{wd}$, i.e., in Fig. 8, the gradient on the $\overline{wd}$ side of $\mu_{y,max}$ (right) was more shallow than the gradient to the left of $\mu_{y,max}$. For events with $\delta > 0$, the opposite effect was typical. We hypothesize that this behavior was caused by the directional shear stress caused by the difference in the channeled wind direction and the mean direction of the forcing ($\overline{wd}$). More specifically, that while the bulk of the plume is channeled along the aisle it was released in, the plume is pressed in the direction of $\overline{wd}$ and some portion of the microspheres are able to migrate into neighboring aisles leading to the longer tail in the spanwise profile pointing from the release aisle back toward $\overline{wd}$. This behavior was altered when the plume center migrated to a neighboring aisle but may likely repeat itself by way of the plume becoming channeled in that aisle while still being pressed towards $\overline{wd}$.

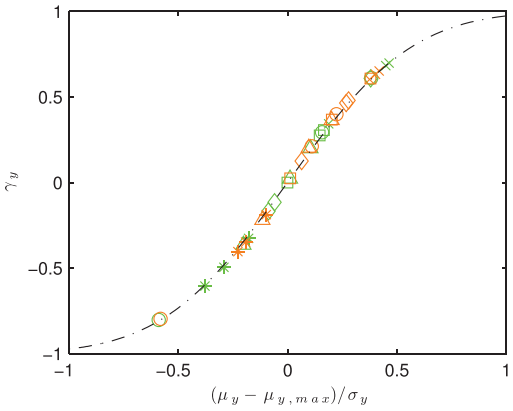

Fig. 12. The relationship between the skewness of the SNDF and the other statistical parameters. Plumes with $H_r \geq 1.2$ m and $H_r = 0.7$ m are represented as *green* and *orange* symbols (Table 4), respectively. The *black dot-dashed* line represents Eq. (11). (For interpretation of the references to color in this figure legend, the reader is referred to the web version of this article.)

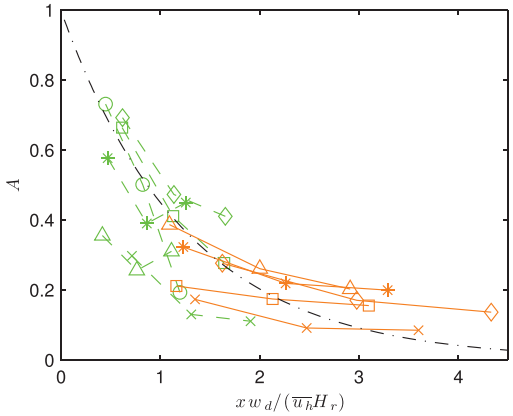

Fig. 13. The multiplier, A, needed to scale the modeled Π values. Plumes with $H_r \geq 1.2$ m and $H_r = 0.7$ m are represented as *green* and *orange* symbols (Table 4) with *dashed* and *solid* lines, respectively. The *black dot-dashed* line represents Eq. (13). (For interpretation of the references to color in this figure legend, the reader is referred to the web version of this article.)

As explained previously, the parameter Δh was the distance that the plume fell below the source height and therefore controls the height of the plume centerline. Due to the limited resolution in the vertical direction, especially in the lower canopy, the values obtained for Δh from the multi-variable optimization procedure had a high degree of uncertainty. This was most pronounced for the events where $H_r = 0.7$ m. Plumes with $H_r \geq 1.2$ m had multiple impaction trap heights below the plume source and so were considered to be more reliable for the determination of Δh. A linear regression performed on the 18 Δh values from these events (6 events × 3 x distances) yielded,

$$\Delta h = 0.30 + 0.039\frac{x}{u_h}. \tag{12}$$

This equation was an interesting result as the slope term had units of velocity and had a value nearly indistinguishable from the expected settling velocity of the microspheres, i.e., 3.9 cm/s. A similar relationship was suggested in Okubo and Levin (1989) to account for the downward trajectory of the centerline of heavy-particle plumes. The intercept value of 30 cm was likely an initial fall distance of the plume at the source, analogous to the initial plume rise used in studies of buoyant plumes (Turner, 1994).

The plume concentration multiplier A was used to scale the values determined by Eq. (4) to match the values collected in the field. A value of 1.0 would suggest that A could be removed from Eq. (4) and all of the released mass would have still been accurately accounted for. For all but one of the experimental plumes, A was <1.0 suggesting that mass was removed from the plumes and not accounted for by the spread alone (Fig. 13). The remaining plume ($H_r = 0.7$ during the first event) was excluded from this analysis as it had values of $A > 1.0$ suggesting that the amount of mass actually released was more than was recorded in the field. It is important to note that the value of A only impacts the concentration magnitudes and does not affect the parameters that define the plume shape (e.g., σ_y, γ_y). Physically, A represented multiple processes in the canopy which worked to deplete the number of spheres in the plume. These processes include deposition onto the plant elements and ground by settling and impaction. Models have been proposed to explain the processes controlling this depletion (e.g., Aylor and Sutton, 1992; Raupach et al., 2001; Pardyjak et al., 2008; Skelsey et al., 2008; Chamecki et al., 2012). We did not investigate these processes in depth here, but simply compared the depletion of microspheres that was observed in the field to,

$$A = \exp\left(-\sqrt{\frac{2}{\pi}}\frac{xw_d}{\overline{u_h}H_r}\right), \tag{13}$$

where w_d is the total deposition velocity of microspheres to both the ground and the vegetation. A least-squares regression found that $w_d = 0.36$ m/s was best for our data. Aylor (1978) and Aylor and Sutton (1992) used a very similar relationship with σ_z in place of H_r. Eq. (13) tended to match the values determined for the depletion of microspheres from the plume in the field reasonably well.

5. Final conclusions

Analysis of the momentum data from the vineyard field experiment showed that the canopy's impact on turbulence statistics taken during *parallel flow* did not differ significantly from that seen in other canopy studies. The architecture did however significantly effect the wind direction within the canopy which resulted in turning of the velocity profile when the winds were not aligned with the vine rows. It was also observed that the total level of mixing in the canopy was maintained by a heat flux convergence even when increasing stability would have caused the mechanical mixing of the flow to decrease. The canopy architecture of a vineyard was found to cause the microsphere plumes to be channeled down the aisles but skewed back toward the mean wind direction. From this we can conclude that the vine row direction is arguably the most important parameter for estimating plume shape. The shape of the plume was studied by fitting a simple bi-directional Gaussian distribution to the field data at three independent downwind distances from the plume source. The statistics from these fits were able to demonstrate the channeling of the plume into the vine row direction by way of an offset parameter that tracked the plume centerline. The skewed nature of the plume was also measured using a skewness term drawn from the SNDF. It is unclear at this time if these same effects would be seen for larger values of δ. Future experiments need to be conducted when $22^\circ < \delta < 90^\circ$. Release events where collection is performed at much larger downwind length scales should also be conducted. We hypothesize that for longer distance transport the near-source effects of the canopy would diminish and the relationships between the architecture and

the values of μ_y and $\mu_{y,max}$ would be altered. All of the statistical parameters of the plume were compared to published functions of simple meteorological and canopy architectural variables. To solidify our understanding of these relationships and improve our confidence in the plume behavior near the ground, experiments with a wider range of meteorological conditions and with the lowest impaction traps closer to the ground are needed. Finally, we believe that in future modeling efforts on dispersion within canopies, and especially those composed of discrete elements, definitions of canopy architecture need to exist in the models. Simply using a homogeneous canopy density analogy will never be able to reproduce results like the spanwise skewness observed here.

Acknowledgements

This work was funded by the United States Department of Agriculture (USDA) project 5358-22000-039-00D, the National Science Foundation grant AGS 1255662, and the University of Utah's Global Change and Sustainability Center. We thank Cole Provence, Jim Eynard, Andy Albrecht, Jessica Keune, and Tom Loveday for their excellent assistance with the field campaign. The use trade, firm, or corporation names in this publication are for information and convenience of the reader. Such use does not constitute an endorsement or approval by the USDA or the Agriculture Research Service of any product or service to the exclusion of others that may be suitable.

Appendix A. Supplementary data

Supplementary data associated with this article can be found, in the online version, at http://dx.doi.org/10.1016/j.agrformet.2015.06.003

References

Addepalli, B., Pardyjak, E.R., 2013. Investigation of the flow structure in step-up street canyons – mean flow and turbulence statistics. Boundary-Layer Meteorol. 148, 133–155.
Allwine, K.J., Shinn, J.H., Streit, G.E., Clawson, K.L., Brown, M., 2002. Overview of Urban 2000: a multiscale field study of dispersion through an urban environment. Bull. Amer. Meteor. Soc. 83, 521–536.
Aylor, D.E., 1978. Dispersal in time and space: Aerial pathogens. In: Horsfall, JG., Cowling, EB. (Eds.), Plant Disease: An Advanced Tretise. Vol. 2. Academic Press, New York, pp. 159–180.
Aylor, D.E., Ferrandino, F.J., 1989. Dispersion of spores released from an elevated line source within a wheat canopy. Boundary-Layer Meteorol. 46, 251–273.
Aylor, D.E., Flesch, T.K., 2001. Estimating spore release rates using a Lagrangian stochastic simulation model. J. Appl. Meteor. 40, 1196–1208.
Aylor, D.E., Fry, W.H., Mayton, H., Andrade-Piedra, J.L., 2001. Quantifying the rate of release and escape of Phytophthora infestans sporangia from a potato canopy. Phytopathology 91, 1189–1196.
Aylor, D.E., Sutton, T.B., 1992. Release of *Venturia inaequalis* ascospores during unsteady rain: Relationship to spore transport and deposition. Phytopathology 82, 532–540.
Azzalini, A., 1985. A class of distributions which includes the normal ones. Scand. J. Stat. 12 (2), 171–178.
Bailey, B., Stoll, R., 2013. Turbulence in sparse, organized vegetative canopies: a large-eddy simulation study. Boundary-Layer Meteorol. 147, 369–400.
Bailey, B.N., Stoll, R., Pardyjak, E.R., Mahaffee, W.F., 2014. Effect of vegetative canopy architecture on vertical transport of massless particles. Atmos. Env. 95, 480–489.
Belcher, S.E., 2005. Mixing and transport in urban areas. Philos. Trans. R. Soc. A 363, 2947–2968.
Böhm, M., Finnigan, J.J., Raupach, M.R., Hughes, D., 2013. Turbulence structure within and above a canopy of bluff elements. Boundary-Layer Meteorol. 146, 393–419.
Bouvet, T., Wilson, J.D., Tuzet, A., 2006. Observation and modeling of heavy particle deposition in a windbreak flow. J. Appl. Meteorol. Climatol. 45, 1332–1349.
Braun, U., 1995. The Powdery Mildews (Erysiphales) of Europe. Gustav Fischer Verlag, New York, pp. 337.
Cassiani, M., Katul, G.G., Alberston, J.D., 2008. The effects of canopy leaf area index on airflow across forest edges, Large-eddy simulation and analytical results. Boundary-Layer Meteorol. 126, 433–460.
Castro, I.P., Cheng, H., Reynolds, R., 2006. Turbulence over urban-type roughness, Deduction from wind-tunnel measurements. Boundary-Layer Meteorol. 118, 109–131.
Chamberlain, A.C., 1975. The movement of particles in plant communities. In: Monteith, J.L. (Ed.), Vegetation and the Atmosphere. I. Principles. Academic Press, New York, pp. 155–203.
Chamecki, M., Default, N.S., Isard, S.A., 2012. Atmospheric dispersion of wheat rust spores: a new theoretical framework to interpret field data and estimate downwind dispersion. J. Appl. Meteorol. Climatol. 51, 672–685.
Coleman, T.F., Li, Y., 1996. An interior trust region approach for nonlinear minimization subject to bounds. SIAM J. Optim. 6, 418–445.
Davis, J.M., Eisner, A.D., Wiener, R.W., Main, C.E., 1997. A flow visualization study of spore release using a wind tunnel-mounted laser light sheet. Plant Dis. 81, 1057–1065.
Degrazia, G.A., Campos, C.R.J., Carvalho, J.C., Anfossi, D., Goulart, A.G., 2001. Turbulence parameterisation for Lagrangian stochastic dispersion models. Rev. Bras. Meteorol. 16 (2), 123–134.
Detto, M., Katul, G.G., Siqueira, M., Juang, J.Y., Stoy, P., 2008. The structure of turbulence near a tall forest edge: the backward-facing step flow analogy revisited. Ecol. Appl. 18, 1420–1435.
Dupont, S., Brunet, Y., 2008. Influence of foliar density profile on canopy flow: a large-eddy simulation study. Agric. For. Meteorol. 148, 976–990.
Dupont, S., Patton, E.G., 2012. Influence of stability and seasonal canopy changes on micrometeorology within and above an orchard canopy. The CHATS experiment. Agric. For. Meteorol. 157, 11–29.
Dwyer, M.J., Patton, E.G., Shaw, R.H., 1997. Turbulent kinetic energy budgets from a large-eddy simulation of airflow above and within a forest canopy. Boundary-Layer Meteorol. 84, 23–43.
Ferrandino, F.J., 1993. Dispersive epidemic waves: I. Focus expansion within a linear planting. Phytopathology 83, 795–802.
Finnigan, J.J., 2000. Turbulence in plant canopies. Ann. Rev. Fluid Mech. 32, 519–571.
Franzese, P., Huq, P., 2011. Urban dispersion modelling and experiments in the daytime and nighttime atmosphere. Boundary-Layer Meteorol. 139, 395–409.
Gleicher, S.C., Chamecki, M., Isard, S.A., Pan, Y., Katul, G.G., 2014. Interpreting three-dimensional spore concentration measurements and escape fraction in a crop canopy using a coupled Eulerian? Lagrangian stochastic model. Agric. For. Meteorol. 194, 118–131.
Gregory, P.H., 1973. The Microbiology of the Atmosphere. Leonard Hill Books, London, pp. 377.
Gryning, S.E., Lyck, E., Hedegaard, K., 1979. Short-range diffusion experiments in unstable conditions over inhomogeneous terrain. Tellus 30, 392–403.
Hage, K.D., 1961. On the dispersion of large particles from a 15-m source in the atmosphere. J. Meteorol. 18, 534–539.
Hanna, S.R., 1981. Lagrangian and Eulerian time-scale relations in the daytime boundary layer. J. Appl. Meteorol. 20, 242–249.
Hanna, S.R., Britter, R., Franzese, P., 2003. A baseline urban dispersion model evaluated with Salt Lake City and Los Angeles tracer data. Atmos. Environ. 37, 5069–5082.
Hanna, S.R., Baja, E., 2009. A simple urban dispersion model tested with tracer data from oklahoma city and manhattan. Atmos. Environ. 43, 778–786.
Hoydysh, W.G., Dabberdt, W.F., 1994. Concentration fields at urban intersections: fluid modeling studies. Atmos. Environ. 28, 1849–1860.
Huang, J., Cassiani, M., Albertson, J.D., 2009. The effects of vegetation density on coherent turbulent structures within the canopy sublayer: a large-eddy simulation study. Boundary-Layer Meteorol. 133, 253–275.
Hunt, J.C.R., Weber, A.H., 1979. A Lagrangian statistical analysis of diffusion from a ground-level source in a turbulent boundary layer. Q. J. R. Meteorol. Soc. 105, 423–443.
Huq, P., Franzese, P., 2013. Measurements of turbulence and dispersion in three idealized urban canopies with different aspect ratios and comparisons with a Gaussian plume model. Boundary-Layer Meteorol. 147, 103–121.
Jarvis, W.R., 1977. Botryotinia and Botrytis species: Taxonomy, physiology, and pathogenicity. A guide to the literature. Research Branch, Canada Department of Agriculture, Harrow, Ontario, pp. 195.
Johnson, L.F., Roczen, D.E., Youkhana, S.K., Nemani, R.R., Bosch, D.F., 2003. Mapping vineyard leaf area with multispectral satellite imagery. Comput. Electron. Agric. 38, 33–44.
Judd, M.J., Raupach, M.R., Finnigan, J.J., 1996. A wind tunnel study of turbulent flow around single and multiple windbreaks, Part I. Velocity fields. Boundary-Layer Meteorol. 80, 127–165.
Klein, E.K., Lavigne, C., Foueillassar, X., Gouyon, P-H., Larédo, C., 2003. Corn pollen dispersal: quasi-mechanistic models and field experiments. Ecol. Monogr. 73, 131–150.
Klein, P., Leitl, B., Schatzmann, M., 2007. Driving physical mechanisms of flow and dispersion in urban canopies. Int. J. Climatol. 27, 1887–1908.
Launiainen, S., Vesala, T., Molder, M., Mammarella, I., Smolander, S., Rannik Ü, Kolari, P., Hari, P., Lindroth, A., Katul, G.G., 2007. Vertical variability and effect of stability on turbulence characteristics down to the floor of a pine forest. Tellus 59B, 919–936.
Mahrt, L., 1998. Stratified atmospheric boundary layers and breakdown of models. Theoret. Comput. Fluid Dynamics 11, 263–279.
Moran, S.M., Pardyjak, E.R., Veranth, J.M., 2013. Understanding the role of grid turbulence in enhancing pm10 deposition: scaling the stokes number with R_λ. Phys. Fluids 25, 103–115.

Novak, M.D., Warland, J.S., Orchansky, A.L., Ketler, R., Green, S., 2000. Wind tunnel and field measurements of turbulent flow in forests. Part I. Uniformly thinned stands. Boundary-Layer Meteorol. 95, 457–495.

Okubo, A., Levin, S.A., 1989. A theoretical framework for data analysis of wind dispersal of seeds and pollen. Ecology 70, 329–338.

Pardyjak, E., Cuerva, A., 2007. Sonic anemometry/thermometry. In: Tropea, C., Foss, JF. (Eds.), Springer Handbook of Experimental Fluid Mechanics. , 1st ed. Springer, New York, pp. 436–446.

Pardyjak, E.R., Speckart, S.O., Yin, F., Veranth, J.M., 2008. Near source deposition of vehicle generated fugitive dust on vegetation and buildings: model development and theory. Atmos. Environ. 42, 6442–6452.

Patton, E.G., Shaw, R.H., Judd, M.J., Raupach, M.R., 1998. Large-eddy simulation of windbreak flow. Boundary-Layer Meteorol. 87, 275–306.

Patton, E.G., Horst, T.W., Sullivan, P.P., Lenschow, D.H., Oncley, S.P., Brown, W.O.J., Burns, S.P., Guenther, A.B., Held, A., Karl, T., Mayor, S.D., Rizzo, L.V., Spuler, S.M., Sun, J., Turnipseed, A.A., Allwine, E.J., Edburg, S.L., Lamb, B.K., Avissar, R., Calhoun, R.J., Kleissl, J., Massman, W.J., Paw, U.K.T., Weil, J.C., 2011. The canopy horizontal array turbulence study. Bull. Am. Meteor. Soc. 92, 593–611.

Peterson, H., Mazzolini, D., O'Neill, S., Lamb, B., 1999. Instantaneous spread of plumes in the surface layer. J. Appl. Meteor. 38, 343–352.

Poggi, D., Porporato, A., Ridolfi, L., Albertson, J.D., Katul, G.G., 2004. The effect of vegetation density on canopy sub-layer turbulence. Boundary-Layer Meteorol. 111, 565–587.

Prussin, A.J., Marr, L.C., Schmale, D.G., Stoll, R., Ross, S.D., 2014. Experimental validation of a long-distance transport model for plant pathogens. Application to *Fusarium graminearum*. Agric. For. Meteorol. 203, 118–130.

Raupach, M.R., Thom, A.S., Edwards, I., 1980. A wind-tunnel study of turbulent flow close to regularly arrayed rough surfaces. Boundary-Layer Meteorol. 18, 373–397.

Raupach, M.R., Woods, N., Dorr, G., Leys, J.F., Cleugh, H.A., 2001. The entrapment of particles by windbreaks. Atmos. Environ. 35, 3373–3383.

Raynor, G.S., Hayes, J.V., Ogden, E.C., 1970. Experimental data on ragweed pollen dispersion and deposition from point and area sources. BNL Rept. 50224 (T-564) Brookhaven National Laboratory, Upton, NY, pp. 33.

Raynor, G.S., Hayes, J.V., Ogden, E.C., 1974. Particulate dispersion into and within a forest. Boundary-Layer Meteorol. 7, 429–456.

Skelsey, P., Holtslag, A.A.M., van der Werf, W., 2008. Development and validation of a quasi-Gaussian plume model for the transport of botanical spores. Agric. For. Meteorol. 148, 1383–1394.

Speckart, S.O., Pardyjak, E.R., 2014. A method for rapidly computing windbreak flow field variables. J. Wind Eng. Ind. Aerodyn. 132, 101–108.

Su, H-B., Schmid, H.P., Vogel, C.S., Curtis, P.S., 2008. Effects of canopy morphology and thermal stability on mean flow and turbulence statistics observed inside a mixed hardwood forest. Agric. For. Meteorol. 148, 862–882.

Su, H-B., Shaw, R.H., Paw, U.K.T., Moeng, C-H., Sullivan, P.P., 1998. Turbulent statistics of neutrally stratified flow within and above a sparse forest from large-eddy simulation and field observations. Boundary-Layer Meteorol. 88, 363–397.

Talaie, A., Shojaie-Saadee, M., Dadashpour, A., Asgari-Sarcheshmeh, M.A., 2011. Fruit quality in five apple cultivars trees trained to intensive training system: Geneva y-trellis. GENETIKA 43, 153–161.

Tarara, J.M., Ferguson, J.C., Hoheisel, G-A., Perez Pe na, J.E., 2005. Asymmetrical canopy architecture due to prevailing wind direction and row orientation creates an imbalance in irradiance at the fruiting zone of grapevines. Agric. For. Meteorol. 135, 144–155.

Taylor, G.I., 1921. Diffusion by continuous movements. Proc. Lond. Math. Soc. 20, 196–211.

Thiessen, L.D., Keune, J.A., Neill, T.M., Turechek, W.W., Grove, G.G., Mahaffee, W.F., 2015. Development of a grower performed inoculum detection assay for management of grape powdery mildew. Plant Pathol., http://dx.doi.org/10.1111/ppa.12421

Thomas, C., Foken, T., 2007. Flux contribution of coherent structures and its implications for the exchange of energy and matter in a tall spruce canopy. Boundary-Layer Meteorol. 123, 317–337.

Turner, D.B., 1994. Workbook of Atmospheric Dispersion Estimates: An Introduction to Dispersion Modeling, 2nd ed. CRC Press, Boca Raton, pp. 192.

USDA National Agricultural Statistics Service (USDA NASS), 2013. Noncitrus fruits and nuts 2012 preliminary summary. http://usda.mannlib.cornell.edu/MannUsda/viewDocumentInfo.do?documentID=1113

Verhoef, A., De Bruin, H.A.R., Van Den Hurk, BJ.J.M., 1997. Some practical notes on the parameter kB^{-1} for sparse vegetation. J. Appl. Meteor. 36, 560–572.

Venkatram, A., Snyder, M.G., Heist, D.K., Perry, S.G., Peterson, W.B., Isakov, V., 2013. Re-formulation of plume spread for near-surface dispersion. Atmos. Environ. 77, 846–855.

Waterhouse, G.M., 1973. Peronosporales. In: Ainsworth, GC., Sparrow, FK., Sussman, AS. (Eds.), The Fungi: An Advanced Treatise. Vol. 45. Academic Press, New York, pp. 165–183.

Weiss, A., Allen Jr., L.H., 1976. Air-flow patterns in vineyard rows. Agric. For. Meteorol. 16, 329–342.

Whiteman, C.D., 2000. Mountain Meteorology: Fundamentals and Applications. Oxford University Press, New York/Oxford, pp. 376.

Yang, B., Morse, A.P., Shaw, R.H., Paw, U.K.T., 2006. Large-eddy simulation of turbulent flow across a forest edge. Part II: Momentum and turbulent kinetic energy budgets. Boundary-Layer Meteorol. 121, 433–457.

Yee, E., Biltoft, C.A., 2004. Concentration fluctuation measurements in a plume dispersing through a regular array of obstacles. Boundary-Layer Meteorol. 111, 363–415.

Yee, E., Gailis, R.M., Hill, A., Hilderman, T., Kiel, D., 2006. Comparison of wind-tunnel and water-channel simulations of plume dispersion through a large array of obstacles with a scaled field experiment. Boundary-Layer Meteorol. 121, 389–432.

Yue, W., Parlange, M.B., Meneveau, C., Zhu, W., van Hout, R., Katz, J., 2007. Large-eddy simulation of plant canopy flows using plant-scale representation. Boundary-Layer Meteorol. 124, 183–203.

CHAPTER 4

HEAVY PARTICLE TRANSPORT IN A TRELLISED AGRICULTURAL CANOPY DURING NON-ROW-ALIGNED WINDS

Agricultural systems are exposed to and influenced by particles of many types, the concentrations of which are typically highest in the regions immediately surrounding their sources. In trellised canopies specifically, the unique architecture of the canopy directly affects the shape of particulate plumes and tends to alter their transport patterns in the near-source region. To investigate the behavior of particle plumes near their sources in a trellised canopy, a set of particle release experiments was conducted during a field campaign in an Oregon vineyard in 2013. Specifically, plumes of inert fluorescent microspheres (10 to 45 μm diameter) were released into the canopy during periods when the mean wind direction was significantly different from the vine row direction. Plume concentrations were collected at over 100 separate locations in a three-dimensional space within 10 canopy heights downwind of the source during each release period. These plumes proved to be more complex than those released during periods of row-aligned winds. A novel analysis approach using the superposition of two Gaussian plume equations was developed to quantitatively assess the plumes' shape behavior. It was determined that many basic plume shape parameters, as determined by integrating the superposed Gaussian equation that was fit to the field concentrations, varied significantly as a function of the mean wind direction. As the wind direction changed from roughly row-diagonal to directly row-normal, the rate at which the spanwise plume width increased with downwind distance increased by a factor two. Similarly, the rate at which the plume height increased with downwind distance was higher for row-perpendicular plumes than for

row-diagonal plumes. It was also determined that the row-diagonal plumes exhibited a much higher spanwise skewness than did the row-normal plumes, but that for all of the plumes, the skewnesses tended towards zero (symmetric) with increasing downwind distance.

4.1 Introduction

Particle transport in canopies has received considerable research interest in recent years (e.g., Venkatram et al., 2004; Pardyjak et al., 2008; Pan et al., 2014). Most canopy-based particle transport studies have been done in one of two types of canopies. The first of these is urban and quasi-urban canopies, typified by buildings of various heights and spacings and by inhomogeneities like deep street canyons. The other is vegetative canopies, the majority of which have been relatively dense and essentially horizontally homogeneous. In both of these canopy types, dispersion patterns have been studied over a rather large range of length scales. The urban-based studies have typically focused on dispersion patterns at length scales much larger than the local building and street scales (e.g., Hanna and Baja, 2009). Dispersion patterns on very local scales are often very irregular and more difficult to study due to the complexity of the local building and street effects. As a result, fewer studies have focused on these areas (e.g., Allwine et al., 2002; Belcher, 2005). Similarly, dispersion studies in agricultural or natural vegetative canopies have usually either focused on sub-canopy dispersion in relatively dense, homogenous canopies (e.g., Aylor and Ferrandino, 1989; Gleicher et al., 2014) or on transport at scales much larger than the field scale, wherein in-canopy physics and near-source patterns were of lesser concern (e.g., Brown and Hovmoller, 2002; Spijkerboer et al., 2002; Prussin et al., 2015). More complex canopies, with local inhomogeneities, large gaps between plants, or multidimensional trellising systems, have received little research attention by comparison.

High-value perennial crops, like grapes, almonds, and hops, are typically grown in complex canopies which often have large gaps between plants (e.g., vineyards). Additionally, many perennial crop growers are moving toward the use of trellising systems that structure the canopies for optimal growth and ease of harvest (Robinson

et al., 1991; Lauri, 2009). Trellising creates a uniquely structured and heterogenous architecture unlike either the urban canopies or the homogenous canopies previously studied. Management of these canopies requires understanding the transport of particulates into and within the canopies and the flow physics that dictate that transport (Mahaffee et al., 2011). From an ecological standpoint, because plume concentrations are typically highest near their source and are therefore likely to have the greatest impact in that region, resolving their behavior within the canopy and near the source is of great interest (Mahaffee et al., 2014). The understanding of particle transport (e.g., fungal spores, pesticide sprays, pollen) near sources within these canopies is crucial to their prosperity (Mahaffee and Stoll, 2016).

In order to investigate particle plume behavior in a trellised canopy, a series of field campaigns has been conducted in a commercial vineyard in Oregon in conjunction with the United States Department of Agriculture (USDA) Agricultural Research Service (ARS). Findings from the 2011 campaign in which we examined particle plumes released during periods when the mean winds were nearly aligned with the vine-row direction were published as Miller et al. (2015). The work here is focused on plumes that were released during periods when the mean winds were in a significantly different direction than the vine rows. For that, we only examined plumes where the mean wind direction well above the canopy was $> 40^\circ$ away from parallel to the vine row direction. These plumes were collected in a vineyard near Monmouth, Oregon in 2013 while meteorological data were collected using an instrumented tower located in the same vineyard block (Section 4.2). Extensive analysis of the meteorological data, including mean statistics, turbulent fluxes, and energy spectra, was reported in Miller et al. (2016). A novel approach of using the superposition of two Gaussian plume equations was used to estimate simple plume shape parameters in an effort to understand the signature of the vineyard architecture on the behavior of the plume (Section 4.3).

4.2 Field Campaign

The field campaign was performed in a vineyard near Monmouth, Oregon in 2013 and was described in detail in Miller et al. (2016). A similar study was performed in

the same vineyard in 2011 and microsphere plumes from that campaign—which were collected at times when the winds were blowing nearly parallel to the vine rows—were reported in Miller et al. (2015). The specifics of the vineyard architecture as well as extensive statistics on the velocity field, momentum fluxes, turbulent kinetic energy, and turbulent spectra as collected in the vineyard during the 2013 campaign were explained in Miller et al. (2016). Here, it is sufficient to say that the vineyard canopy was 2.15 m tall (h) with north-to-south oriented rows spaced at 2.5 m on center (r_s), and that a meteorological tower was placed in the center of an aisle near the center of relatively flat vineyard block ($\approx 44^\circ\ 49'\ 27.0''$ N, $123^\circ\ 14'\ 17.0''$ W). The tower had six Campbell Scientific CSAT3 sonic anemometers at heights of z = 10.1 m, 5.0 m, 3.0 m, 2.0 m, 1.4 m, and 0.7 m. Tri-directional wind data, defined as $u_i = \{u_\perp, v_\parallel, w\}$, where $u_\perp$ and $v_\parallel$ were velocity components oriented perpendicular to (x') and parallel to (y') the vine row direction, respectively, were logged throughout the weeks-long campaign. Other meteorological variables that were relevant to the field campaign—like fine-wire thermocouple temperatures (T)—were also logged for use in this and other studies (Bailey et al., 2016).

During the 2013 campaign, microsphere plumes were released during periods when the above-canopy mean wind direction ($\overline{wd}$) ranged from row-parallel to row-perpendicular. The overbar represents a mean taken over the time window of the individual plume release event. Herein, the focus is on the plumes released when $\overline{wd}$ was significantly different from the vine row direction.

4.2.1 Dispersion Experiments

The series of microsphere release events were conducted using three separate colors of polyethylene microspheres. These microspheres were used and discussed in Miller et al. (2015), but different lots were used here. The three colors were violet (UVPMS-BV-1.00, Cospheric LLC), orange (UVPMS-BO-1.00, Cospheric LLC), and yellow/green (UVPMS-BY2-1.00, Cospheric LLC), each with > 90% of spheres within the diameter range of 10 to 45 μm (Fig. 4.1). The violet, orange, and yellow/green microspheres had average diameters of 30.9, 34.1, and 32.8 μm, respectively. When the average diameter for each color was determined on a per-mass basis, the average

diameters were 33.1, 35.5, and 35.4 μm, respectively. These diameters and ranges corresponded well with the average hydraulic diameter of the spores of multiple common fungal pathogens found in vineyards. This includes *Botrytis cinerea* (diameters of 8–12 μm, Jarvis, 1977), *Erysiphe necator* (diameters of 20–36 μm, Braun, 1995), and *Plasmopara viticola* (diameters of 30–50 μm, Waterhouse, 1973). The microspheres' density was 1.005 g/cm^3, similar to many fungal spores, including those relevant for vineyards (Gregory, 1973).

The microspheres were suspended in a 0.05% v/v Tween 20 solution at a concentration of 0.05 g/ml which was then emitted into the canopy using ultrasonic atomizer nozzles (Sonaer Inc.). The nozzles allow for a solution to be pumped through and atomized at the nozzle tip. Three nozzles were mounted into the canopy at separate individual heights (H_r) with the nozzle tip pointed downward, and each was connected to a syringe filled with one color of microspheres in liquid suspension. Before each release event, the syringes were filled with the solution and loaded into a syringe pump (Model 22, Harvard Apparatus). During each event, the syringe pump was used to pump the microsphere solution to the nozzles at a constant rate throughout the length of the event. The nozzles were tuned such that as the solution was pumped through, it was visibly vaporized at the nozzle's tip, resulting in the microspheres being carried away by the wind (Fig. 4.2). During each release event, the violet, orange, and yellow/green microspheres were released from heights of H_r = 1.51 m, H_r = 1.16 m, and H_r = 0.81 m, respectively.

The microsphere concentrations were sampled using the rotating arm impaction traps described and shown in Miller et al. (2015). The impaction trap cross-arms were replaced with newer versions that spun the rotating substrates at a radius of 4.3 cm. Also, the heights of the individual impaction traps within the canopy were altered somewhat to values of z = 1.9 m, 1.4 m, 0.9 m, and 0.2 m (from 1.6 m, 1.2 m, 0.8 m, and 0.4 m used in 2011). These small changes were based primarily on lessons learned from the 2011 campaign, e.g., a desire for concentration data nearer to the ground. An array of 23 aluminum towers was positioned downwind, east and northeast, of the release location. This resulted in each plume being sampled at 115 separate locations at downwind distances between 1.5 and 21 m from the release nozzles (Fig. 4.3).

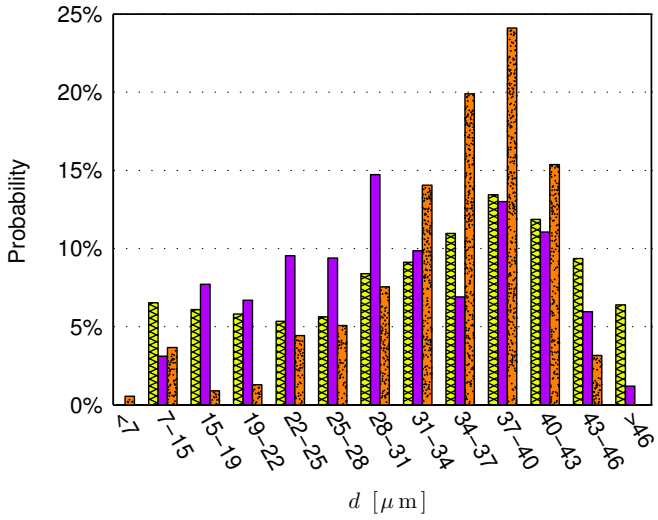

Figure 4.1: Histogram of the microsphere diameters. The yellow hatched bars, the solid violet bars, and the speckled orange bars represent the yellow, violet, and orange microspheres, respectively.

Figure 4.2: One of the ultrasonic nozzles through which the microsphere solutions were pumped to be released into the canopy, and the syringe pump loaded with syringes filled with the three colors of suspended microspheres. The nozzle was releasing microspheres when the photo was taken, as indicated by the fine mist exiting the bottom right corner of the image.

This was even more locations than were used in Miller et al. (2015) and provided an unmatched quantity and resolution of near-source plume concentrations among similar experiments. The asymmetric layout of the 23 towers was designed based on expected mean wind directions from the southwest and based on prior experience with attempting to capture plumes during periods with those southwest winds in 2011. The ultrasonic nozzles, the impaction traps, and the syringe pump were all controlled using a wireless mesh network using Xbee modules (Digi International Inc.), thus allowing for operation from outside the vineyard block.

A total of 12 release events were conducted when $|\delta| > 40°$, where δ was the difference between $\overline{wd}$ and the vine-row direction (Miller et al., 2015, 2016). Each of the events was conducted in the afternoon hours when fungal spores are typically transported in the field (Pady and Subbayya, 1970). This resulted in each of the events having an atmospheric stability (ζ) that was slightly unstable, where $\zeta = h/L$ and L was the Obukhov length defined at the canopy top (Table 4.1). The Obukhov length was defined as $L = -u_{*,h}^3 \overline{T_o} / (\kappa g (\overline{w'T'})_h)$, where κ is the von Kármán constant (taken as 0.4), g is gravitational acceleration, $\overline{T_o}$ is the temperature at the top of the canopy, $\overline{w'T'}$ was the absolute vertical heat flux, primes represent deviations from the means taken over the time period that each plume was released, the subscript h denotes values determined at the canopy top, and the friction velocity was defined as $u_* = \left[\overline{u'_\perp w'}^2 + \overline{v'_\parallel w'}^2\right]^{1/4}$.

The microsphere concentration at each impaction trap location was determined by examining a 10–20 mm long section at the center of the length of each rod from each impaction trap under a fluorescence stereo microscope. This was done while using specific excitation lighting and lens filters to allow each color of spheres to be counted individually. The number of spheres was then converted into a scaled concentration (Π) by multiplying by the average mass per sphere and by the canopy-top velocity ($\overline{u_h}$) and by dividing by the swept volume of the examined portion of the rods from each impaction trap and by the plume source strength (Miller et al., 2015).

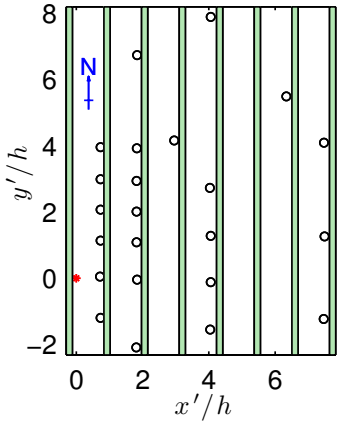

Figure 4.3: The layout of the impaction trap towers downwind of the source nozzles. Each *black circle* represents the location of the vertical column of five impaction traps, the *red star* represents the location of the three vertically aligned nozzles, and the *green patches* represent the vine rows.

Table 4.1: Table of the meteorological conditions determined during each release event, including the wind velocity at the z = 10 m anemometer ($\overline{u}$), the canopy-top velocity ($\overline{u_h}$), and the canopy-top friction velocity ($u_{*,h}$).

Event	Time (PDT)	Mass [g]	$\lvert\delta\rvert$	$\overline{u}$ [m/s]	$\overline{u_h}$ [m/s]	$u_{*,h}$ [m/s]	ζ
1	14:29	0.50	40.1°	2.69	0.87	0.33	-0.073
2	16:35	0.58	41.7°	3.93	1.15	0.48	-0.044
3	15:31	0.50	42.2°	2.74	0.83	0.33	-0.092
4	18:47	0.50	42.5°	3.18	0.89	0.38	-0.018
5	17:02	0.50	44.7°	4.93	1.47	0.52	-0.023
6	17:41	0.48	49.5°	2.77	0.78	0.37	-0.023
7	15:29	0.50	55.1°	2.91	0.73	0.38	-0.102
8	16:15	0.50	55.3°	3.79	1.15	0.48	-0.035
9	14:28	0.50	58.1°	3.20	0.96	0.38	-0.064
10	15:35	0.50	62.4°	3.04	0.88	0.39	-0.036
11	17:01	0.50	84.2°	2.62	0.70	0.31	-0.022
12	16:18	0.50	89.1°	2.14	0.63	0.28	-0.092

4.3 Dispersion Experiment Results

The concentration data from each of the 115 impaction traps locations for each of the 36 microsphere plumes (12 events with three release heights) provided a relatively high-resolution three-dimensional (3D) representation of the near-source plume shape. Most previous dispersion studies in plant canopies sampled concentrations at considerably fewer locations and often only along one axis or in one plane (e.g., Aylor and Ferrandino, 1989; Chamecki et al., 2012; Prussin et al., 2015). Some exceptions to this have used gridded 3D sampling (e.g., Raynor et al., 1974; Pan et al., 2014), but we are unaware of any studies other than our own with as many points as this in the near source region (Miller et al., 2015). The concentration data demonstrated that the plumes had complex 3D shapes, that they were not symmetric around any identifiable axis, and that they varied in shape as a function of δ (e.g., Fig. 4.4).

Before moving into more complex 3D shape analysis, simple observations of the plume behavior were made. The location of the peak concentration (Π_{max}) in each north-to-south oriented row of trap towers and the rate of decay of those values was determined. Examining Π_{max} in each row to the east of the release device (i.e., positive x') indicated that regardless of the trap height or location, the row-orthogonal decay rate decreased with x' (Fig. 4.5). The centerline decay rates of Gaussian-type plumes has been investigated extensively in a variety of environments and has been shown to follow $\Pi_{max} = a\ x^{-b}$. This is a simplification of the Gaussian plume equation, resulting in b usually having a value of ≈ 2 (e.g., Venkatram et al., 2004; Hanna et al., 2007). Interestingly, when Π_{max} was studied versus the row-orthogonal distance, x', instead of along the perceived plume centerline, b was found to be 1.89, regardless of δ. The locations at which Π_{max} occurred in each row were typically at the impaction trap tower location which was closest to where $\overline{wd}$ vector suggested that the max should have been, i.e., if the plume centerline could be assumed to follow $\overline{wd}$. When the max concentration was studied versus the x location of the impaction trap tower (where x was the downstream distance along the vector defined by $\overline{wd}$) at which Π_{max} was found, the same fit was found to have $b = 1.66$. This is closer to the value of $b = 1.5$ reported by Hanna et al. (2003) for the centerline decay rate nearer to the source.

Additionally, the height at which the peak was detected in each row showed

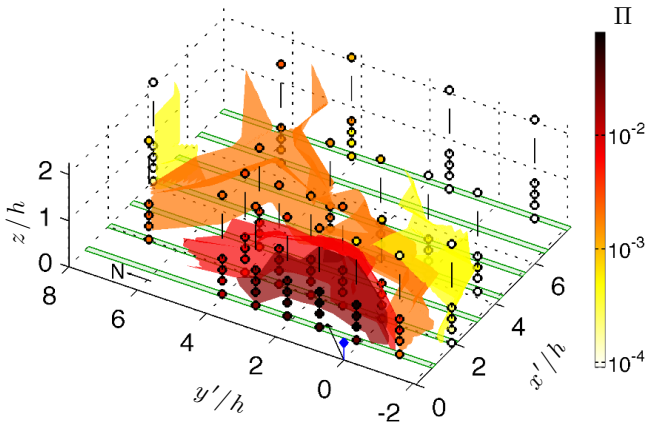

Figure 4.4: Concentration data for the violet microsphere plume (H_r = 1.51 m) from release event 5. Each of the 115 impaction traps are depicted in their respective 3D locations as *circles* colored by their respective values of Π. Isosurfaces of constant Π values of Π = $\{0.02, 0.007, 0.002, 0.0005\}$ m^{-2} were determined via a real-space, tri-linear interpolation of the impaction trap data. The *blue diamond* represents the source location while the *green patches* represent the footprints of the individual vine rows. The *black arrow* originating at the origin depicts $\overline{wd}$ which was from 44.7° west of south, i.e., from southwest to northeast.

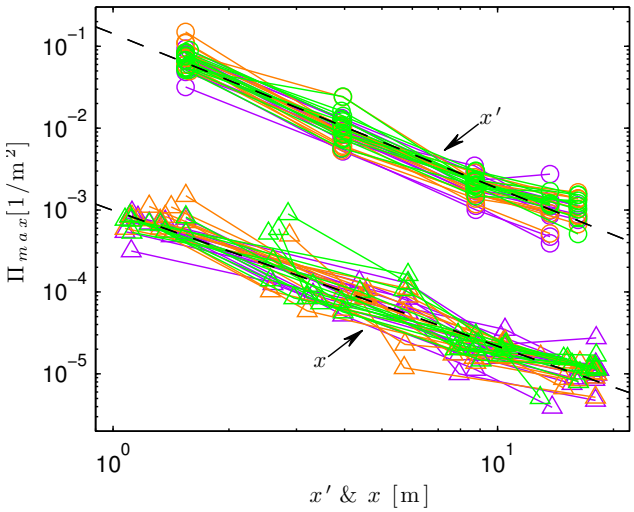

Figure 4.5: The maximum Π value in each north-to-south row of impaction trap towers in aisles east of the release location. The upper cluster of lines depict the Π values plotted versus x' while the lower cluster of lines depict the same Π values divided by 100 and plotted versus x, where x is the distance along the vector defined by $\overline{wd}$. The *violet*, *orange*, and *green* lines are for the violet, orange, and yellow/green microsphere plumes, respectively. The *dashed black* lines depict exponential fits with B = 1.89 and B = 1.66 for the groups plotted versus x' and x, respectively.

considerable correlation to the release height. For example, in the third aisle east of the aisle of the source, Π_{max} was found to occur at the impaction trap nearest to h in eight of the 12 plumes with H_r = 1.51 m. That height was actually > H_r for those plumes, meaning much of the plume had moved up in the canopy. For the remaining four plumes, Π_{max} was at either the impaction trap just lower than H_r (three out of 12) or all the way up at the z = 4.85 m impaction trap (one out of 12). For the yellow/green microsphere plumes—released near the canopy bottom—the max value in the third aisle east of the source was found to be at the impaction trap at z = 0.22 m in five of the 12 cases, z = 1.88 m in five of the 12 cases, and at a height between those for the remaining two cases.

Even with 115 sample locations within the field, the gaps between the locations were still typically larger than h and larger than would be desired in order to make reliable estimations of plume shape parameters—like the width of the plume (σ_y)—by direct calculation from their statistical definitions. Tri-linear interpolation of the data allowed for such parameters to be identified directly by using their definitions in any arbitrary coordinates system, e.g., the plume width could be determined along any axis through the domain by use of a sample standard deviation calculation. Such an approach is dubious, however, because it assumes linear concentration variations between sample locations, including those that are spaced relatively far apart, like those farther from the source. This assumption is bad for plume concentration data, which is known to not vary linearly in space, and also does not ensure that mass is conserved across space. Therefore, if plume shape parameters are desired, a more informed and accurate interpolant like that used in Miller et al. (2015) would be necessary.

4.3.1 Plume Analysis

In examining the momentum and turbulence fields within the vineyard canopy, it was determined in Miller et al. (2016) that a canopy aligned coordinate system provided for simpler and more easily understood elucidation of the data. In this way, contributions of the along-row and row-orthogonal fluxes could be examined as functions of δ. Because these fluxes were directly responsible for the plume shape

behavior in the canopy, it was assumed that a similarly defined coordinate system could be used to define the plume shapes and that the behavior of the plume in each of the axes of this system could be related to those row-oriented fluxes. To that end, an equation was developed that could be fit to the concentration data and then be used to determine the specifics of the plume shape and behavior. This procedure was broadly similar to what was done in Miller et al. (2015) and although the skewed-Gaussian plume equation that was used therein was tried for use here, it did not provide a satisfactory quality of fit for most of the plumes and thus a new equation was developed. The new equation consisted of the superposition of two Gaussian plume distributions (SuperGauss), with one oriented perpendicular to and one oriented parallel to the vine rows. The SuperGauss was defined as,

$$\begin{aligned}\Pi = P\Bigg[&\frac{A_\perp}{2\pi\sigma_{y\perp}\sigma_{z\perp}}\exp\left(\frac{-(y_\perp-\mu_{y\perp})^2}{2\sigma_{y\perp}^2}\right)\\&\times\left(\exp\left(\frac{-(z-H_e)^2}{2\sigma_{z\perp}^2}\right)+\exp\left(\frac{-(z+H_e)^2}{2\sigma_{z\perp}^2}\right)\right)\Bigg]\\&+(1-P)\Bigg[\frac{A_\parallel}{2\pi\sigma_{y\parallel}\sigma_{z\parallel}}\exp\left(\frac{-(y_\parallel-\mu_{y\parallel})^2}{2\sigma_{y\parallel}^2}\right)\\&\times\left(\exp\left(\frac{-(z-H_e)^2}{2\sigma_{z\parallel}^2}\right)+\exp\left(\frac{-(z+H_e)^2}{2\sigma_{z\parallel}^2}\right)\right)\Bigg],\end{aligned} \tag{4.1}$$

where the A's were magnitude adjustments which account for mass removal (Miller et al., 2015), μ_y's were spanwise offsets of the distributions' means from the equations' axes, σ_y's and σ_z's were standard deviations of the plume in the spanwise and vertical direction, respectively, and there were separate values of each for the perpendicular and parallel portions of SuperGauss. The $\perp$ and $\parallel$ subscripts denote variables taken with respect to axes oriented in those respective directions, H_e was the effective plume centerline height along each portions' axis, and P was the weighting factor for the two distributions and always had a value between zero and one. The use of P in this way ensured that Equation 4.1 was a valid solution to the advection-diffusion equation if it were defined in the same coordinate system.

Because all 115 values of Π were used in the fit of each plume, and because each impaction trap was at its own downstream and spanwise distance in each of the two

portions' respective coordinate systems, functional forms for the individual shape parameters had to be assumed *a priori*. For the row-perpendicular portion of the SuperGauss, the streamwise and spanwise coordinates were x' and y', respectively, while the row-parallel oriented portion had streamwise and spanwise coordinates of y' and x', respectively (Fig. 4.3). It was therefore assumed that,

$$A_\perp = \exp(-m_{A\perp}x') \quad \text{and} \quad A_\parallel = \exp(-m_{A\parallel}y'), \tag{4.2}$$

$$\sigma_{y\perp}^2 = \sigma_{y\perp,0}^2 + m_{\sigma_{y\perp}}^2 x'^2 \quad \text{and} \quad \sigma_{y\parallel}^2 = \sigma_{y\parallel,0}^2 + m_{\sigma_{y\parallel}}^2 y'^2, \tag{4.3}$$

$$\sigma_{z\perp}^2 = \sigma_{z\perp,0}^2 + m_{\sigma_{z\perp}}^2 x'^2 \quad \text{and} \quad \sigma_{z\parallel}^2 = \sigma_{z\parallel,0}^2 + m_{\sigma_{z\parallel}}^2 y'^2, \tag{4.4}$$

and

$$\mu_{y\perp} = m_{\mu_{y\perp}} x' \quad \text{and} \quad \mu_{y\parallel} = m_{\mu_{y\parallel}} y', \tag{4.5}$$

for the two portions of the SuperGauss, respectively, as identified by the subscripts $\parallel$ and $\perp$. In this equation set, $\sigma_{y,0}$ and $\sigma_{z,0}$ were the effective width and height of the plume at the source location, and $m_A, m_{\sigma_y}, m_{\sigma_z}$, and m_{μ_y} were the rates of change of each of their respective parameters with downwind distance. $m_{\sigma_y}, m_{\sigma_z}$, and m_{μ_y} were nondimensional while m_A had units of m^{-1}. These relatively simple forms were chosen based on previous research into each of the parameters in other canopies (e.g., Aylor and Sutton, 1992; Huq and Franzese, 2013; Miller et al., 2015) and to provide a straightforward closure to the equation set. For the spanwise offsets, m_{μ_y} was defined such that it was positive when the centerline of each SuperGauss portion was offset into the quadrant in which most of the impaction trap towers were positioned. This meant that for the perpendicular portion, a positive μ_y (and m_{μ_y}) represented an offset to the left (north) of the row-perpendicular axis and for the parallel portion, it represented an offset to the right (west) of the row-parallel axis. The effective plume centerline height was assumed to follow,

$$H_e = H_r - (dH + m_H x') \quad \text{and} \quad H_e = H_r - (dH + m_H y'), \tag{4.6}$$

where dH was an initial fall distance at the source, analogous to an initial plume rise seen in buoyant plume problems (Stockie, 2011), and m_H was the rate of fall with downwind distance, typically caused by gravitational settling. The same values

for dH and m_H were used for both portions of the SuperGauss as neither initial fall nor settling were believed to be directionally dependent. Therefore, H_e behaved identically along each portions centerline. Collectively these functions, along with P, resulted in a total of 15 parameters that were simultaneously optimized to the 115 values of Π for each plume. This allowed for high-quality fits and for a wide range of arbitrary plume shapes to be generated (Fig. 4.6).

The equation set (Equations 4.1–4.6) was fit to the field data using a multivariable nonlinear least-squared-error optimization that employed the trust-region approach in MATLAB (The MathWorks Inc., version R2010a). The convergence criteria were developed such that error was minimized in real and log space simultaneously. Optimization in real space is biased toward improved fits near the source and poorer fits farther from the source, and optimizations in log space tend to considerably over- or under-estimate the concentrations near the source. Using an optimization in both real and log space provided for better overall fits to the whole plume (Table 4.2). The plume of violet microspheres from event 12 was only optimized in real space because a satisfactory convergence could never be achieved with the dual optimization. This may have been caused by somewhat noisy concentration data at the impaction traps farthest from the source causing the log-space optimization to fail. An optimization in real space only was no different than the technique used in Miller et al. (2015) and was therefore still considered to be effective.

The quality of the fit of the SuperGauss, when observed in real space, tended to get worse for lower release heights. In contrast, the log-space r^2 values stayed nearly constant with H_r. Because the real-space fit was biased toward the near-source concentration behavior, this reduction in the real-space fit quality was indicative of the SuperGauss being poorer at approximating near-source behavior for plumes with lower H_r's. Similarly, because the log-space fits were unchanged with H_r, the SuperGuass approximated behaviors at impaction traps farther from the source equally well for each of the release heights. The poorer fit near the source for lower release heights may have been caused by the use of $\overline{u_h}$ in the normalization of the Π values. If a different velocity scale were used near the canopy bottom, perhaps one that could account for the complexity of the understory flow physics, the quality of

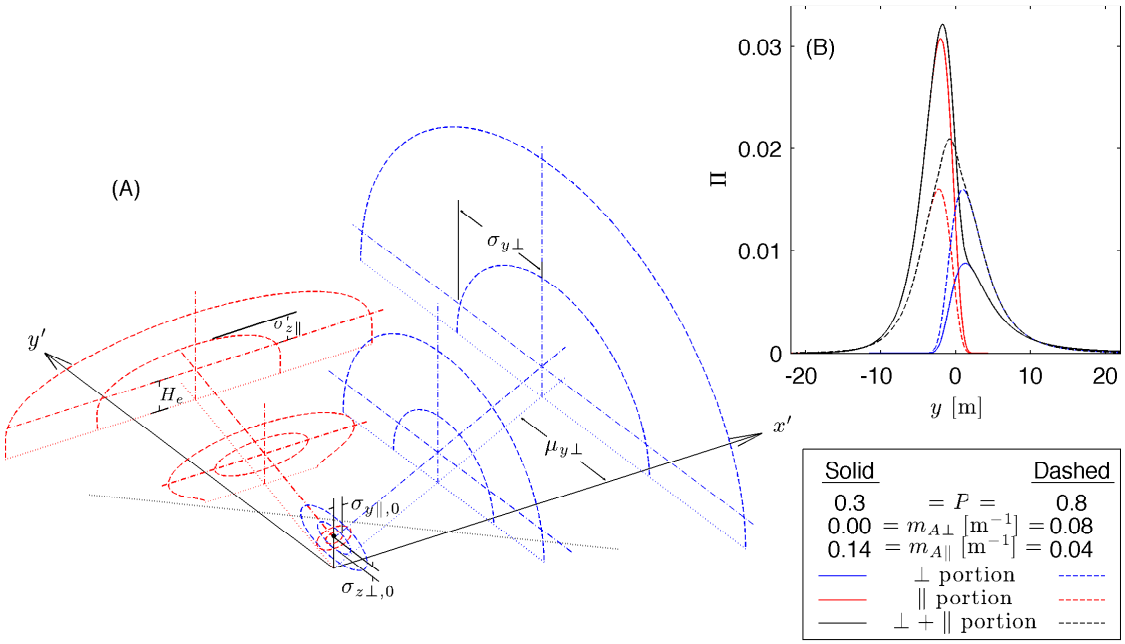

Figure 4.6: A schematic of the two portions of the SuperGauss with a subset of the equation's parameters labeled for clarity (A) as well as spanwise profiles of Π taken from the demonstrated equation used in the schematic (B). In A, the *dot-dashed* lines show the centerlines and planar axes at downaxis distances of 8 and 19 m for each of the portions, the *dotted* lines show those same axes projected onto the ground, and the *dashed* lines are contour isolines at one and two standard deviations from the centerlines in each dimension. The spanwise profiles in B were taken at a height of H_r and about the mean wind direction vector, which was assumed to be at 45° from parallel for this demonstration. They were taken along a line at 6 m downwind of the source as depicted by the black *dotted* line. The parameter values used in A were used to determine the profiles in B along with the coefficients shown in the legend. Two different combinations of the values of P and the streamwise decay rates ($m_{A\perp}$ and $m_{A\parallel}$) were used to demonstrate typical shapes that can be attained by the summation of the two Gaussian equations. *Blue* lines throughout are for the perpendicular portion of the equation and *red* lines are for the parallel portion.

Table 4.2: The real- (rs) and log-space (ls) based quality-of-fit measures for the fit of the SuperGauss to each of the plumes.

	Violet (H_r = 1.51 m)		Orange (H_r = 1.16 m)		Yellow/green (H_r = 0.81 m)	
Event	r^2 (rs)	r^2 (ls)	r^2 (rs)	r^2 (ls)	r^2 (rs)	r^2 (ls)
1	0.93	0.90	0.93	0.90	0.80	0.91
2	0.93	0.89	0.91	0.85	0.93	0.87
3	0.95	0.86	0.92	0.86	0.93	0.85
4	0.94	0.86	0.93	0.87	0.92	0.88
5	0.94	0.92	0.97	0.92	0.91	0.90
6	0.93	0.83	0.90	0.84	0.81	0.80
7	0.95	0.87	0.90	0.85	0.89	0.86
8	0.96	0.89	0.87	0.90	0.93	0.92
9	0.92	0.90	0.88	0.86	0.87	0.89
10	0.92	0.88	0.88	0.86	0.88	0.90
11	0.93	0.85	0.83	0.76	0.68	0.84
12	0.98*	0.44*	0.71	0.87	0.83	0.88

* Optimized in real space only.

the fit near the source may have been improved. It is believed that flow accelerates through the vine understory—as it does in other canopies with open understories (e.g., Su et al., 2008)—but with the exception of Bailey and Stoll (2013), the actual affects in the vineyard have not been extensively investigated.

Both the perpendicular and parallel portions of the SuperGauss were studied individually in addition to looking at the composite plume shape created by the superposition. Plume shape parameters of the composite plume equation were determined by integration of the SuperGauss using the direction defined by $\overline{wd}$ as the assumed centerline direction of the plume. Values for σ_y, σ_z, μ_y, the spanwise skewness γ_y, the spanwise kurtosis (K_y), and the spanwise location of the maximum Π ($\mu_{y,max}$) were determined at four different x distances. The four distances, x = 3, 5.5, 8, and 16 m, were chosen to match the distances used in Miller et al. (2015). The spanwise moments were defined as,

$$\mu_y = \frac{\int_{-\infty}^{\infty} y\Pi(y)dy}{\int_{-\infty}^{\infty} \Pi(y)dy}, \tag{4.7}$$

$$\sigma_y^2 = \frac{\int_{-\infty}^{\infty} (y-\mu_y)^2\Pi(y)dy}{\int_{-\infty}^{\infty} \Pi(y)dy}, \tag{4.8}$$

and,

$$M_n = \frac{\int_{-\infty}^{\infty} (y-\mu_y)^n\Pi(y)dy}{\sigma_y^n \int_{-\infty}^{\infty} \Pi(y)dy}, \tag{4.9}$$

where M_n are higher order moments and n is an integer. For γ_y and K_y, n = 3 and n = 4, respectively. The integral divisor in Equations 4.7 through 4.9 was necessary because the spanwise distributions of Π did not always integrate to unity. These definitions are mathematically consistent with the same variables used in Miller et al. (2015) although those were defined based on identities of the Skew-Normal Distribution Function (SNDF). Finally, the values of σ_y and σ_z determined for the composite plume were fit with equivalent forms of Equations 4.3 and 4.4 in order to determine the values for σ_{y0}, σ_{z0}, m_{σ_y}, and m_{σ_z} for the whole plume.

4.3.2 Plume Shape Results

The values of the streamwise decay rate slopes (m_A's) for the perpendicular and parallel portions of the SuperGauss did not exhibit any trend with either H_r or δ and had values of $m_{A_\perp}$ = 0.05 m^{-1} with a standard deviation of 0.03 m^{-1} and $m_{A_\parallel}$ = 0.21 m^{-1} with a standard deviation of 0.09 m^{-1}. The perpendicular portion typically had larger values of σ_y than did the parallel portion. This was caused by $\sigma_{y0,\perp}$ being larger than $\sigma_{y0,\parallel}$ (1.54 m and 0.91 m on average, respectively) and because its rate of increase with downaxis distance was also larger (i.e., $m_{\sigma_{y,\perp}}$ = 1.00 while $m_{\sigma_{y,\parallel}}$ = 0.15 on average). The values of $\sigma_{y0,\parallel}$ found here were very nearly constant over all of the plumes regardless of H_r or δ, and were very near the value reported for the same variable in Miller et al. (2015).

Values of σ_{z0} for the perpendicular and parallel portions were usually small, even having values of zero in the perpendicular portion for many of the plumes. There was a considerable spread in the values, however, especially for the plumes with lower values of $|\delta|$. The parallel portion had larger values of σ_{z0} than did the perpendicular portion on average (0.73 m versus 0.49 m), but σ_z tended to grow more slowly in that portion than in the perpendicular portion ($m_{\sigma_{z,\parallel}}$ = 0.30 versus $m_{\sigma_{z,\perp}}$ = 0.90 on average).

For all but 11 of the plumes, dH was zero. Nine of the 11 for which it was non-zero were plumes released at H_r = 1.51 m. They had an average of dH = 0.11 m and a max of dH = 0.34 m. Similarly, only seven of the plumes had a non-zero value of m_H and although it had been expected that this value would typically be similar to the terminal fall velocity of the microspheres, it is not unbelievable that the plethora of other factors influencing the microsphere trajectories washed out any terminal fall velocity effects. It should also be noted that the values of dH and m_H were constrained within the multivariable optimization such that they were not allowed to be negative, a result that would have suggested that the plume centerline started at a height above H_r and/or was able to rise higher than H_r with downwind distance.

Unsurprisingly, m_{μ_y} for the perpendicular portion tended to decrease with increasing $|\delta|$. It ranged from values as high as ≈ 2 for some of the plumes with $\delta < 40°$ (i.e., for each row-perpendicular meter downaxis from the source, the centerline of

the perpendicular portion was offset two meters from the axis) to being zero for all of the plumes with $\delta > 80°$. Perhaps less intuitive was that $m_{\mu_{y,\parallel}}$ also showed a slight decrease with $|\delta|$. This suggested that as δ increased, the amount that the parallel portion was offset from the row-parallel axis decreased. All but five of the plumes had values of $0.04 < m_{\mu_{y,\parallel}} < 0.28$. Two of the remaining five were plumes with lower values of δ and had $m_{\mu_{y,\parallel}} \approx 0.5$ while the other three all had $\delta > 80°$ and had $m_{\mu_{y,\parallel}} \approx 0$. The decay of $m_{\mu_{y,\parallel}}$ to near zero as δ increased to 90° was the opposite of what would have been expected (large offsets of the parallel portion for plumes with $\overline{wd}$ most different from row-parallel) but may be partially explained by the behavior of P.

The weighting parameter, P, showed an increase in the importance of the perpendicular portion as $|\delta|$ increased (Fig. 4.7). As $\overline{wd}$ moved from row-diagonal to row-normal, the portion of the SuperGauss that was oriented perpendicularly to the vine row direction was responsible for more of the released mass—a result that was expected by design of the equation. Additionally, P was typically largest for the plumes with the lowest H_r. In 10 of the 12 events, the plumes released at the bottom of the canopy had higher P values than those released in the upper canopy.

More important than the behavior of the individual portions of the SuperGauss was the behavior of the plume as a whole, as identified by its integrated shape parameters. The behavior of σ_{y0} and m_{σ_y} was determined by fitting Equation 4.3 to the four values for σ_y determined at the four x distances. Both parameters were found to increase as a function of $|\delta|$ (Fig. 4.8). This result was consistent across the events studied here and proved to also be consistent with values determined from the row-parallel plumes published in Miller et al. (2015). The increase of σ_{y0} and m_{σ_y} with $|\delta|$ was likely caused by the variation of the plumes' effective advection velocity (u_a) and the directional asymmetry of the flux tensor reported in Miller et al. (2016). As $\overline{wd}$ turned from row-parallel to row-perpendicular, the streamwise velocity at the z = 1.3 m anemometer—assumed to roughly represent u_a—decreased considerably. Additionally, the row-parallel oriented mixing ($\sigma_{v_\parallel}$) was greater during periods of perpendicular winds than was the row-perpendicular mixing ($\sigma_{u_\perp}$) during periods of row-parallel winds. In Miller et al. (2016), this was attributed to the structure of the canopy and the variation in the net canopy drag with $\overline{wd}$. The

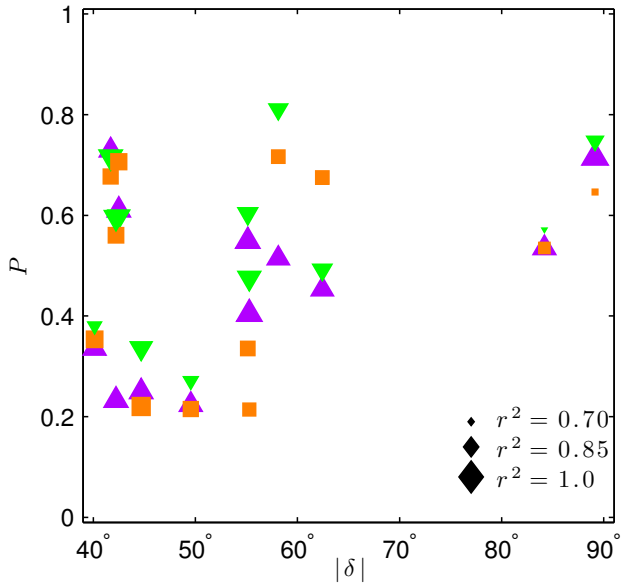

Figure 4.7: The fraction of the plume mass accounted for by the perpendicular portion of the SuperGauss. *Violet triangles*, *orange squares*, and *green triangles* represent data from the violet, orange, and yellow/green microsphere plumes that were released at H_r = 1.51 m, 1.16 m, and 0.81 m, respectively. Marker sizes correspond to the r^2 values determined in real space with approximate relative sizes demonstrated by the *black diamonds*.

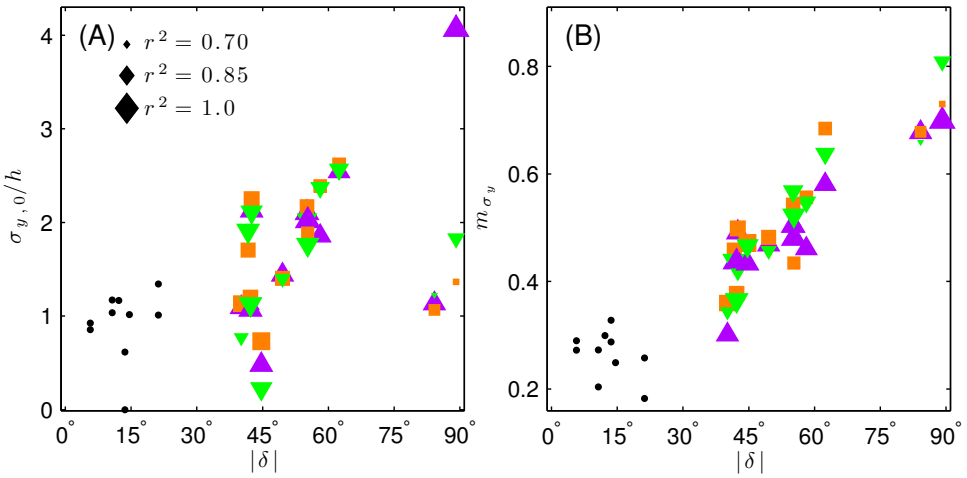

Figure 4.8: The width of the plume at the source (A) and the rate of increase in the plume width as a function of $|\delta|$ (B). *violet triangles*, *orange squares*, and *green triangles* represent data from the violet, orange, and yellow/green microspheres plumes that were released at H_r = 1.51 m, 1.16 m, and 0.81 m, respectively. Marker sizes correspond to the r^2 values determined in real space with approximate relative sizes demonstrated by the *black diamonds*. The *black circles* depict data from the near-parallel plumes published in Miller et al. (2015) and are not sized by any r^2 values.

combination of the behavior's of u_a and the spanwise mixing resulted in row-parallel oriented plumes being channeled along the aisle, moving at a higher average speed, and staying relatively narrow. During periods of row-perpendicular winds, spanwise mixing within the canopy was relatively large and streamwise advection was low, leading to a wider plume source and an increased rate of spread with x.

In eight of the 12 release events, the plumes with H_r = 1.16 m had higher values of m_{σ_y} than did the plumes of either the higher or lower H_r values. Because these plumes were released near the middle of the canopy height (the densest portion) while the other colors were released closer to the canopy top and the canopy understory, it was likely that those plumes had a lower apparent spread rate because they were able to pass over or under the vine rows more easily. This would have prevented them from being forced to spread laterally as much as the mid-height plumes which would have been forced to spread out more before being able to slowly pass through the vine rows or before spreading enough vertically to pass under or over the vine rows. Of the remaining four release events, the largest value of m_{σ_y} came from the plumes released near the canopy bottom in three of them and from the plume released highest in the canopy in one. The same result was seen with σ_{y0}. Specifically, it had the largest values for the plume released near the middle of the vine height in seven of the 12 events. The remaining five events were split three to two for the other two release heights.

Similarly to the spanwise spread behavior, σ_{z0} and m_{σ_z} also increased with $|\delta|$ (Fig. 4.9). This result seemed to conflict with the finding in Miller et al. (2016) that vertical mixing (σ_w) within the canopy sub-layer (CSL) was actually larger during row-parallel flow periods than during row-perpendicular ones. Obviously, however, based on a simple argument of mass-conservation, during periods of row-perpendicular mean-flow, it was necessary that some flow pass over and under the individual vines due to the vines limiting the flow that could pass directly through. Bailey and Stoll (2013) demonstrated the spatial variation in the mean vertical velocity in the vines' wake regions. It showed that flow regularly passed through the understory of the vines and returned upwards on the wake side while some also moved upwards and over the vines only to return downward again on the back side. This behavior would likely

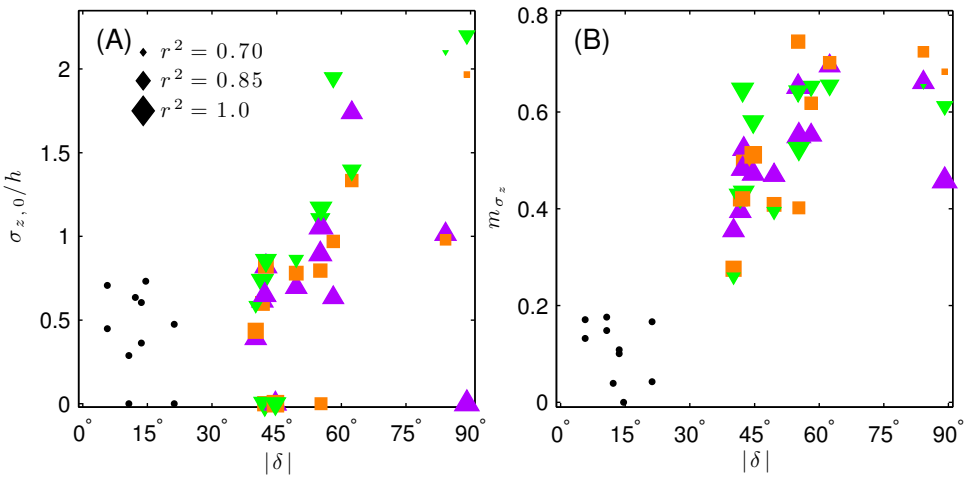

Figure 4.9: The vertical dimension of the plume at the source (A) and the rate of increase of σ_z for the whole plume as a function of $|\delta|$ (B). *violet triangles*, *orange squares*, and *green triangles* represent data from the violet, orange, and yellow/green microspheres plumes that were released at H_r = 1.51 m, 1.16 m, and 0.81 m, respectively. Marker sizes correspond to the r^2 values determined in real space with approximate relative sizes demonstrated by the *black diamonds*. The *black circles* depict data from the near-parallel plumes published in Miller et al. (2015) and are not sized by any r^2 values.

force the plume to spread in the vertical direction with increasing downwind distance, regardless of the relatively quiescent behavior of the vertical turbulent fluctuations within the canopy. From this, it could be concluded that mass conservation of the mean flow field plays an important, if not dominant, role in the vertical transport of the row-perpendicular component of particulate transport in vineyard-like canopies.

Additionally, because u_a was much lower during row-perpendicular flow periods, the plume had more time to be affected by the limited vertical turbulent mixing before reaching a given downwind distance. When σ_w/u_a was studied from the z = 1.3 m anemometer, it tended to increase from ≈ 0.83 to ≈ 1.82, on average, as $|\delta|$ increased from 40° to 90°. This was the case for the meteorological data collected during each of the release events, as well as for all of the "neutral" and "moderately convective" periods from the dataset used in Miller et al. (2016). Interestingly, because the trend in σ_w/u_a roughly matched that of m_{σ_z}, the value of $m_{\sigma_z} \times (u_a/\sigma_w)$ was essentially constant with δ. Averaged across all 36 of the plumes, $m_{\sigma_z} u_a/\sigma_w$ was = 0.510 with a standard deviation of only 0.137, and no observable trend with δ.

It was also observed that there was no apparent trend for m_{σ_z} as a function of H_r. From the 12 release events, in four of them the violet plume had the largest value, in four of them the orange plume had the largest, and in four of them the yellow/green plume had the largest. For σ_{z0}, nine of the 12 events had the largest values for the plumes released the lowest in the canopy, meaning that although those plumes had the largest vertical source dimension, they then grew at basically the same rate as the plumes released at other heights, on average. This may have been caused by the upward movement of the flow coming through the open understory of the vine just upstream of the source location, but such a conclusion is difficult to test in the field. As was mentioned in Miller et al. (2015), the vertical resolution of the impaction traps near the ground created some uncertainty with determining vertical plume parameters for the plumes released near the bottom of the canopy. Although we positioned the lowest impaction trap on each tower closer to the ground during this study than in 2011, this same issue of lower resolution near the ground created some uncertainty in the σ_{z0} values for the plumes with the lowest H_r's.

The values of $\mu_{y,max}$ determined for the whole plumes showed that larger offsets

were typically seen for plumes with lower values of $|\delta|$ (among the range of δ values reported here). The spanwise location of the maximum value of Π at each x was offset from the $\overline{wd}$ vector by essentially zero for the plumes with $|\delta|$ nearest to 90° (Fig. 4.10A). These values of $\mu_{y,max}$ were plotted versus nondimensional advection times defined as the downwind distance over $\overline{u_h}$ for each event ($t = x/\overline{u_h}$) normalized by an eddy turnover time. The turnover time was defined as h divided by the standard deviation of the canopy-top spanwise velocity component, defined around $\overline{wd}$ ($T_y = h/\sigma_v$). The $\mu_{y,max}$ values were negative at most downwind distances for the majority of the plumes. This corresponded to the max concentration location being offset to the left of $\overline{wd}$ when viewed from the source location. This offset was therefore in the direction of the vine rows, and suggested that for lower values of $|\delta|$, there was a higher likelihood of mass being partially channeled down the vine rows instead of following $\overline{wd}$.

Values of γ_y were positive at most downwind distances for the majority of the plumes, and typically trended towards zero with increasing t/T_y (Fig. 4.10B). Positive values of γ_y corresponded to the longer tail of the spanwise distribution being pointed to the right when viewed from the source. Therefore, while $\mu_{y,max}$ was typically offset to the left of $\overline{wd}$, the plume was skewed back toward $\overline{wd}$. This likely indicated that while some portion of the mass was channelled into the vine row direction, it was also being pushed through or around the vines back toward the mean wind direction. Because of this, γ_y typically had the opposite sign of μ_y and $\mu_{y,max}$ (Fig. 4.10C), which was consistent with the near-parallel plumes reported in Miller et al. (2015). Those plumes also had opposite signs for $\mu_{y,max}$ and γ_y for the majority of the downwind distances across all the plumes. The magnitudes of γ_y for each plume decreased with t/T_y, suggesting that with downwind distance, the plumes trended toward spanwise symmetry. This was apparent regardless of δ but manifest as a larger change in the magnitude of γ_y for plumes with lower values of $|\delta|$. Although both $\mu_{y,max}$ and γ_y tended to decrease with $|\delta|$, there did not appear to be a continuous correlation between the two, especially for plumes with $|\delta|$ in the 40° to 65° range.

The kurtoses of the spanwise profiles also tended to have the highest magnitudes for plumes released during periods with lower magnitudes of δ and at downwind

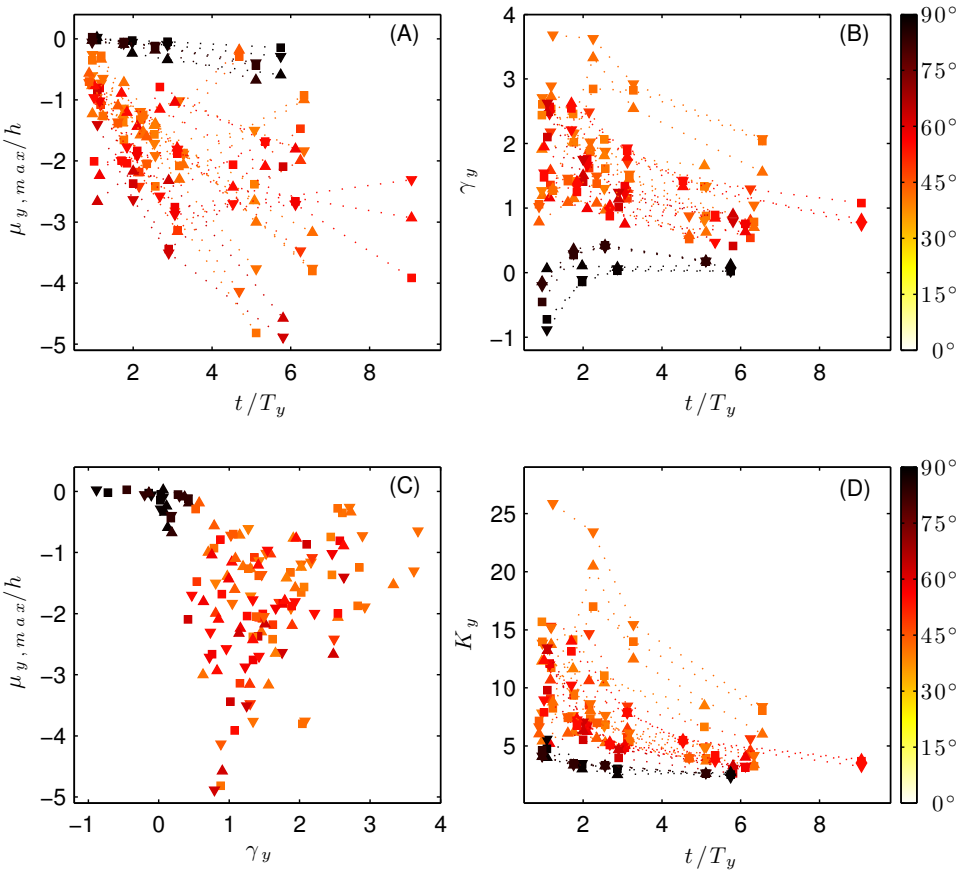

Figure 4.10: The values of $\mu_{y,max}$ versus the nondimensional advection time (A), the skewness of the spanwise distribution about $\overline{wd}$ vector as a function of the nondimensional advection time (B), $\mu_{y,max}$ versus γ_y (C), and the spanwise kurtosis about $\overline{wd}$ vector as a function of the nondimensional advection time (D). Upward pointed *triangles*, *squares*, and downward pointed *triangles* represent data from the violet, orange, and yellow/green microspheres plumes that were released at H_r = 1.51 m, 1.16 m, and 0.81 m, respectively. Each line is for a single plume and is colored by $|\delta|$.

locations nearest to the source (Fig. 4.10D). For a fixed standard deviation, a large K_y value indicates a relatively narrow and peaked distribution function, a kurtosis of 3.0 indicates a normal distribution, and a distribution with a kurtosis of < 3 appears flatter or even box shaped. Because K_y decreased for all plumes with increasing downwind distance, the spanwise shape must have transitioned towards being somewhat flatter than near the source where it was more peaked, given the specific values of σ_y at each distance x.

Similarly to the behavior of $\mu_{y,max}$, the plumes with the lower values of $|\delta|$ typically had the highest magnitudes of γ_y and K_y (Fig. 4.11). The values of γ_y reported in Miller et al. (2015) never exceeded unity because the SNDF was incapable of producing a distribution shape with $|\gamma_y| > 1.0$. Fortunately, all of the row-aligned plumes reported therein met this criteria. For many of the non-row-aligned plumes investigated here, that was not the case, and values of $\gamma_y > 1.0$ were not uncommon. This was especially true for the the plumes with lower $|\delta|$ values and for smaller downwind distances. Combined with the skewness data from Miller et al. (2015), this meant that plumes that were nearly row-parallel and those that were almost perfectly row-orthogonal had the lowest γ_y values, while those with $|\delta| \approx 45^\circ$ had the largest relative spanwise skewnesses. Such a finding seems intuitively consistent with the behavior of $\overline{u'_\perp v'_\parallel}$ within the canopy, specifically, that cross-vine mixing and stress-tensor asymmetry were most prevalent and complicated when winds were row-diagonal (Miller et al., 2016). From among the plumes studied here, K_y was also largest for plumes with $|\delta| \approx 45^\circ$. This was likely due to the channeling of the plumes down the rows that also led to decreased σ_y values. For the plumes that were released during periods when the winds were nearly row-perpendicular, the spanwise profiles were flatter (along with being wider—larger σ_y values) due to the enhanced spanwise mixing and resistance to streamwise advection due to the increased drag caused by the vine rows (Miller et al., 2016).

4.4 Summary and Conclusions

The microsphere plumes collected in Oregon provided an extensive, relatively high-resolution, 3D dataset of plume concentrations in a trellised canopy in the

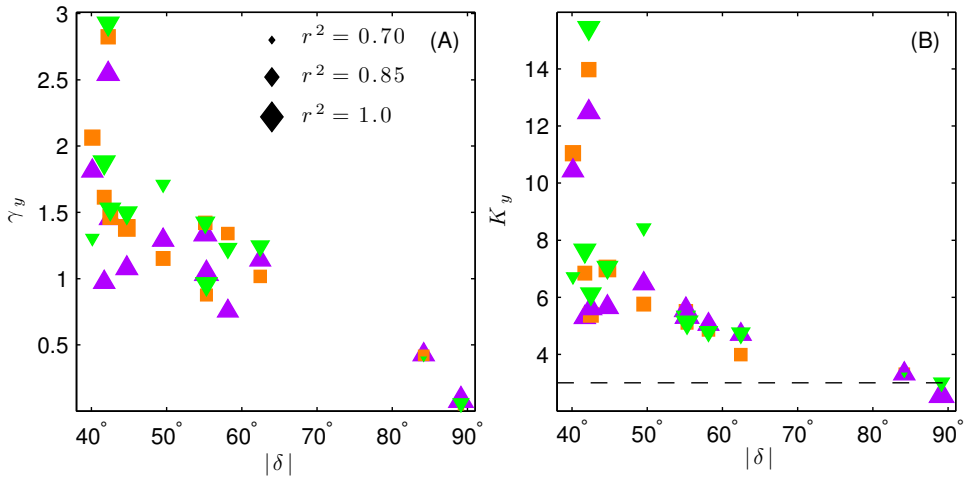

Figure 4.11: The spanwise skewness (A) and the spanwise kurtosis (B) at x = 8.0 m as a function of $|\delta|$. *violet triangles*, *orange squares*, and *green triangles* represent data from the violet, orange, and yellow/green microspheres plumes that were released at H_r = 1.51 m, 1.16 m, and 0.81 m, respectively. Marker sizes correspond to the r^2 values determined in real space with approximate relative sizes demonstrated by the *black diamonds*. The horizontal *black dashed* line in B depicts the kurtosis value of a univariate normal distribution, i.e., K_y = 3.0.

vicinity of the plumes' sources. The plumes were analyzed by fitting a weighted sum of two Gaussian plume distribution equations to the concentration data collected in the field. Moments and parameters determined from the fit of the SuperGauss provided an understanding of the plumes' shapes and behaviors as function of H_r and δ. Combined with the details of the nearly-row-parallel plumes reported in Miller et al. (2015), the information presented herein creates a relatively complete picture of the expected behavior of particulate plumes in vineyard and vineyard-like canopies. These findings show that the discrete architecture of the vineyard canopy does indeed exhibit a specific signature on the shape of particulate plumes released into the CSL. Unlike plumes studied in other canopy types or in freestream flows, these proved to be more complex and highly non-Gaussian. Some plume parameters showed consistent behavior with variations in δ, and although some did not exhibit such clear relationships, they all show just how complicated the influence of the vineyard canopy is on plume dynamics. The dimensions of the effective plume source in the spanwise and vertical directions both tended to increase with $|\delta|$. The rate of spread with downwind distance in both the spanwise and vertical directions also tended to increase with $|\delta|$. This behavior was primarily attributed to spread caused by the conservation of mass of the mean flow, to the decrease in u_a within the canopy as $|\delta|$ increased, and also to the variations in the magnitudes of the turbulent mixing components as $\overline{wd}$ varied from row-parallel to row-perpendicular. These findings were shown to also be consistent with the row-parallel plumes published in Miller et al. (2015), which had relatively small effective source sizes and did not expand in the spanwise or vertical directions as quickly as the plumes reported herein. The plumes also tended to have some portion of the released mass being channeled down the canopy aisle, with a smaller portion of that mass being channeled as $|\delta|$ increased. This channeling typically led to a skewness in the plume shape, with the long tails being pointed from the row the plume was channeled down back toward $\overline{wd}$. With increasing downwind distances, the plumes trended toward symmetry and towards more Gaussian-like shapes as influences of the near-source canopy discontinuities were diminished on the average.

The plume shape details examined via the Oregon field campaigns and explained

both here and in Miller et al. (2015) provide a basis from which simple plume models could be developed and validated. Further steps in linking the findings reported here to meteorological conditions and canopy-specific parameters would still be necessary in that development. Additionally, some complexities of the CSL flow and its influence on the plume shape are difficult to parse out solely from the field data, and for which, 3D simulations using Large-Eddy Simulation or high-resolution wind-tunnel experiments would likely be necessary to understand. This includes behaviors like understory particle transport, ejection of particles from the canopy, and vine-wake recirculation. Bailey and Stoll (2013) and Bailey et al. (2014) have reported some work in this regard but only focused on cases with $\delta = 90^{\circ}$. Further work of similar quality will allow for even more accurate, spatially resolved models of particulate transport in canopies like those studied here.

4.5 References

Allwine, K. J., J. H. Shinn, G. E. Streit, K. L. Clawson, and M. Brown, 2002: Overview of urban 2000: A multiscale field study of dispersion through an urban environment. *Bull. Amer. Meteor. Soc.*, **83**, 521–536.

Aylor, D. E. and F. J. Ferrandino, 1989: Dispersion of spores released from an elevated line source within a wheat canopy. *Boundary-Layer Meteorol.*, **46**, 251–273.

Aylor, D. E. and T. B. Sutton, 1992: Release of *venturia inaequalis* ascospores during unsteady rain: Relationship to spore transport and deposition. *Phytopathology*, **82**, 532–540.

Bailey, B. N. and R. Stoll, 2013: Turbulence in sparse, organized vegetative canopies: A large-eddy simulation study. *Boundary-Layer Meteorol.*, **147**, 369–400.

Bailey, B. N., R. Stoll, E. R. Pardyjak, and W. F. Mahaffee, 2014: Effect of vegetative canopy architecture on vertical transport of massless particles. *Atmos. Environ.*, **95**, 480–489.

Bailey, B. N., R. Stoll, E. R. Pardyjak, and N. E. Miller, 2016: A new three-dimensional energy balance model for complex plant canopy geometries: Model development and improved validation strategies. *Agric. For. Meteorol.*, **218–219**, 146–160.

Belcher, S. E., 2005: Mixing and transport in urban areas. *Phil. Trans. R. Soc. A*, **363**, 2947–2968.

Braun, U., 1995: *The Powdery Mildews (Erysiphales) of Europe*. Gustav Fischer Verlag, New York, 337 pp.

Brown, J. K. and M. S. Hovmoller, 2002: Aerial dispersal of pathogens on the global and continental scales and its impact on plant disease. *Science*, **297**, 537–541.

Chamecki, M., N. S. Default, and S. A. Isard, 2012: Atmospheric dispersion of wheat rust spores: A new theoretical framework to interpret field data and estimate downwind dispersion. *J. Appl. Meteorol. Climatol.*, **51**, 672–685.

Gleicher, S. C., M. Chamecki, S. A. Isard, Y. Pan, and G. G. Katul, 2014: Interpreting three-dimensional spore concentration measurements and escape fraction in a crop canopy using a couple eulerian-lagrangian stochastic model. *Agric. For. Meteorol.*, **194**, 118–131.

Gregory, P. H., 1973: *The Microbiology of the Atmosphere*. Leonard Hill Books, London, 377 pp.

Hanna, S. R. and E. Baja, 2009: A simple urban dispersion model tested with tracer data from Oklahoma City and Manhattan. *Atmos. Environ.*, **43**, 778–786.

Hanna, S. R., R. Britter, and P. Franzese, 2003: A baseline urban dispersion model evaluated with Salt Lake City and Los Angeles tracer data. *Atmos. Environ.*, **37**, 5069–5082.

Hanna, S. R., J. White, and Y. Zhou, 2007: Observed winds, turbulence, and dispersion in built-up downtown areas of Oklahoma City and Manhattan. *Boundary-Layer Meteorol.*, **125**, 441–468.

Huq, P. and P. Franzese, 2013: Measurements of turbulence and dispersion in three idealized urban canopies with different aspect ratios and comparisons with a gaussian plume model. *Boundary-Layer Meteorol.*, **147**, 103–121.

Jarvis, W. R., 1977: *Botryotinia and Botrytis Species: Taxonomy, Physiology, and Pathogenicity. A Guide to the Literature.*, 195. Research Branch, Canada Department of Agriculture, Harrow, Ontario.

Lauri, P.-E., 2009: Developing a new paradigm for apple training. *Compact Fruit Tree*, **42**, 17–19.

Mahaffee, W., G. Grove, and R. Stoll, 2011: Inoculum detection to manage grape powdery mildew. *Practical Winery & Vineyard*, **Spring**, 26–32.

Mahaffee, W., S. Schwebs, F. Hand, D. Gubler, B. Bailey, and R. Stoll, 2014: Improving management of grape powdery mildew with new tools and knowledge. *Practical Winery & Vineyard*, **April**, 59–67.

Mahaffee, W. F. and R. Stoll, 2016: The ebb and flow of airborne pathogens: Monitoring and use in disease management decisions. *Phytopathology*, **106**, 420–431.

Miller, N. E., R. Stoll, W. Mahaffee, T. M. Neill, and E. Pardyjak, 2015: An experimental study of momentum and heavy particle transport in a trellised agricultural canopy. *Agric. For. Meteorol.*, **211–212**, 100–114.

Miller, N. E., R. Stoll, W. Mahaffee, and E. R. Pardyjak, 2016: The mean and turbulent flow statistics in a trellised agricultural canopy. *Boundary-Layer Meteorol.*, submitted.

Pady, S. M. and J. Subbayya, 1970: Spore release in uncinula necator. *Phytopathology*, **60**, 1702–1703.

Pan, Y., M. Chamecki, and S. A. Isard, 2014: Large-eddy simulation of turbulence and particle dispersion inside the canopy roughness sublayer. *J. Fluid Mech.*, **753**, 499–534.

Pardyjak, E., S. Speckart, F. Yin, and J. Veranth, 2008: Near source deposition of vehicle generated fugitive dust on vegetation and buildings: Model development and theory. *Atmos. Environ.*, **42**, 6442–6452.

Prussin, A. J., L. C. Marr, D. G. Schmale, R. Stoll, and S. D. Ross, 2015: Experimental validation of a long-distance transport model for plant pathogens: Application to *fusarium graminearum*. *Agric. For. Meteorol.*, **203**, 118–130.

Raynor, G. S., J. V. Hayes, and E. C. Ogden, 1974: Particulate dispersion into and within a forest. *Boundary-Layer Meteorol.*, **7**, 429–456.

Robinson, T. L., A. N. Lakso, and Z. Ren, 1991: Modifying apple tree canopies for improved production efficiency. *HortScience*, **26**, 1005–1012.

Spijkerboer, H. P., J. E. Beniers, D. Jaspers, H. J. Schouten, J. Goudriaan, R. Rabbinge, and W. van der Werf, 2002: Ability of the Gaussian plume model to predict and describe spore dispersal over a potato crop. *Ecological Modelling*, **155**, 1–18.

Stockie, J. M., 2011: The mathematics of atmospheric dispersion modelling. *SIAM Review*, **53**, 349–372.

Su, H.-B., H. P. Schmid, C. S. Vogel, and P. S. Curtis, 2008: Effects of canopy morphology and thermal stability on mean flow and turbulence statistics observed inside a mixed hardwood forest. *Agric. For. Meteorol.*, **148**, 862–882.

Venkatram, A., V. Isakov, D. Pankratz, J. Heumann, and J. Yuan, 2004: The analysis of data from an urban dispersion experiment. *Atmos. Environ.*, **38**, 3647–3659.

Waterhouse, G. M., 1973: *Peronosporales*, 165–183. Academic Press, New York.

CHAPTER 5

CONCLUSION

The primary and direct impact of this work is the improved understanding of transport characteristics in perennial trellised agricultural canopies. This is of interest to the research community that has spent considerable time researching the same phenomena in homogeneous and urban canopies. The plume data collected in the vineyard are at a higher spatial resolution than any identified previously published studies and are concentrated to downsteam distances at length scales that have typically been ignored by others. This alone will have impacts in the dispersion-studying and -modeling community. The specific signature of the discrete canopy architecture was found to influence the mean flow in the canopy by way of effects like flow channeling. It influenced the components of the flux tensor within the canopy by creating an asymmetry between components with along-row fluctuations and those with row-normal fluctuations. This asymmetry also resulted in wind-direction based variations in aggregate variables like the displacement height. The canopy architecture also altered turbulent structure and spectra compared to that seen in homogenous canopies or freestream flows. Canopy-top turbulent structures were shown to likely change in thickness, center height, and frequency with changes in wind alignment. Also, shifts were observed in the eddy-scales of the peak premultiplied energy spectra with wind direction changes and with height. The peak were observed at larger scales above the canopy and during periods of row-parallel winds but shifted to smaller scales—roughly equal to the row spacing—at heights within the canopy and during periods of row-perpendicular winds.

Microsphere plumes released during periods of varied above-canopy mean wind directions also showed direct influences from the canopy architecture. Generally, the

channeling of the mean winds into the vine row direction caused the particles to also typically be biased toward dispersion down the rows instead of across vines. This meant that for the plumes released during periods of roughly row-parallel winds, the particles were simply channeled down the rows, the plumes did not spread laterally or vertically very quickly, and the plumes were nearer to symmetric in the spanwise direction. As the mean wind direction above the canopy turned away from row-parallel, the channeling of the plume typically resulted in the plume centerline being offset from that mean wind direction vector and in a spanwise skewness becoming increasingly apparent as some particles were able to migrate across vine rows following that mean wind vector. When the winds turned to fully row-perpendicular, the spanwise offset and skewness essentially disappeared again because neither row-parallel direction was dominant in its channeling. This also meant that the plumes were advected much more slowly, and spread out more quickly in the spanwise and vertical directions.

Collectively, this gives a relatively complete picture of plumes in the vineyard canopy. This understanding is relevant on its own, but is perhaps most useful in its applications to real-world situations seen by growers of trellised crops. The simplest, directly applicable observation of use to growers is the fact that due to the dominance of the row-parallel channeling, particulates like fungal spores are more likely to spread and be deposited along single vine rows than from row to row. For spores specifically, this would likely lead to fungal diseases existing in elongated row-parallel regions in the vineyard, instead of in regions that cross multiple rows. These effects would likely be most perceptible for clones of an originating colony within a few canopy heights of that colony. In battling against the fungal outbreaks, the same observations could be used to inform fungicide applications such that the spray would purposefully drift into the infected areas only and be prevented from drifting beyond the field. Particles that are transmitted more than a few canopy heights (perhaps beyond $8h$) would be more likely to follow traditional Gaussian plume behavior following a direction that likely lies between the mean wind direction above the canopy and the vine row direction. With continued study from other fields with differing row spacings and canopy heights, it may also be possible to determine that there exists some optimal ratio of those values for which disease would be maximally inhibited from ever crossing

from vine to vine. Such a finding could become a natural prophylactic for preventing particulate spread.

5.1 Broader Impacts and Future Work

The modified-Gaussian plume equations used in the curvefitting procedures throughout this work lend themselves well to the development of simple models to predict near-source dispersion patterns in the vineyard. One such model has already been developed for prediction of plume concentrations for plumes released during roughly row-parallel winds, and a validation study of that model using data from the 2013 field campaign is forthcoming. This model—and similar ones for other wind conditions—will explicitly account for the linkages between local meteorology and canopy geometry. Much work still needs to be done in the development and validation of these models. Perhaps the most difficult steps will be determining the functional links between the parameters in the plume model equations and the local meteorological and canopy variables. Fortunately, there are other plume datasets that have been collected in vineyards in Oregon (the one used throughout this work as well as another) that should provide us with ample replicants from which to continue tuning and testing.

Eventually, the goal is to develop these models for use in a comprehensive fast-response epidemiological model that will be distributed to growers (Mahaffee et al., 2014; Mahaffee and Stoll, 2016). Similar epidemiological models have been developed by others (e.g., Sall (1980); Calonnec et al. (2008)), but none have explicitly defined all of the ecosystem processes to the level that is now possible with modern computing resources and with high-resolution data. Although the algebraic models alluded to here would be a primary element of this ecosystem resource, their inability to explicitly resolve the vine rows would require that separate submodules for concentration changes across individual vines and deposition to the canopy surfaces be added. A meteorological model along with real-time data would be used to drive the dispersion, and biological models for the pathogen and plants would predict growth and fecundity based on microclimate variables. Bailey et al. (2016) presented an energy and water budget model for complex canopies that will likely serve as an

important portion of a complete vineyard ecosystem model. No known published models of this type explicitly define the canopy architecture and are therefore limited in their ability to inform management decisions spatially (e.g., fungicide spraying or optimal planning and planting practices). The epidemiological model will combine real-time monitoring and modeling to give up-to-speed pathogen outbreak information which will significantly improve growers' ability to identify and respond to disease foci.

These tools (the dispersion models alone and/or the eventual ecosystem model) will also be easily transferable to other applications. In addition to working for fungal spores, as was the original intent of the model development, the dispersion model could directly be used for transport of other heavy particles like dust and pesticide droplets within the vineyard. The dispersion model would also be easily adaptable for use in heavy particle transport in any canopy with a discrete 2D-style architecture like that of vineyards. Most simply this includes trellised orchards, berry patches, hop yards, tree farms, and homogeneous crop types—like corn—at early stages of the growing season when plant height is small. With only limited additional effort, the dispersion-pattern based discoveries reported here could also be added to near-source dispersion models in urban and quasi-urban canopies. One obvious difference for which account would need to be made is the solidity of buildings compared to plants. It is known, however, that at certain scales, spanwise profiles of particulate concentrations are channelled along street canyons and are skewed back towards the mean wind direction (Yee and Biltoft, 2004). Finally, the dispersion model could also be used for the tracking of scalars in similar canopies, by simply removing mass-based effects like settling velocity. This could have application in energy, water, and biosecurity models. With some greater effort, focused significantly on the biological submodels, the forthcoming epidemiological model could be adapted for use in many other canopies as well as for other aerially dispersed biologicals like aphids.

5.2 References

Bailey, B. N., R. Stoll, E. R. Pardyjak, and N. E. Miller, 2016: A new three-dimensional energy balance model for complex plant canopy geometries: Model development and improved validation strategies. *Agric. For. Meteorol.*, **218–219**,

146–160.

Calonnec, A., P. Cartolaro, J. Naulin, D. Bailey, and M. Langlais, 2008: A host-pathogen simulation model: powdery mildew of grapevine. *Plant Pathology*, **57**, 493–508.

Mahaffee, W., S. Schwebs, F. Hand, D. Gubler, B. Bailey, and R. Stoll, 2014: Improving management of grape powdery mildew with new tools and knowledge. *Practical Winery & Vineyard*, **April**, 59–67.

Mahaffee, W. F. and R. Stoll, 2016: The ebb and flow of airborne pathogens: Monitoring and use in disease management decisions. *Phytopathology*, **106**, 420–431.

Sall, M., 1980: Epidemiology of grape powdery mildew: A model. *Phytopathology*, **70**, 338–342.

Yee, E. and C. A. Biltoft, 2004: Concentration fluctuation measurements in a plume dispersing through a regular array of obstacles. *Boundary-Layer Meteorol.*, **111**, 363–415.

APPENDIX A

2011 FIELD NOTES

A.1 Introduction

This is a transcription of the field notes collected during the 2011 field campaign conducted in a vineyard near Monmouth, Oregon in collaboration with the USDA-ARS labs in Corvallis. While in the field, notes were taken on the experimental procedures, the equipment locations and layouts, timestamps, and more, the details of which are condensed and organized here.

A.2 Meteorological Tower

One meteorological (met.) tower was deployed at a central location within the southwesterly most block of the vineyard (44° 49.465′ N 123° 14.265′ W). The tower was erected in the center of the aisle and was positioned such that the anemometers would be mounted off of the northernmost edge. A Campbell Scientific CR5000 datalogger was used to collect the data from the sensors deployed on the tower.

A.2.1 Anemometers

Four Campbell Scientific CSAT3 sonic anemometers were deployed at heights of:

- 196.75″
- 113.98″
- 71.10″
- 33.23″

These heights were all measured above ground level (AGL) at the tower base and to the center of the anemometers' sampling volumes.

The anemometers were oriented such that the CSAT3 heads pointed at a heading of 0°. All four CSAT3's were mounted in perfect vertical alignment (sampling volumes directly above each other) with the sampling volumes nearly centered in the aisle. Their sampling volumes of the bottom two anemometers were measured to be 51″ from the centerline of the vine row to the west of the tower and 47″ from the centerline of the vine row to the east of the tower. Because the anemometers were mounted off the northern edge of the tower and were also pointed north, periods with winds from the south (between 165° and 195°) should be ignored from analysis.

A.2.2 Fine-wire Thermocouples

Each CSAT3 had either a Campbell Scientific FW05 or FW1 fine-wire thermocouple (TC) collocated with it such that the couple was located at the same heights as the sampling volume heights listed for the CSAT3's. All of the fine-wire thermocouples were wired to the datalogger and were logged in order based on height, i.e., the fine-wire at 196.75′′ is fine-wire TC number one.

A.3 Other Energy Budget Sensors

A variety of other sensors were deployed into the vineyard along with the met. tower in order to collect other variables associated with the wind and canopy energy budgets.

A.3.1 Infrared Radiometers

Two Apogee SI-111 Infrared Radiometers were mounted to a poll located to the south of the main tower but within the same aisle. The first radiometer (IRR1) was pointed at the ground in the center of the aisle. It was mounted 46″ AGL. It was positioned 54″ from the centerline of the vine row to the west and 44″ from the centerline of the row to the east. The second radiometer (IRR2) was mounted at 45.5″ AGL and was pointed straight at the western "face" of the leaves of the vine row located to the east of the sensor. IRR2 was 24″ from the "surface" of the leaves at which it was pointed orthogonally too.

A.3.2 Leaf Movement Sensors

A set of piezoelectric motion sensors were mounted to both real and artificial leaves in the canopy in an area south of the main tower. The sensors were the DT series from Measurement Specialists. The artificial leaves were made from clear mylar film and were cut to roughly match the dimensions of an "average" grape leaf. DT sensors were attached to the artificial leaves using glue and to the real leaves on the vine while in the field using fingernail polish. Use of fingernail polish was a method suggested by Walt Mahaffee as a method the USDA staff has used before to attach objects to the surfaces of leaves. The individual sensors were connected to differential channels on the CR5000 as follows:

- Channel 5: Artificial leaf, 64″ AGL
- Channel 6: Real grape leaf, 48″ AGL
- Channel 8: Artificial leaf, 46″ AGL
- Channel 9: Artificial leaf, 30″ AGL
- Channel 15: Artificial leaf, 51″ AGL
- Channel 16: Real grape leaf, 34″ AGL
- Channel 18: Artificial leaf, 67″ AGL
- Channel 19: Artificial leaf, 34″ AGL
- Channel 20: Real grape leaf, 65″ AGL

The sensors on the real grape leaves were mounted upside down, and all sensors were wired to the datalogger in the same way. This likely means that the data signals from the real leaves require a sign change in order to systematically match the data from the artificial leaves.

Nearly zero analysis has been performed on the data collected by these sensors as of this writing, primarily because it is unclear as to how the data signals should be interpreted. The DT sensors give a voltage output based on bending, twisting, and

compression, and possibly from vibration and temperature change. Any of these movements produced a voltage response which then decayed back toward a zero voltage as long as no new movement was initiated. Analysis of the voltage data streams requires an understanding of the typical voltage magnitudes associated with movements of different magnitudes over different time scales and an understanding of the time constants that control the decay in those voltages when the movements cease. Such understanding has not been studied and thus the raw voltage signals have not been extensively studied.

A.4 Canopy Dimensions and Characteristics

The canopy in the vicinity of the tower was trimmed to a height of 72–76″ on average. The open understory was about 30″ tall (AGL) with the fruiting wire typically at about 31″ AGL. The vine rows were oriented from 0° to 180° and were at an average spacing of 98″ on center. Along each vine row, the individual plants were planted at a spacing of 5 ft on average. Most plants were believed to be approximately 5 years old and had trunk diameters between 1″ and 1.5″. The vine rows were trimmed by hand at least once during the campaign, but a considerable number of shoots often extended into the aisles. The majority of the leaves and shoots were kept to an average row thickness of $\approx 18''$. Every other aisle in the block was tilled and left as dirt while the others were allowed to have grasses and weeds to grow in them. After the field campaign ended, the USDA staff collected data to determine the leaf area density and leaf area index of the vineyard.

A.5 Microsphere Release Events

A series of 16 microsphere release experiments were conducted in the vineyard during the field campaign.

A.5.1 Microspheres

Fluorescent polyethylene microspheres of two different colors were used in the field to study plume shapes under different meteorological conditions. Two colors of microspheres — yellow/green (UVPMS-BY2-1.00, Cospheric LLC) and orange (UVPMS-BO-1.00, Cospheric LLC) — were used.

A.5.2 Release Devices

The microspheres were released into the canopy using vibrating funnels constructed by Andrew Gould following the work of Bouvet et al. (2006). The funnels were constructed of standard plastic chemistry funnels purchased from the chemistry supply room on campus at the University of Utah. Custom inserts were machined to fit into the necked ends of the funnels. They were contracted and obtained by the USDA staff in Oregon from a machine shop in Corvallis. The inserts were press-fit into the funnel ends and had an orifice with a diameter of 210 μm drilled through them, through which the microspheres were able to fall when vibrated in the field. A 3VDC micro-vibration motor was glued to each funnel and powered by a battery pack with a switch. The vibration of the funnel theoretically produced a steady stream of microspheres out of the funnel during the release periods, during which the switches were turned on. Before each release event, microspheres were added to each funnel. Before and after each release event, the funnels were weighed in order to determine the mass of microspheres that was released during each event.

The funnels were held in the canopy using three-finger chemistry clamps which were mounted onto T-posts that were placed such that they were up against the surface of the vine canopy. The T-posts were located at approximately 44° 49.471′ N 123° 14.265′ W. The funnels were held out away from the nearest leaves by about 3″. The T-post used to hold funnels during events with northerly winds was positioned on the western face of the vine row that was just to the west of the met. tower, and far enough north of the met. tower that all sampling of the plume for those events was done upwind of the tower. The T-post used for events with westerly winds was positioned on the eastern face of the vine to the west of the met. tower and was thus only about 2 feet from the other T-post. This resulted in the locations of the funnels for northerly releases being $\approx 25''$ away from the locations of the funnels for westerly releases.

For the release events conducted during periods of northerly winds, funnels were mounted at one or two of three possible heights on the T-post at the release location: 68″, 49″, or 26″ AGL. For the events conducted during westerly winds, the funnels were mounted at heights of either 67.25″, 49.125″, or 27″ AGL on the T-post used

for those events.

A.5.3 Impaction Traps

The microspheres were collected using rotating arm impaction traps built by the USDA-ARS labs. Five impaction traps were mounted at different heights onto towers made of aluminum 80/20 T-channel. The five heights were measured from the ground to the trap crossarm for each tower and all had approximate heights of:

- 0.41 m
- 0.76 m
- 1.19 m
- 1.60 m
- 4.85 m

These trap heights should only be assumed to be accurate to about ±2″. The height of the top impaction trap was not ever actually measured in the field and is only quoted here as the height in the designs for the towers. It is possible that based on local ground discrepancies and individual variation between one tower and the next, these heights are only accurate as an average approximation. The actual center of the sampling volume at each of these impaction traps is likely half the substrate height above the heights listed here. Each impaction trap's crossarm had a radius from the motor drive shaft to the center of the substrate rod hole of 3.5 cm. Thirty-three towers were used to make a three-dimensional array that was deployed downwind of the plume source locations.

A.5.3.1 Tower Arrays

The impaction trap towers were arranged into one continuous array ranging from the southwest of the release locations to the northeast of the release locations. The array was divided into three zones for use in remotely turning the impaction traps on and off using a wireless network. A simple layout for the tower array was designed prior to the field campaign and believed to be sufficient to capture the plume shape

over all the expected wind directions (Figure A.1). Schematic layouts of the trap array were written in the handwritten notes during the field campaign so that the approximate locations of the towers with respect to the release location could be determined for use during analysis (Table A.1).

A.5.3.2 Array for Westerly Releases

Two of the three zones of the trap tower array were used for microsphere release events during westerly winds. Zone 1 consisted of tower numbers 1–5, 8–12, 15, 17, and 18. Zone 2, which was used for both westerly and northerly release events, consisted of tower numbers 6, 7, 13, 14, 19, and 20 (Figure A.1).

A.5.3.3 Array for Northerly Releases

Zones 2 and 3 of the trap tower array were used for microsphere release events conducted during northerly winds. Zone 3 consisted of tower numbers 16 and 21–33 (Figure A.1).

A.5.4 Release Events

Of the 16 release events that were conducted, the first four events were immediately recognized to have been unusable and were therefore never analyzed and are excluded from explanation here (Table A.2). The final two events were conducted by the USDA staff after all University of Utah staff had returned home. Events 5–14 were timed using a windows netbook that was in Utah time and was also off by approximately 35 additional seconds compared to the CR5000 time. The timestamps for everything throughout the campaign were corrected to the CR5000 clock after the CR5000 clock was correct for Oregon time (Section A.6.1).

A.6 Data Files Info.

A.6.1 Met. Tower

All sensors were sampled at 20 Hz and written to a table that was converted to comma separated after the campaign. The comma separated files were then processed in MatLab to convert them to easily usable .mat files. In processing them into .mat files, the timestamps throughout the different files were corrected to Oregon local

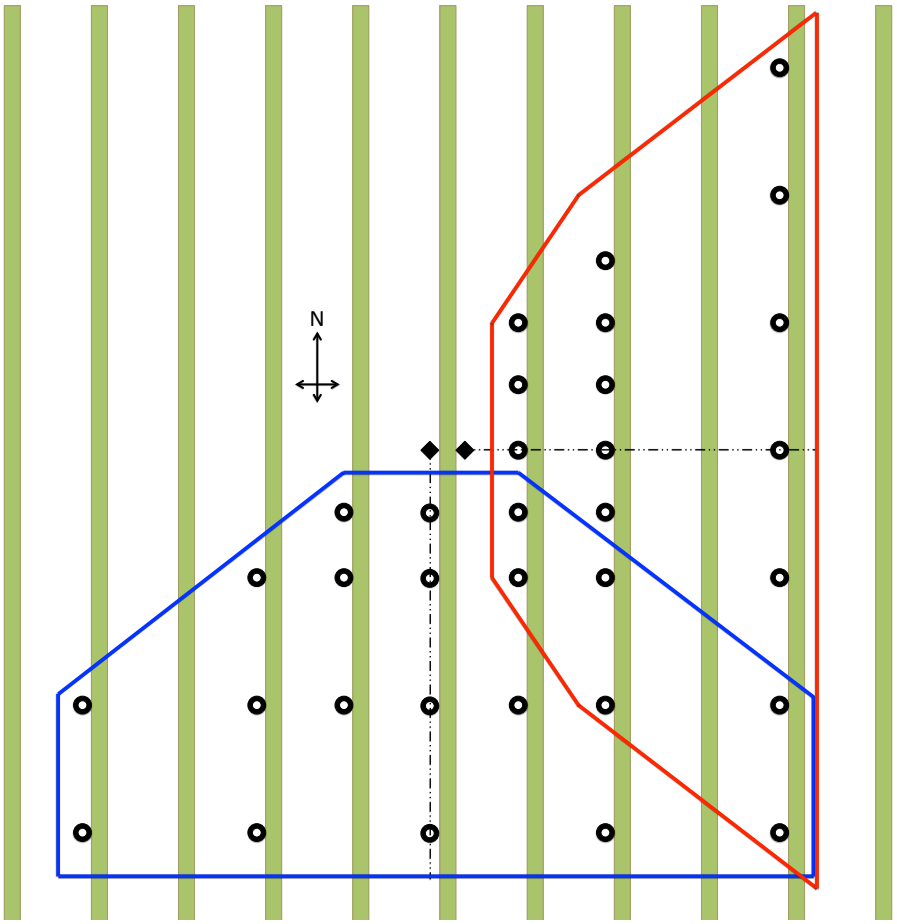

Figure A.1: Schematic of the impaction trap layout with respect to the release device locations within the vineyard. The tower locations are represented by the open circles, the release device locations are represented by the black diamonds, and the vine rows are represented by the green patches. The red and blue outlines enclose the impaction trap towers used for the westerly release events and the northerly release events, respectively. The impaction trap towers enclosed by both the red and blue outlines were used for the release events for both wind directions.

Table A.1: Approximate locations of the impaction trap towers within the array. All coordinates are with respect to the T-post used for the northerly release events

Tower number	distance east [inches]	distance north [inches]
1	354	369.5
2	354	253.5
3	354	128.5
4	354	4.5
5	354	-119.5
6	354	-241.5
7	354	-362
8	159	191.5
9	157.3	131.5
10	155.9	71.5
11	157.9	6.5
12	155.4	-52.5
13	158.6	-113.5
14	160.8	-236.5
15	63.4	131.5
16	155.4	-358.5
17	60.3	67.5
18	59.4	8.5
19	60.3	-58.5
20	59.4	-114.5
21	64.1	-237.5
22	0	-55
23	0	-118
24	0	-240
25	0	-362
26	-100.9	-59.3
27	-100.9	-120.3
28	-97.4	-244.3
29	-199.2	-111
30	-199.2	-231
31	-199.2	-353
32	-396.7	-234
33	-396.7	-355

Table A.2: Release events conducted. The timestamps are in the corrected CR5000 time in Oregon time. Color/height pairs correspond to the color of microspheres (Y for yellow/green and O for orange) released and one of the three clamp height positions for the vibrating funnels on the T-post for the respective wind directions (Section A.5.2). The mass amounts listed are the total mass of microspheres released and are in the same order as the color/height pairs, respectively.

Event	Direction	color/height	Duration (min)	Date	Start Time	Mass [g]
5	W	O/Mid	15	9/27	19:13:17	0.11
6	N	Y/Top, O/Bot	5	9/28	17:15:21	0.20, 0.16
7	N	Y/Top, O/Bot	5	9/28	18:28:15	0.24, 0.37
8	N	Y/Top, O/Bot	5	9/29	12:12:45	0.64, 0.00
9	N	Y/Mid, O/Bot	7	9/30	11:03:35	0.16, 0.83
10	N	Y/Mid, O/Bot	7	9/30	12:55:20	0.23, 0.59
11	W	Y/Top, O/Bot	7	9/30	13:56:35	0.36, 0.21
12	W	Y/Top, O/Mid	7	9/30	14:44:55	0.21, 0.57
13	W	Y/Top, O/Mid	7	9/30	15:50:55	0.57, 0.42
14	W	Y/Bot, O/Mid	7	9/30	17:15:15	0.58, 0.75
15	N	Y/Top, O/Bot	7	10/13	12:01:00	0.50, 0.34
16	N	Y/Top, O/Bot	7	10/13	13:40:44	0.73, 0.88

time. The clock on the CR5000 was set to a French timezone during a previous experiment and was not updated for this campaign. This resulted in the CR5000 timestamps in the original files being seven hours ahead of Oregon time. The .mat files then had columns in the following order:

- Timestamp: 6 columns covering month, day, year, hour, minute, second in Oregon time
- 5 m anemometer: u, v, w, Sonic T
- 3 m anemometer: u, v, w, Sonic T
- 2 m anemometer: u, v, w, Sonic T
- 1 m anemometer: u, v, w, Sonic T
- 4 fine-wire thermocouples from 5 m to 1 m
- 9 leaf motion piezoelectric sensors, numbers 5–20, in order in columns 27–35

and were named using the date on which the file ends, e.g., *09_29_Sonics.mat*.

A.6.2 Infrared Radiometers

The data from the SI-111's were all logged at 1 Hz on a Campbell Scientific CR5000. The data were also converted to .mat files with the data organized in columns in the following order:

- Timestamp: 6 columns covering month, day, year, hour, minute, second in Oregon time
- SI-111's: Sensor body temps ×2, thermopile mV readings ×2, Radiometer target temps ×2.

These files were named in the same manner as above but with "IRR" in the name, e.g., *09_29_IRR.mat*.

A.6.3 Tower Data for Each Release Event

The anemometer and temperature data that were collected during each release event were copied out of the tower .mat files into their own individual .mat files for easy use in calculating meteorological conditions during each event. The appropriate timestamps for each event were used and the data copied to a new .mat file with a naming convention based on the release event number, e.g., *Release5.mat*. Additionally, as a way to check the steadiness of the flow conditions during each of the events, a 30-minute time window which was centered around the central time-point of each release event was also copied out of the tower files into separate .mat files using a similar naming convention, e.g., *Release5_30Window_Centered.mat*.

A.7 Other Notes

Scanned images of the field notes as they were taken in the field should also be used as a reference when using this document with the datasets.

A.8 References

Bouvet, T., J. D. Wilson, and A. Tuzet, 2006: Observation and modeling of heavy particle deposition in a windbreak flow. *J. Appl. Meteorol. Climatol.*, **45**, 1332–1349.

APPENDIX B

2013 FIELD NOTES

B.1 Introduction

This is a report of the procedures, equipment, and collected data from the 2013 field campaign which took place in a vineyard near Monmouth, Oregon in pursuit of the goals associated with the PTRAC development project.

B.2 Meteorological Tower

A meteorological (met.) tower was deployed at a central location within the southwesterly most block of the vineyard (44° 49′ 27.0″ N 123° 14′ 17.0″ W). A single 10 m tower was used and was erected such that it was against the vine to its immediate east with the anemometers mounted off its northwest edge. A Campbell Scientific CR3000 datalogger was used for most of the equipment on the tower. An additional CR5000 datalogger was used for other peripheral sensors as specified below.

B.2.1 Anemometers

Six Campbell Scientific CSAT3 sonic anemometers were deployed at heights of:

- 10.09 m
- 5.05 m
- 3.01 m
- 1.98 m
- 1.37 m
- 0.73 m

where all were measured above ground level (AGL) in the middle of the aisle to the center of the anemometer sampling volumes.

The anemometers were oriented such that the CSAT3 heads pointed at a heading of 270°. The lowest three CSAT3's were all mounted in perfect vertical alignment (sampling volumes directly above each other) with the sampling volumes nearly centered in the aisle. The sampling volumes of all three were 46″ from the centerline of the vine to the west and 47″ from the centerline of the vine to the east. Because of the orientation of the anemometers and their location with respect to the tower frame, periods with mean wind directions between 75° and 138° should be excluded from analysis.

B.2.2 Eddy-covariance EC150

A Campbell Scientific EC150 was deployed with the CSAT3 at 5.05 m AGL. The EC100 temperature probe in its shield was mounted to the tower such that its height was equal to the height of the center of the sampling volume of the CSAT3 and EC150. The EC100 electronics enclosure was mounted to the tower somewhat lower than the head, and although no specific measurement was taken, it was ≈ 3.75 m AGL.

B.2.3 Fine-wire Thermocouples

Each CSAT3 had either a Campbell Scientific FW05 or FW1 fine-wire thermocouple (TC) collocated with it such that the couple was located at the same heights as the sampling volume heights listed for the CSAT3's. All of the fine-wire TC's were wired to the CR3000 datalogger and were logged in order based on height, i.e., the fine-wire at 10.09 m was fw_1, the one at 0.73 m was fw_6.

B.3 Other Energy Budget Sensors

B.3.1 Leaf and Leaf Replica Sets

Two real grape leaves were chosen for temperature collection using Type E TC's. The TC's were attached to the underside surfaces of the leaves using a highly conductive adhesive paste. Next to each real leaf, a similarly sized leaf replica cut out of copper plate was held in the canopy using small clamps attached to a T-post. The replicas were kept at the same heights as the real leaves, were deployed immediately

next to the real leaves, and also had Type E TC's attached to the underside of the copper. The leaf and replica pairs were positioned on the eastern facing side of the vine row located immediately to the west of the meteorological tower, and were around 15 m to the south of the tower.

The first leaf pair was initially mounted at 72″ above ground level and were at an incline of approximately 45 degrees, with the leaf tips pointed downward toward the ground at the center of the aisle to the east of the vine row. This set used the larger of the two copper leaves provided by Brian Bailey for use in this data collection. The TC's on the real and artificial leaves were ≈ 6.5″ apart from each other with the replica TC being exactly north of the TC on the real leaf. The second set of leaves included the smaller of the two replica leaves provided by Brian Bailey (although it was the medium sized leaf of the three that had been produced) and were mounted 52″ AGL. They too were ≈ 6.5″ apart on a north-to-south line with the replica leaf to the south of the real one.

All of the leaf TC's, along with multiple other sensors, were logged on a Campbell Scientific CR5000 that was positioned near the base of the T-post. This location, where these and other sensors were deployed to the south of the met. tower, is referred to as the Secondary Energy Station from here on.

An SHT15 temperature and humidity sensor was deployed along with each replica set and was positioned just below (≈ 4″) each pair. The two sensors were logged using a Local Energy budget Measurement Station (LEMS) that was designated as LEMS-T. The LEMS-T was mounted alongside the CR5000 enclosure near the ground and logged the two SHT15 sensors at 1/7 Hz throughout the campaign.

On 8/15/13 the replica sets were rearranged somewhat on the advise of Brian Bailey who needed them in optimal positions for use in radiation model validation. The upper replica set was moved up to a height of 85.5″ AGL and were made perfectly horizontal. A new vine leaf of approximately the same size as the previous one was used and the thermocouple was removed from the previous leaf and attached to the new one. The lower replica set was kept in the same location using the same leaves but was also rotated to being very nearly level with the ground. This slight adjustment meant the TC's were at a height of 52.5″ AGL.

B.3.2 Soil Heat Flux Plates

An HFP01SC (self-calibrating heat flux plates) with accompanying TCAV (averaging thermocouple) and CS616 (soil moisture probe) were deployed ≈ 2 m south of the met. tower. All of the devices were inserted into the ground such that they were pointed to the west from the wall of the hole that was dug, but were nearly centered in the aisle once in the ground, i.e., the hole was dug to the east of the aisle c/l and the devices were pressed into the western surface of the hole so that they were approximately under the c/l of the aisle.

The HFP01SC plates were ≈ 8 cm deep with 62 cm between them, north to south. The CS616 was placed with the more shallow of the two probes at ≈ 2.5 cm deep. The block at the base of the two probes was centered between the HFP's (on the north-to-south line) and thus the CS616 centerline was 31 cm from the nearest edge of each HFP. Because of the length of the CS616 probes and the fact that the block was near the center of the aisle, the probes were primarily sampling soil to the west of the aisle centerline. The TCAV probes were buried with two probes each at ≈ 2 and 6 cm deep. The two sets of two probes were each buried in a vertical line extending up from the proximal edge of each HFP, thus resulting in the pairs also being 62 cm apart from each other (north-to-south) and 31 cm from the CS616 probe centerline, with which they were essentially parallel (east-to-west).

B.3.3 Radiation Sensors

A Kipp & Zonen CNR1 Net Radiometer was deployed at 10.32 m AGL on the main tower and was oriented to 90°. It recorded incoming shortwave radiation from above (SW_up) and below (SW_dn) as well as incoming longwave radiation from above (LW_up) and from below (LW_dn). As part of its internal operations, the CNR1 requires a temperature reading, so it therefore also measured and output temperature via an internal TC, thus providing an additional height to the temperature profiles. A Quantum SQ-110 photosynthetically active radiation (PAR) sensor and a Licor LI-200 net radiometer were mounted to the CNR1 mounting arm and were therefore also at 10.32 m AGL. The LI-200's calibration constant was incorrect when it was originally mounted and initiated but was corrected to a value of 75.527 on 8/7/13.

The CNR1, LI-200, and SQ-110 were all connected to the CR3000 on the tower.

Additional PAR sensors were mounted in the canopy to determine PAR attenuation. Two were mounted with the lower leaf/replica pair described above. These two were positioned back-to-back with one pointed directly upwards and the other directly downwards. Because they were mounted alongside the lower replica leaf, they too were on the eastern face of the vine running along the west side of the met. tower. They were positioned such that they were flush with the mean "surface" of the vine row. A third PAR sensor was mounted below the up/down PAR sensor pair, at a height of 7.5″ AGL and was pointed directly upwards. This PAR sensor was not centered under the vine row but was positioned just to the inside (west) of the vine row surface if the surface were extended down to the ground from the vine above—see page 006 of the handwritten notes for a schematic. A second LI-200 was mounted alongside (north-to-south) the PAR sensor that was nearest to the ground. It was at an effective height of 6.5″ AGL and was also leveled such that it was pointing directly upwards. These three PAR sensors and the LI-200 with them were connected to the CR5000 datalogger.

B.3.4 LEMS

Two LEMS were deployed near the Secondary Energy Station on T-posts in the aisle (Figure B.1). The two LEMS were designated as LEMS-L and LEMS-M. Each LEMS included an SHT15 temperature/humidity sensor, a Licor LI-200, and two Decagon 5TM soil moisture probes. LEMS-L was mounted on a post located 31″ to the east of the vine row to which the leaf TC pairs were mounted. The SHT15 was at a height of 152″, the LI-200 was centered in the aisle (46.5″ from each neighboring vine centerline) and was 3.75″ AGL on its mounting post, and the 5TM's were buried such that they were centered in the aisle and were at depths of approximately 5 and 50 cm. The T-post for LEMS-M was positioned 18.5″ from the centerline of the vine to its west and was thus approximately midway between LEMS-L and the surface of the vine row. It too was mounted such that the SHT15 was at 152″ AGL. The LI-200 was positioned at 23.25″ from the vine to the west and 4.25″ AGL, and was thus approximately midway between the LI-200 used with LEMS-L and the vine

Figure B.1: A northward looking photo of the LEMS and met. tower. LEMS-M is in the left foreground, LEMS-L is in the center, and the met. tower is seen in the right background. The locations of the LI-200's and the 5TMs for each LEMS are visible from the orange tape wrapped around the lead wires. The understory radiation sensors can also be seen in the lower left corner along with the CR5000 enclosure and LEMS-T. The radiation shield protecting the SHT15 deployed with the upper leaf replica can also be seen near the top of the canopy just above LEMS-M.

centerline. The 5TM's for this LEMS were also buried at approximately 5 and 50 cm but were at 16″ from the centerline of the vine row to the west.

All three of the LEMS were set to Utah time prior to transport to Oregon and were not updated at any time during the campaign. No specific timestamp was collected or known for the LEMS during the campaign and therefore, appropriate precautions should be taken when attempting to correlate the LEMS data to the data from either of the dataloggers.

B.3.5 Surface Soil Temperature

Two Apogee SI-111 Infrared Radiometers (IRR's) were deployed on the LEMS T-posts and were logged using the CR5000 of the Secondary Energy Station. The IRR mounted along with LEMS-L was at 36″ AGL on the T-post and was pointed at a downward angle toward the center of the aisle. The IRR mounted along with LEMS-M was also 36″ high and pointed at the center of the aisle. Because of the difference in the east-west location of the two T-posts, the angle at which each of the SI-111's was pointed was slightly different (Figure B.1).

B.4 Canopy Dimensions and Characteristics

The canopy in the area around the met. tower was trimmed to a height of 85″ on average. The bottom of the fruiting zone was between 26″ and 31″ AGL with the fruiting wire typically at about 31″. The vine rows were oriented from 0° to 180° (north-to-south) and were at an average spacing of 96″ on center. Every other aisle in the block was tilled and left as dirt while the others were allowed to have grasses and weeds to grow in them. The vines were trimmed by a tractor-towed mowing machine at least once during the campaign and were also trimmed by hand by farm staff at least once during the campaign as well. Very tight tolerances were kept on the vine dimensions and there was little variation along rows or from row to row. As such, the vine rows were maintained at a relatively consistent thickness of 18″.

B.5 Microsphere Release Events

Three different types of particle release events were conducted under different wind conditions. For the first set of release events, an array was set up that would work for

either north or southwest winds to capture near-source (< 9 canopy heights downwind) dispersion patterns. The final release events were conducted during northerly winds with the intention of collecting long-distance (up to 84 canopy heights downwind) plume dispersion. A total of 23 release events were conducted and time was kept for each on the lab netbook (Table B.1).

B.5.1 Microspheres

Fluorescent polyethylene microspheres of three different colors were used in the field to study particle plume shapes under different meteorological conditions. The three colors were: yellow/green (UVPMS-BY2-1.00), orange (UVPMS-BO-1.00), and violet (UVPMS-BV-1.00) and were all obtained from Cospheric LLC. Spec sheets for each color show the diameter distributions of the microspheres and are kept with the handwritten field notes.

B.5.2 Release Devices

The microspheres were released into the air using ultrasonic nozzles through which the particles were pumped while suspended in a water and surfactant mixture. A Harvard Apparatus syringe pump was used to pump the fluid at a controlled rate through Sonaer Inc. nozzles. The nozzles were mounted onto T-posts that were placed such that they were near the surface of the vine canopy and the nozzle tips were pointed downward. They were attached to the T-posts using finger clamps and were held out from the vine surfaces by about 3″.

For each near-source release event, the three colors of microspheres were each released from different heights in the canopy. The purple microspheres were always released from a height of 151 cm, the orange microspheres were always released from a height of 116 cm, and the green/yellow microspheres were released from a height of 81 cm. The rate of release of each color of microspheres was the same during each event as the syringes were all placed on the same pump in the same way. For all but two of these release events, the pump was set to push 0.5 ml/min of microsphere solution. The solution had a concentration of 0.05 g/ml, which combined with the pumping rate, resulted in 0.5 g of microspheres being released during a 20-minute duration release event.

Table B.1: Release events conducted. Timestamps are from the office netbook which was on Utah time.

Event	Array	Duration (min)	Date	Start Time	Notes
1	W	20	8/7	16:06:25	0.58 g released
2	W	20	8/7	17:36:07	0.48 g released
3	W	20	8/7	18:42:19	
4	W	20	8/7	19:48:41	
5	W	20	8/14	15:29:22	
6	W	20	8/14	16:36:59	
7	W	20	8/14	17:50:29	
8	W	20	8/14	18:57:32	
9	W	20	8/15	15:30:46	
10	W	20	8/15	16:32:32	
11	W	20	8/15	17:19:27	
12	W	20	8/15	18:02:24	
13	W	20	8/16	16:31:07	
14	W	20	8/16	17:16:56	
15	W	20	8/16	18:03:12	
16	N	20	8/19	11:47:29	
17	N	20	8/19	16:34:32	
18	N	20	8/19	17:28:33	
19	N	20	8/19	18:15:41	
20	N	20	8/19	19:14:25	
21	N	20	8/19	19:59:18	
22	LN	20	8/20	16:35:26	3 syringes × 6 g = 18 g
23	LN	18	8/20	17:52:58	3 syringes × 5.4 g = 16.2 g

For the long-distance release events, three ultrasonic nozzles were collocated such that the tips were all within 3″ of each other and centered at a height of 54″ AGL.

B.5.3 Impaction Traps

The microspheres were collected using rotating arm impaction traps built by the USDA-ARS labs. Five impaction traps were mounted at different heights onto towers made of aluminum 80/20 T-channel. Forty of these towers were used to make three-dimensional arrays that were deployed downwind of the plume source locations. The heights of the individual impaction traps were measured to be:

- 9.0″
- 33.6″
- 53.4″
- 74.0″
- 4.9 m

These heights are an average of many towers measured in the field and thus the heights of the traps at any individual tower may have been slightly different due to inconsistencies in the the ground surface. Each impaction trap's crossarm had a radius from the motor drive shaft to the center of the substrate rod hole of 4.3 cm.

B.5.3.1 Near-Source Tower Array

The near-source releases were conducted during either northerly winds or westerly/southwesterly winds. For this, a single continuous array of all 40 towers was arranged to the south and east of the release locations. The array was somewhat similar to the array used in 2011 but with additional towers and a re-arrangement designed based on lessons learned from that campaign (Figure B.2). Labelled schematic layouts of the trap arrays are in the handwritten notes taken during the field campaign along with the measurements used to determine the approximate locations of each of the towers with respect to the source locations. Twenty two of the 40 towers were used for the northerly releases and 23 were used for the westerly releases.

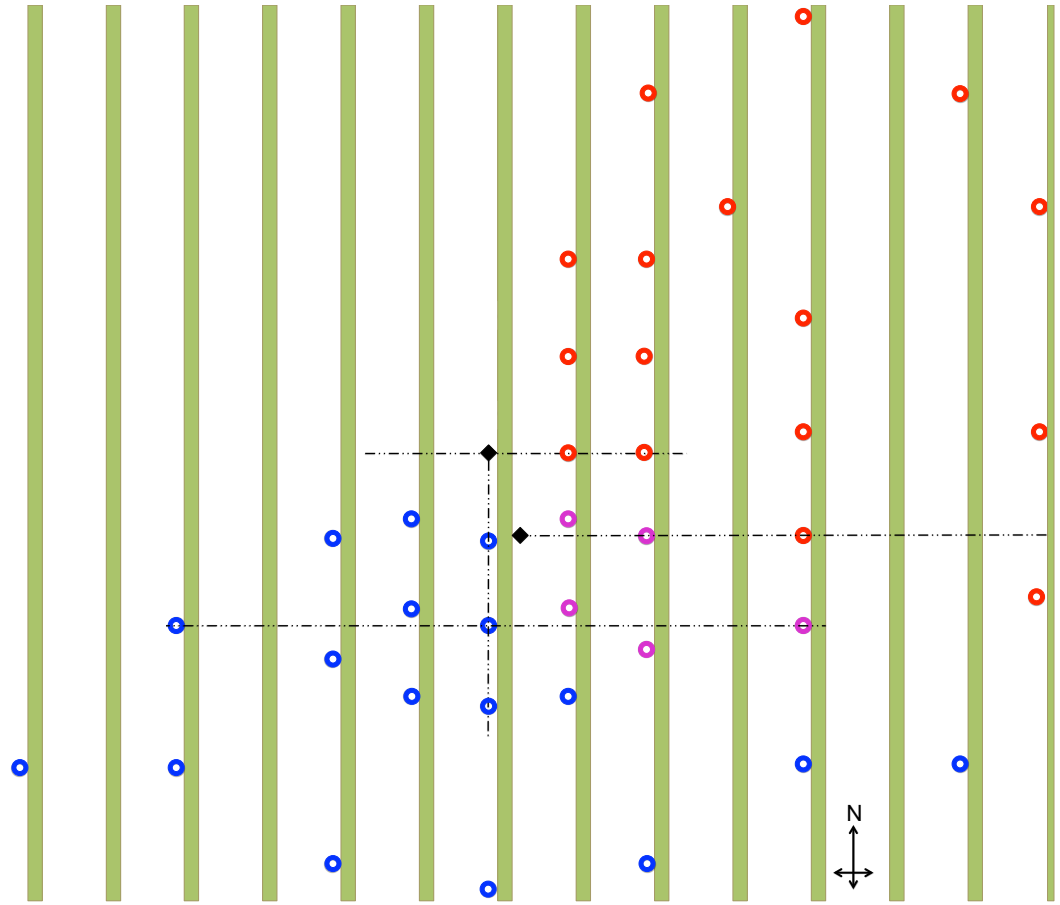

Figure B.2: Schematic of the impaction trap layout with respect to the release device locations within the vineyard. The tower locations are represented by the open circles, the release device locations are represented by the black diamonds, and the vine rows are represented by the green patches. The red and blue circles depict impaction trap tower locations used for the westerly release events and the northerly release events, respectively. The magenta circles depict tower locations used with both the westerly and northerly release arrays.

Towers with tower-numbers 8, 15, 16, and 21–24 were used for both the northerly and westerly release events. Significantly more measurements of the tower locations were taken in the field than there were towers. This resulted in an overdefinition of the layout locations of the towers. These measurements were then used as input data for an optimization program which was used to determine the approximate locations of each tower in two-dimensional space while reducing the error across the entire measurement-equation set (Table B.2). The tower that had been labelled as tower number 6 was located incorrectly initially but was moved to the correct location prior to the first event and was renamed as tower 41.

B.5.3.2 Tower Array for Long-Distance Releases

The impaction trap tower array was rearranged at the completion of the near-source releases into an array for the long-distance release events. The release location used for the near-source northerly wind events was kept as the release location for these events. The arc of towers that was approximately 18 m to the south of the release device location was left in place and became the arc of towers that was nearest to the source for these events. This included tower numbers 4, 7, 14, 29, 36, 39, and 41. A second arc of nine towers was then positioned approximately 90 m south of the source and a final arc of nine towers was positioned approximately 180 m south of the release device (Table B.3). This resulted in a total of 25 towers in the array. Towers 8, 15–16, 22–24, 30–35, 37–38, and 40 were not used in this array.

B.6 Data Files Info

B.6.1 Met. Tower

The anemometers, EC150, and the finewire thermocouples were all logged on the CR3000 at 20 Hz and written to a table that was converted to comma separated files after the campaign. The comma separated files were then converted to MatLab .mat files that were more easily readable. The CR3000 was running on local Oregon time throughout the campaign and therefore no adjustments to the data timestamps were necessary. The .mat files had columns in the following order:

Table B.2: Approximate locations of the impaction trap towers within the array. Coordinates are in meters and with respect to the two release locations as specified.

Tower	Westerly source		Northerly source	
	distance east	distance north	distance east	distance north
1	16.13	-2.66	—	—
2	16.18	2.72	—	—
3	16.15	8.84	—	—
4	—	—	14.40	-15.06
5	13.68	11.85	—	—
7	—	—	9.54	-14.95
8	8.73	-3.35	9.42	-5.82
9	8.77	-0.24	—	—
10	8.77	2.76	—	—
11	8.71	5.89	—	—
12	8.76	17.03	—	—
13	6.39	8.99	—	—
14	—	—	4.63	-17.12
15	3.91	-4.51	4.60	-6.98
16	3.96	-0.09	4.65	-2.56
17	3.93	2.35	—	—
18	3.93	4.34	—	—
19	3.93	6.34	—	—
20	3.94	8.48	—	—
21	3.96	14.54	—	—
22	—	—	2.29	-7.21
23	1.57	-2.59	2.26	-5.06
24	1.54	0.10	2.24	-2.37
25	1.58	2.45	—	—
26	1.59	4.47	—	—
27	1.58	6.46	—	—
28	1.58	8.55	—	—
29	—	—	-0.13	-17.77
30	—	—	-0.14	-8.38
31	—	—	-0.19	-5.57
32	—	—	-0.19	-2.63
33	—	—	-2.63	-7.93
34	—	—	-2.66	-5.07
35	—	—	-2.68	-2.14
36	—	—	-5.07	-16.98
37	—	—	-5.13	-6.74
38	—	—	-5.17	-2.50
39	—	—	-9.97	-14.69
40	—	—	-9.87	-5.77
41	—	—	-14.83	-14.53

Table B.3: Approximate locations of the impaction trap towers within the array for the long-distance release events.

Tower	distance east [m]	distance south [m]
1	50.8	172.7
2	38.8	81.2
3	36.2	176.3
4	14.4	15.1
5	29.1	85.2
7	9.5	-15.0
9	24.0	178.4
10	19.3	87.9
11	11.8	179.6
12	9.6	89.5
13	0.0	90.0
14	4.6	17.1
17	0.0	180
18	-10.0	89.4
19	-12.4	179.6
20	-19.7	87.8
21	-24.5	178.3
25	-29.5	85.1
26	-36.7	176.2
27	-39.2	81.0
28	-51.3	172.5
29	-0.13	17.8
36	-5.1	17.0
39	-10.0	14.7
41	-14.8	14.5

- Timestamp: 6 columns covering month, day, year, hour, minute, second in Oregon time
- EC150: CO_2, H_2O, T, P_a
- 10.09 m anemometer: u, v, w
- 5.05 m anemometer: u, v, w
- 3.01 m anemometer: u, v, w
- 1.98 m anemometer: u, v, w
- 1.37 m anemometer: u, v, w
- 0.73 m anemometer: u, v, w
- Fine wire thermocouples: fw_1 through fw_6
- Anemometer sonic temperatures: 10.09 m through 0.75 m heights

The timestamp on this CR3000 was 1 minute and 30 seconds different from the netbook stamp, in addition to the one hour timezone difference, i.e., CR3000: 12:46:30 = Netbook: 13:48:00. These .mat files were named with a leading "T" for tower followed by a date stamp of the month and day, e.g., *T0816.mat*. For each of the release event periods, tower data were extracted from the whole dataset and saved as their own .mat files. The appropriate timestamp corrections were made to the release event timestamps taken on the netbook so that the correct data were extracted from the CR3000 data which were run on Oregon time. These files were simply named as "Release" and the event number, e.g., *Release16.mat*.

The data from the CNR1, the LI-200, and the PAR sensor on the met. tower were all logged at 1 Hz on a CR3000 using a "SlowSequence" command in the main program. The data were written to a table that was later converted to comma separated and then to .mat files with the data in columns in the following order:

- Timestamp: 6 columns covering month, day, year, hour, minute, second in Oregon time

- CNR1: SW_up, SW_dn, LW_up, LW_dn, T
- LI200: net radiation from above
- PAR: net PAR from above
- 2 HMP45 values which never worked correctly and should be ignored entirely

These files were named in the same manner as the files for the bulk tower data but a leading "E" was used, e.g., *E0817.mat*.

B.6.2 Secondary Energy Station

Data from the leaf and leaf replica TC's, the below-canopy LI-200, the canopy PAR sensors, and the IRR's were recorded at 1 Hz on the CR5000. The CR5000 was set to the French timezone throughout the campaign. The data were written into a table which was converted to .mat files after the experiment. The appropriate correction to the timestamps was made during this conversion such that the .mat files were in Oregon time. An appropriate check of the timestamp conversions, done by comparing the original .dat files and final .mat files, should be done prior to using the data. The resulting .mat files had the following column designations:

- Timestamp: 6 columns covering month, day, year, hour, minute, second in Oregon time
- TC's from the leaf and replica pairs: Upper copper leaf, upper real leaf, mid-canopy copper leaf, mid-canopy real leaf
- PAR's: Mid-canopy upward pointed sensor, mid-canopy downward pointed sensor, below canopy sensor
- LI-200: net radiation below canopy
- SI-111's: Sensor body temperatures ×2, thermopile mV readings ×2, radiometer target temperatures ×2

These files were named in the same manner as the previous versions but with a leading "L" for leaf, e.g., *L0821.mat*.

The data for the HFP01SC were also recorded on the CR5000 and written to its own table. The data were converted to comma separated files but were never converted to .mat files. This was not done because there was no immediate need for the data as well as there being some uncertainty about the data due to doubts about the accuracy. It was realized after the campaign that the code for the plates may not have been working as expected, and also that due to the timestamp difference on the CR5000, the self-calibration of the heat flux plates was happening at 17:00 Oregon time instead of at 24:00 as expected. It is possible that the data from the CS616 and the TCAV's are accurate and usable, but the data from the flux plates themselves should be quality checked extensively before use. The columns of the comma separated table include:

- Timestamp
- HFP: Heat flux of the plates ×2
- CS616: Volumetric soil water content
- TCAV: Average soil temperature above the plates averaged over all four temperature probes
- HFP: calibration constant for each plate

The French timezone timestamp for the CR5000 was an additional 18 seconds different from the netbook time, i.e., CR5000: 11:20:18 = Netbook: 05:20:00.

B.6.3 LEMS

The data files from the LEMS are all labeled in self-explanatory ways and the columns have appropriate headings in every individual comma separated file. No datatype conversions of quality checking of the data has been performed, but the data are believed to be of sufficient quality.

B.7 Other Notes

Before attempting anything with any of these data, the scanned notes taken in the field should be read thoroughly. There are many details in them that were not

transferred to this document. This includes timestamps for when equipment was installed and turned on and off for battery switches and such. It also includes details on when some equipment quit working and was fixed.